Characterisation and Design of Novel Non-Foster Circuits for Electrically Small Antennas

Deepak Singh Nagarkoti

A thesis submitted in partial satisfaction

of the requirements for the degree of

Doctor of Philosophy

School of Electronic Engineering and Computer Science

Queen Mary University of London

February, 2017

Dedicated to my Family

Abstract

There is a demand for broadband electrically small antennas that cover large frequency bands without any requirement of reconfiguration techniques. This is particularly true at low frequencies (VHF/UHF), where wavelengths are long and antennas are physically large. The fundamental gain-bandwidth limitation was related to the electrical size of passive electrically small antennas by Wheeler and Chu; their result implied that an electrically small antenna exhibits high quality factor which limits the bandwidth. Additionally, the gain-bandwidth limitation was related to impedance matching conditions by the Bode-Fano criteria, which restricts available bandwidth using conventional reactive elements. A non-Foster circuit approach has been presented which delivers a broadband input impedance match and also overcomes the aforementioned fundamental limits. These non-Foster impedance circuits can be realised by negative impedance converters (negative inductance and/or capacitance). The thesis also explores the advantages and challenges of antenna impedance matching using negative impedance circuits based on two topologies: (1) conventional transistor-based circuits, and (2) a novel resonant tunnelling diode approach. The advantages of non-Foster circuits in the implementation of broadband small antennas include wideband performance around one-tenth of the self-resonant frequency and overcoming of the fundamental limits associated with passive

antennas. Diode-based circuits are more compact, easily configurable, less sensitive to stability, have low power consumption and are less complex as compared to the transistor based designs. These features makes it a potential candidate for array and meta-material applications. However, there are few challenges for non-Foster circuit integration with an antenna due to high noise figure, which affects the system channel capacity and receiver performance in a communication system. A detailed design procedure has been developed to mitigate the effects of noise and instability and also, the system performance and measurement of the non-Foster circuit integrated antennas have been discussed.

Acknowledgements

Firstly, I would like to thank my advisor, Dr. Khalid Z. Rajab, for his excellent guidance and overwhelming support throughout my doctoral study. I would not have achieved as much progress as I have without his persistent encouragement and professional advice.

I would like to express my deepest gratitude towards my co-advisor, Prof. Yang Hao for providing guidance and motivation throughout my research. As a pioneer in the field, he enlightened me about the nature of research and has guided me on my journey through challenging works.

Besides my advisers, I would like to thank Dr. Akram Alomany for providing insightful comments, continuous encouragement and serving in my examination committee. I would also like to thank my colleagues Dr. Yifeng Fan and Jing Tian for the fruitful discussions and collaborative research work. I would like to mention a special word of appreciation to my colleague Peter Alizadeh and the electronics lab manager Kok Ho Huen for their professional support during the PhD.

I would like to give the most of the credit to my parents Bikram Singh Nagarkoti and Vidya Nagarkoti, for their support, guidance, and sacrifices. I don't want to miss this opportunity to thank my uncle Gulab Singh Tharkoti and aunt Kamlesh Tharkoti. This dissertation would not have been possible without their belief, support, love, care and constant encouragement to

follow my dreams. Thanks to my brother Gajender Singh Nagarkoti and uncle Shyam Singh Tharkoti for their selfless cooperation at every stage in my life. I would also like to thank my cousin Siddharth Bhandari for his tremendous support during some of the difficult times in my life.

I would also like to thank my friend Devashis Negi for his support when I was in need of help the most.

Also, I would like to thank my fellow lab mates for the stimulating discussions, all the fun that we have had in the past four years and the sleepless nights we worked together before deadlines. I would like to present my heartiest gratitude to Dr. Melusine Pigeon, Shakar Alkaraki, Dr. Guangwie Jiang, Dr. Manmohan Sharma, Fizzah Jilani, Nishtha Chopra, Majid Naeem, Darryl Smith, Andy Sarker, Dr. Oleksandr Sushko, Dr. Zhijiao Chen, Dr. Oscar Quevedo-Teruel, Hassan Farooq and Muhammad Qureshi for always being so sweet and helpful towards me. In general, I would like to thank everyone in the **Antenna and electromagnetics research group** at QMUL for their direct and indirect contributions in my journey throughout the graduate program.

Last but not the least, big thanks to my soul mate, my wife Megha who has always supported and pushed me to give my best. This thesis would have never been completed without her sacrifices, encouragement and love.

Licence

Contents

List of Figures

List of Tables

List of abbreviations

ESA	Electrically Small Antenna
NFC	Non-Foster Circuit
NIC	Negative Impedance Converter/Circuit
BJT	Bipolar Junction Transistor
ENR	Excess Noise Ratio
OCS	Open-Circuit Stable
FR-4	Flame Retardant-4
SCS	Short-Circuit Stable
SNR	Signal-to-Noise Ratio
Q	Quality Factor
Op-amp	Operational Amplifier
VHF	Very High Frequency
UHF	Ultra High Frequency
GFET	Graphene Field Effect Transistor
RTD	Resonant Tunnelling Diode
SEM	Scanning Electron Microscope
NDR	Negative Differential Resistance
NFA	Non-Foster Antenna
PCB	Printed Circuit Board
SNRIF	Signal-to-Noise-Ratio Improvement Factor
MTM	Meta-material

0.1 Associated Publications

Journal Articles

(1) **Deepak S. Nagarkoti**, Y. Hao, D. P. Steenson, L. Li, E. H. Linfield, K. Z. Rajab, "Design of Broadband Non-Foster Circuits based on Resonant Tunneling Diodes", *IEEE Antenna and Wireless Propagation Letters*, vol. 15, pp. 1398-1401, April 2016.

(2) **Deepak S. Nagarkoti***, J. Tian*, K. Z. Rajab , Y. Hao (***equal contribution**), "Graphene-Based Tunable Non-Foster Circuit for VHF Applications", *AIP advances*, June, 2016.

(3) Y. Fan, **Deepak S. Nagarkoti**, K. Z. Rajab, Y. Hao, H. Zhang and T. J. Cui, "Wave Propagation in Reconfigurable Broadband Gain Metamaterials at Microwave Frequencies", *Journal of Applied Physics*, vol. 119, 194904, May 2016.

(4) Y. Fan, H. C. Zhang, L. Xu, **Deepak S. Nagarkoti**, Y. Hao and T. J. Cui, " An Active Wideband and Wide-Angle Electromagnetic Absorber at Microwave Frequencies", *IEEE Antenna and Wireless Propagation Letters*, vol. 15, March 2016.

(5) Y. Fan, **Deepak S. Nagarkoti**, K. Z. Rajab, H. C. Zhang, L. Xu, Y. Hao, T. J. Cui, "Immittance-Based Stability Characterization on Active Metamaterials with Non-Foster Loads ", *IEEE Transaction Antenna and Wave Propagation* (Under review)

(6) **Deepak S. Nagarkoti**, K. Z. Rajab, Y. Hao, "System Performance Limitation of a non-Foster Antenna", *IEEE Transaction Antenna and Wave Propagation* (submitted).

(7) **Deepak S. Nagarkoti**, K. Z. Rajab, Y. Hao, "Comparative Study of Transistor and Diode based Non-Foster Matching for Electrically Small Antenna", *IEEE Transaction Antenna and Wave Propagation* (under preparation).

(8) **Deepak S. Nagarkoti**, K. Z. Rajab, Y. Hao, "Noise in transistor based non-Foster circuits in VHF band", *Electronics letters* (under preparation).

Conference Papers

(9) **Deepak S. Nagarkoti**, Y. Hao, K. Z. Rajab , " Non-Foster Matched Reconfigurable Antenna in UHF band", *4th Advanced Electromagnetics Symposium*, Torremolinos, Malaga, Spain, July, 2016.

(10) J. Tian, **Deepak S. Nagarkoti**, K. Z. Rajab, Y. Hao. " Negative Impedance Converter Based on Graphene Field-Effect Transistor", *Graphene Week, Graphene Flagship*, Warsaw, Poland, July, 2016.

(11) **Deepak S. Nagarkoti**, Y. Hao, K. Z. Rajab, "Radiation-Q bound of a Small Non-Foster Antenna", *Proc. IEEE Int. Symp. Antennas Propag. Soc. (APSURSI)*, Puerto Rico, June, 2016.

(12) **Deepak S. Nagarkoti**, Y. Hao, K. Z. Rajab, "Signal to Noise Ratio Improvement with Non-Foster Antenna Matching", *Proc. IEEE Int. Symp. Antennas Propag. Soc. (APSURSI)*, Puerto Rico, June, 2016. **(Invited)**

(13) **Deepak S. Nagarkoti**, Y. Hao, and K. Z. Rajab. "Q-Bandwidth Enhancement of an Antenna using Non-Foster circuit based on Negative

Differential Resistance Devices", *The 10th European Conference on Antennas and Propagation (EuCAP)*, Davos, Switzerland, April, 2016.

(14) **Deepak S. Nagarkoti**, P. Alizadeh, Y. Hao, K. Z. Rajab, et al. "Stability Analysis of Resonant Tunnelling Diode for Resistive Matching of an Electrically Small Antenna", *Proc. IEEE Int. Symp. Antennas Propag. Soc. (APSURSI)*, Vancouver, Canada, 2015.

(15) **Deepak S. Nagarkoti**, Y. Hao, and K. Z. Rajab. "Noise Measurements of a Non-Foster Circuit for Matching of a Receiver Antenna", *The 9th European Conference on Antennas and Propagation (EuCAP)*, Lisbon, Portugal, April, 2015.

(16) **Deepak S. Nagarkoti**, K. Z. Rajab, and Y. Hao. "Design and Stability of Negative Impedance Circuits for Non-Foster Matching of a Monopole Antenna", *The 8th European Conference on Antennas and Propagation (EuCAP)*, Hague, Netherlands, April, 2014.

(17) K. Z Rajab, **Deepak S. Nagarkoti**, Y. Fan, Y. Hao, "Actively-matched Antennas for UHF Applications", *Progress In Electromagnetics Research Symposium*, Stockholm, Sweden, 2013.

(18) K. Z. Rajab, Y. Fan, **Deepak S. Nagarkoti**, Y. Hao, "Stability and Noise in Active Metamaterials", *Progress In Electromagnetics Research Symposium*, Stockholm, Sweden, 2013.

Chapter 1

Introduction to the Theory of Small Antennas

1.1 Quality factor of electrically small antennas

The concept of quality factor (Q) was introduced by Wheeler [6] in the discussion of the limitations associated with small antennas. An equivalent circuit model for small antenna has been proposed and the Q has been defined as the ratio of reactive power to the radiated power. The first relationship between the antenna size, bandwidth and Q has been investigated and it is concluded that Q is inversely proportional to the antenna size as well as the bandwidth. This inference is also applicable for electrically small antennas (ESAs) and confirms the fact that an ESA is fundamentally narrowband. Later, Chu [7] evaluated the minimum Q and hence, the maximum bandwidth of an ideal omnidirectional antenna, enclosed in an imaginary sphere which has been termed as Chu's sphere. Chu used spherical wave functions to represent the radiated fields as a sum of spherical modes. An equivalent lumped circuit is presented here to represent each mode and its

corresponding Q has been estimated. Initially, the concept of Q seems insignificant, however, practically, the gain-bandwidth parameters are highly important in an antenna. Also, the direct measurement of bandwidth is challenging in nature as Q is more suitable quantity being inversely related to the bandwidth in most of the cases. Hence, bandwidth improvement is possible by modification of the antenna structure and its internal fields which consequently affects its Q.

Harrington [8] also followed the circuit approach and obtained a lower minimum Q than Chu's estimation by considering the antenna as radiating in both TE and TM modes. A few years later, Collin and Rothschild [9] developed a field-based approach instead of the aforementioned circuit based method to calculate the exact Q for an antenna radiating either in TE or TM modes. This field-based method was then generalised by Fante [10] for both TE and TM modes and obtained the exact Q for both modes.

Mclean [11] later repeated Chu's work by using a prolate spheroidal wave function. Later, In 2003, Thiele [12] estimated that the value of Q is strongly dependent on the current distribution and determined Q from the concept of super directive ratio. Geyi [13] challenged the work carried out by [9] and claimed the fact that their analysis was not feasible for many antennas. They further re-investigated and produced another approximate method for the calculation of Q that comprised of less complicated integral computations.

Yaghjian and Best [14] exploited the approximate expressions for Q in terms of field, impedance and bandwidth. Also, they examined the effect of wire folding on the radiation resistance and Q. Kwon [15] figured out the inconsistencies in the previous work and did extensive work in re-defining the antenna gain, Q, TE/TM modes and directionality. Thal [16] extended

Chu's work by considering that the surface current distribution of the antenna over a sphere radiates both in the TE and TM modes. He also introduced an additional equivalent circuit to store the energy inside Chu's sphere and to derive gain and Q relationship. Gustafsson [17] proposed an expression for Q in arbitrary shaped small antennas using scattering theory and represented the antenna concerning the material dyadics.

Despite the study of Q, size and bandwidth relationship, it is clear that there are few fundamental limitations which have to be addressed and researched well to improve the small antenna performance. The following section will define the extent to which the operation of small antennas is limited.

1.2 Fundamental limitations of small antennas

The relationship between Q and ka is inversely proportional in all the formulations. One of the most accepted relationship is given as [11]

$$Q_{min} = \eta \left(\frac{1}{ka} + \frac{1}{n(ka)^3} \right) \tag{1.1}$$

Here, η is the antenna efficiency and factor n is the number of modes contained within the antenna. Also, $k = \frac{2\pi}{\lambda}$ is the wave number and a is the radius of the sphere enclosing the antenna.

The small antennas have a size defined by the radius of Chu's sphere, which is a fraction of the wavelength and also, (1.1) clarifies that this leads to high Q for these small antennas. An antenna is fundamentally a bandpass filter having one port connected with conductive field and the other with a radiative field. The bandwidth parameter is significant for any antenna and limited bandwidth can be improved at the expense of antenna efficiency

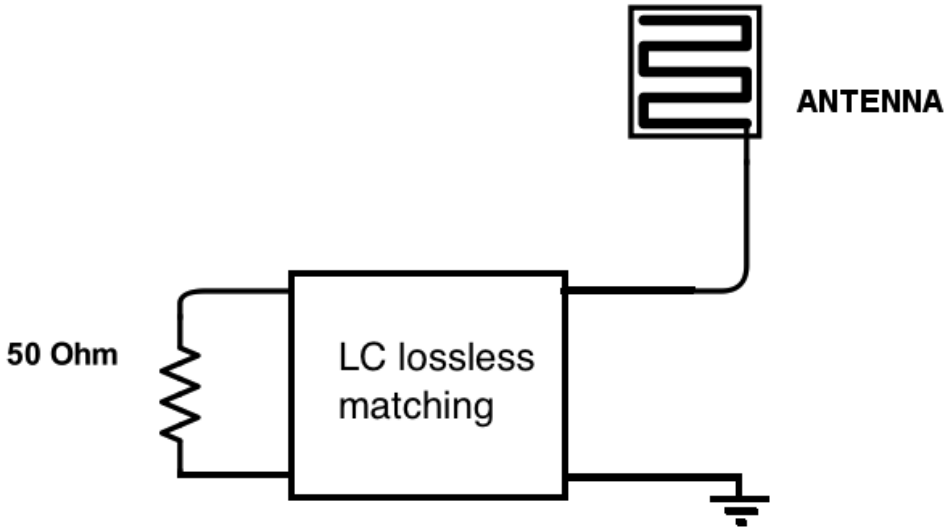

Figure 1.1: Antenna matching improvement using a lossless reactive matching network.

[18]. A lossy antenna has high reflection coefficient and poor efficiency, which implies a trade-off in the efficiency-bandwidth product relationship. The relationship of fractional bandwidth B of a standalone antenna with Q and voltage standing wave ratio (VSWR) is given as [14]

$$B_{max} = \frac{1}{Q_{min}} \frac{(VSWR - 1)}{\sqrt{(VSWR)}} \tag{1.2}$$

1.2 clarifies that the maximum achievable fractional bandwidth for some VSWRs is dependent on the lower bound of Q, which in turn is dependent upon the antenna size and efficiency as shown in 1.1. Therefore, the high Q of small antennas restrict the bandwidth for self-resonating antennas. As shown in Fig. 1.1, bandwidth can be improved by using a lossless matching circuit that could minimise the VSWR to a certain extent. However, the maximum achievable bandwidth using a lossless passive matching network is limited by the fundamental limit of matching, which is given by Bode and

Fano [18, 19] as

$$B = \frac{1}{Q}\frac{\pi}{ln(\frac{1}{\Gamma_{max}})} \tag{1.3}$$

Γ_{max} in 1.3 is the maximum reflection coefficient allowed with passive lossless matching network. Also, high value of Q in small antennas limits the maximum impedance bandwidth B.

1.3 Motivation

The aforementioned performance limitations have significantly induced encouragement to research the methods and practices available, which can outweigh these limitations. Overcoming Foster's reactance theorem [20] provides a mechanism through which the limitations of ESAs can be surmounted. The reactance theorem had been presented almost a century ago, which states that, a lossless reactance variation with frequency must have a positive slope. In other words, the frequency derivative of a lossless passive circuit reactance is always positive. This theorem is applicable for any lossless passive matching network.

In general, ESAs exhibits high Q impedances due to their large reactances and small radiation resistances. As discussed in previous section, the matching of any small antenna using lossless passive element is limited by its bandwidth. The effectiveness of passive lossless matching network for a load is limited by gain bandwidth theory. A negative impedance circuit (NIC) or non-Foster circuit (NFC) demonstrates non-Foster behaviour which has a negative slope of impedance. The NFC circuits are negative inductors or negative capacitors which nullify the reactance of antennas over a wide range of frequencies. This non-Foster based active impedance matching approach is sufficient to overcome the aforementioned gain-bandwidth

product limitation and emerges to be a promising design solution for ESAs with low profile, wide bandwidth and high gain. There are certain advantages and challenges which are inspiring to carry forward as research in this domain and a well planned investigation is required to identify the true potential of non-Foster approach in small antenna enhancement.

1.4 Non-Foster circuits

Non-Foster circuits contradicts the Foster's reactance theorem and possess negative frequency derivative of reactance or susceptance. These circuits are artificially designed using active elements to obtain equivalent negative inductance or capacitance. Conventionally, the loading effect of an inductor L is cancelled by a capacitive element C and the narrow band resonance is obtained at frequency, $\frac{1}{2\pi\sqrt{LC}}$. Non-Foster element, $-L$ cancels the inductive load at all frequencies and shows a unique characteristic that opens gateway for many interesting applications in the microwave regime. While moving from load towards the generator in Smith's chart, passive elements rotate clockwise with frequency, but NFCs/NICs rotate counter-clockwise, thus, leading towards a negative delay. As shown in Figure 1.2, the non-Foster matching results in a theoretically infinite bandwidth irrespective of the band-limited conventional matching.

1.4.1 Advantages

In theory, NFCs overcame Chu's limit of small antennas and Bode-Fano's limitation of matching an arbitrary impedance. In true words, Chu's fundamental limit is defined for passive structures whereas the Bode-Fano limit is applicable only for a lossless matching network. Due to the active circuitry

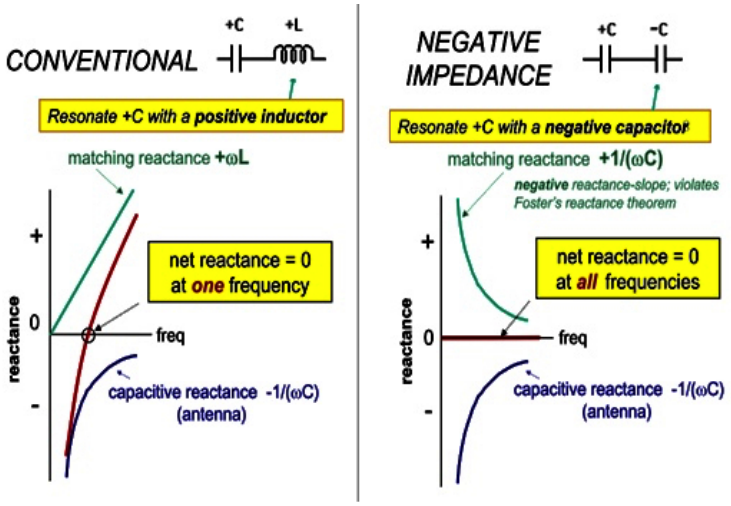

Figure 1.2: Comparison of conventional matching and non-Foster matching, showing the bandwidth enhancement.

involved in NFC design, the studies here, does not violate the standard definition of any of the fundamental limits of small antennas. Furthermore, these NFCs are useful for size reduction of an antenna with a active matching network to obtain high bandwidths. An antenna self-resonating in GHz range could be matched to VHF range using a compact non-Foster circuitry [5]. The improvement in radiation bandwidth can be achieved with non-Foster inclusion, but much less than the impedance bandwidth due to the presence of additional losses. Additionally, SNR (signal-to-noise-ratio) improvement has also been achieved which is limited to the noise figure of NFC. Further, an active wideband absorber has be realised using the non-Foster inclusion in the conventional approach [21]. It is also observed that a non-dispersive superluminal propagation is achievable in a transmission line loaded with non-Foster elements [22].

1.4.2 Challenges

Non-Foster study introduces many additional challenges that are needed to be addressed. In the conventional approach, active elements involved in the NFCs are cross-coupled transistor pairs that provide positive feedbacks to develop non-Foster impedances. Stability in this feedback loop is difficult to achieve due to its oscillation sensitivity. Another critical issue encountered here is, that these transistors are sources of shot noise which degrades the overall performance of the antenna in receiver mode. The noise is introduced and the noise figure measurements have been discussed in chapter 5. Additionally, fundamental limit for SNR improvement has been proposed. The scope of simultaneous power and information transfer using an NFC integrated antenna have been investigated and the system performance limitations have also been discussed. Apart from the noise related challenges, the non-linear behaviour of the NFC with an increased input power restricts its application for high power transmission.

1.5 Thesis organisation

The thesis presents conventional and a novel NFC design for improvement in the performance of small antennas. Due to a few limitations of non-Foster elements, antenna performance is limited only to certain advantages.

Chapter 1 introduces the fundamental bandwidth limitations of small antenna and also presents an NFC-based solution for performance enhancement.

Chapter 2 presents the background theory regarding conventional designs

of NFCs/NICs and also discusses about the modern techniques to achieve non-Foster impedance. Literature review and background study of non-Foster matched small antennas have also been covered along with the solution for stability issues.

Chapter 3 explains the design and development of various stable NFCs. The primary goal here is, to prototype and measure bipolar junction transistor (BJT) based NFC. Further, the chapter explores about NFCs using a graphene field-effect transistor (GFET) and presents the design and stability simulation. Finally, a novel alternative approach for NFC design has been proposed using a resonant tunnelling diode (RTD) along with its capabilities to achieve stability and miniaturisation.

Chapter 4 describes the integration of developed NFC with a suitable passive antenna. It also shows the estimation of Chu's limit for an NFC integrated antenna. Additionally, it presents the prototype of a BJT-based NFC antenna and its impedance and radiation characterisation. Furthermore, the chapter also discusses about the matching of an ESA model using RTD-based NFC network.

Chapter 5 presents the noise analysis along with its effect on SNR and system performances. The noise figure measurement of a BJT-based NFC has been performed under consideration of uncertainty. A fundamental limit for SNR improvement has been derived and the noise performance of BJT-based NFC antenna has been evaluated along with the investigation of channel capacity and power delivery in communication systems.

Chapter 6 summarises the advantages of NFC integrated antennas and associated research challenges in the field of antenna and microwave applications.

1.6 Novel Contribution

The key contributions of the presented work is summarised below

1. A BJT-based NFC has been designed, simulated, fabricated and tested to obtain negative capacitance up to 1 GHz frequency range.

2. A novel approach to obtain various combinations of NFCs has been introduced using the RTDs and a general solution has been presented by broadband matching of small antenna model. Also, graphene-based FET approach is exhibited to achieve the non-Foster impedance and its stability conditions.

3. The improvement in radiation bandwidth has been measured with the inclusion of a BJT-based NFC in conventional ESAs.

4. Noise figure measurements of a BJT-based NFC has been performed and the uncertainty calculations have been estimated.

5. Fundamental limit of Q and the corresponding theoretical limit for SNR improvement for an NFC integrated antenna has been derived.

6. The improvement in SNR bandwidth has been evaluated for NFC integrated antennas in comparison to its passive counterpart.

7. System performance in terms of simultaneous power and information transfer has been investigated in an NFC integrated antenna.

Chapter 2

Background of Non-Foster Impedance Circuits in Antennas

In contrast to passive circuit elements, non-Foster components have negative reactance slope with frequency variation. This unique feature provides interesting and promising outcomes for microwave applications, such as broadband matching of small antennas, RF absorbers, high impedance surfaces, meta-materials (MTMs) and more. This chapter reviews the basic theoretical research methodology of the NFCs and their circuit realisation using conventional techniques. The NFCs are intrinsically unstable due to the negative impedance, which can potentially lead to producing unwanted oscillations. Due to this particular drawback NFCs often cannot operate as a standalone device. A literature review on NFC stability and its contribution in the performance enhancement of small antennas has also been discussed.

2.1 Introduction to non-Foster circuits

Non-Foster impedance is artificially designed and all the conventional reactances follow Foster's reactance theorem, which emphasises that, for any single or two-port passive and lossless network, the reactance always increases monotonically with the frequency. In other words, this artificially designed element exhibits negative impedance and the corresponding circuits are then, known as NICs or NFCs. The design of non-Foster impedance circuits using vacuum tubes [23] and bipolar transistors [1] was proposed in the early 50s. The NFCs were primarily invented to provide negative resistance (gain) for repeaters in telephone plants to overcome transmission line losses. The concept of non-Foster impedance was proposed in the 1920s by Merrill and later in 1951, the vacuum tube based NFC was presented [23]. These NFCs were bulky and fragile in terms of performance, sensitivity and had a limited life-cycle. Two years later, Linvill proposed balanced and unbalanced bipolar transistor-based voltage-inversion NICs (VNICs) which offered improved performance as compared to the existing ones, owing to their light weight, rigid prototype and durability. However, practical behaviour of these NICs was not even close with the ideal design and hence, the necessity for a compensation network was required, which was later proposed by Larkey [24]. In the same year, Yanagisawa [25] introduced a transistor-based current inversion NIC (INIC) and also performed the experiments on the same to verify the parameters. Later in 1959, Indiresan described that application of negative resistance is suitable for implemention in dc analogue computers[26].

Overall, the aforementioned transistor design methodologies and the active component operation is dependent upon the biasing mechanism which

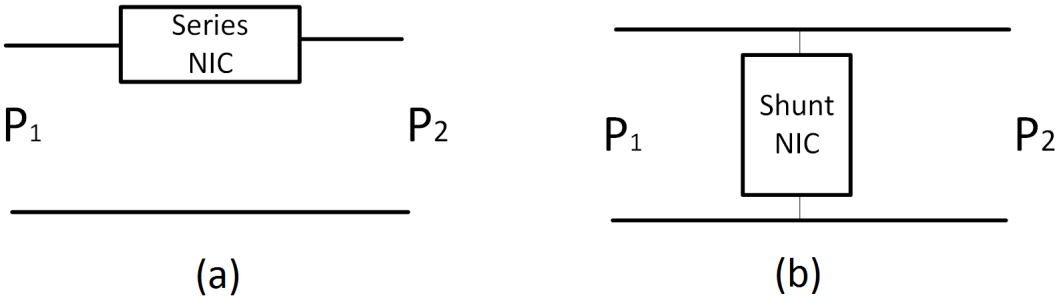

Figure 2.1: The circuit showing utilisation of non-Foster elements within two networks (a) Two-port floating series element (b) One-port grounded shunt element.

is provided by a dedicated external dc power supply. An internal biasing technique was proposed by Nagata, [27] which offered reasonable linearity from dc to the cut-off transistor range.

2.2 Design concept and procedures

Until late 60s, NFCs were well-known in engineering applications, but its practical realisation was still confined due to the stability issues. As on date, the hardware implementation of a stable NFC is quite challenging at high frequencies. Hence, the basic conceptual design of non-Foster impedance generators has been studied here in detail which is then followed by various possible practical design methodologies of implementation. A negative or non-Foster impedance is achieved across both the terminals of a two-port network with an active circuit configuration and a passive load impedance. This two-port NFC can be used in a series or shunt configuration as shown in Fig. 2.1(a) and Fig. 2.1(b) respectively. The NFC design configuration includes active components like transistors, connected in a cross-coupled manner as shown in Fig. 2.2 with the necessary biasing mechanism. It comprises of four stability poles such that the input and output currents are

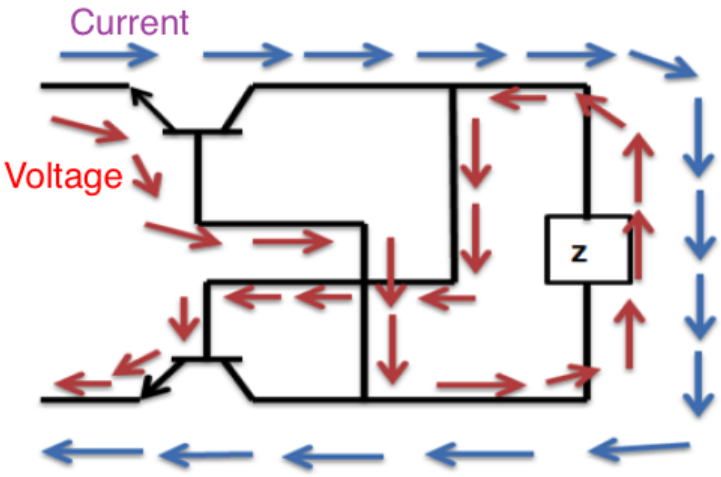

Figure 2.2: The basic voltage and current relationship in an series NFC circuit.

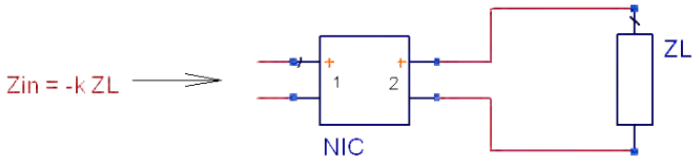

Figure 2.3: NFC as a two-port network with load transformation at the input terminals.

equal, but the input voltage is inverted at the output terminals which has been shown in Fig 2.2. The red line shows voltage (V_{BE}) while the blue line shows current (I_{CE}) that establishes the negative input impedance, seen across the emitter terminals. The two-port hybrid circuit analysis of VNICs and INICs are implemented in the next section.

2.3 Hybrid parameters representation

Any non-Foster impedance circuit can be analogized to an ideal transformer that transforms a passive load impedance to a negative impedance scaled by a factor of k as shown in Fig. 2.3. The conversion factor k is a positive integer, also known as the conversion ratio, which is equal to 1 in an ideal

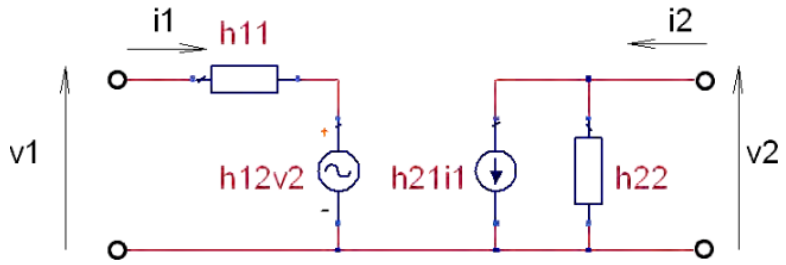

Figure 2.4: Equivalent h-model of the non-Foster impedance circuit.

case and may vary frequency for other practical applications.

The hybrid model of negative impedance can be well represented by using hybrid or h-parameters as shown in Fig. 2.4. The hybrid circuit matrix is given as

$$\begin{bmatrix} V_1 \\ I_2 \end{bmatrix} = \begin{bmatrix} h_{11} & h_{12} \\ h_{21} & h_{22} \end{bmatrix} \begin{bmatrix} I_1 \\ V_2 \end{bmatrix} \tag{2.1}$$

Hence, the circuit equations at the input and output ports are given by

$$V_1 = h_{11}I_1 + h_{12}V_2 \tag{2.2}$$

and,

$$I_2 = h_{21}I_1 + h_{22}V_2 \tag{2.3}$$

Now, if port 2 is terminated with Z_L, the impedance seen across port 1 or the input impedance is given by

$$Z_{in} = \frac{V_1}{I_1} = h_{11} - \frac{kZ_L}{1 + h_{22}Z_L} \tag{2.4}$$

where, k=$h_{12}.h_{21}$

For the condition in hybrid model, assuming h_{11}=h_{22}=0

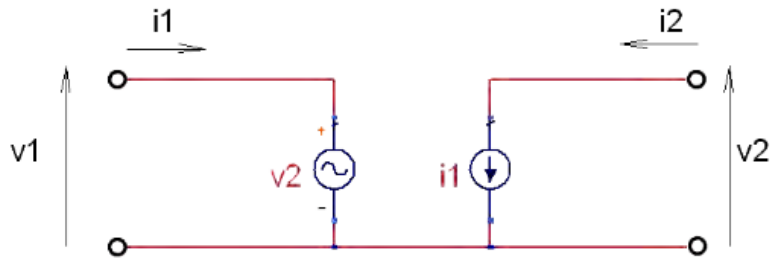

Figure 2.5: h-model of an ideal current inversion negative impedance circuit.

The input impedance becomes negative to the load value as

$$Z_{in} = -k.Z_L \tag{2.5}$$

Also, Ideally, k=$h_{12}.h_{21}$=1 and hence,

$$Z_{in} = -Z_L \tag{2.6}$$

The possibility of negative impedance here could be either by inversion of current or voltage. The current inversion without affecting the polarity of input and output voltages is known as an INIC as shown in Fig. 2.5. The h-matrix for current inversion NIC is depicted as

$$h = \begin{bmatrix} 0 & 1 \\ 1 & 0 \end{bmatrix} \tag{2.7}$$

The voltage and current relationship in the current inversion model is given by

$$I_1 = I_2 = (-I_L) \tag{2.8}$$

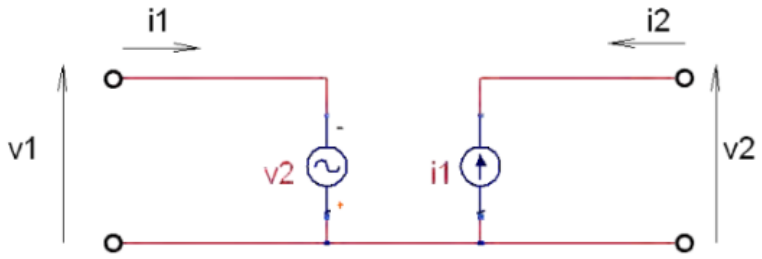

Figure 2.6: h-model of an ideal voltage inversion negative impedance circuit.

and,

$$V_1 = V_2 \tag{2.9}$$

An operational amplifier (op-amp) based NFC, as a current inversion circuit will also be discussed later in this chapter.

Similar to INIC, reversing the polarity of voltage without changing the current directions, in order to achieve negative impedance, is called VNIC as shown in Fig. 2.6. The h-matrix for voltage inversion NIC is given as

$$h = \begin{bmatrix} 0 & -1 \\ -1 & 0 \end{bmatrix} \tag{2.10}$$

The voltage and current relationship in this voltage inversion model is given by

$$I_1 = -I_2 = I_L \tag{2.11}$$

and,

$$V_1 = -V_2 \tag{2.12}$$

Thus, it is concluded that all non-Foster impedance circuits comprise of active elements that are responsible for negative impedance either by current inversion through a load while keeping the same voltage, or by voltage inversion across the load while maintaining the current through it. A bipolar

transistor-based Linvill model is a practical implementation of the voltage inversion model.

The NIC implementations are widely referred as NFCs because the negative slope of reactance contradicts Foster's theorem for lossless and passive devices which suggests the presence of a positive slope for reactance with frequency at all times. Hence, NICs and NFCs are used as synonyms throughout the thesis.

2.4 Theory of non-Foster impedance circuits

This section talks about the conventional design techniques to achieve non-Foster impedance. The circuit analysis for op-amp NFC as well as BJT-based NFC have been presented here.

A non-Foster impedance circuit is implemented using active devices along with passive elements. An op-amp based NFC is the conventional approach for low-frequency designs [28]. The NFC can also be realised in VHF band by investigating alternative design methods. A cross-coupled BJT pair with positive feedback was introduced by Linvill and has also been conveyed to this thesis [1]. Recently, a graphene-based transistor, known as the graphene field-effect transistor (GFET) has been proposed as an integrated chip, alternative to the BJT approach [29]. Few RTD-based non-Foster impedance circuits have also been presented in this chapter to attain a low form factor and high bandwidth solution. Each RTD-based NFC has only one active element and few passive components [5]. Detailed description of the aforementioned methods is presented in following subsections.

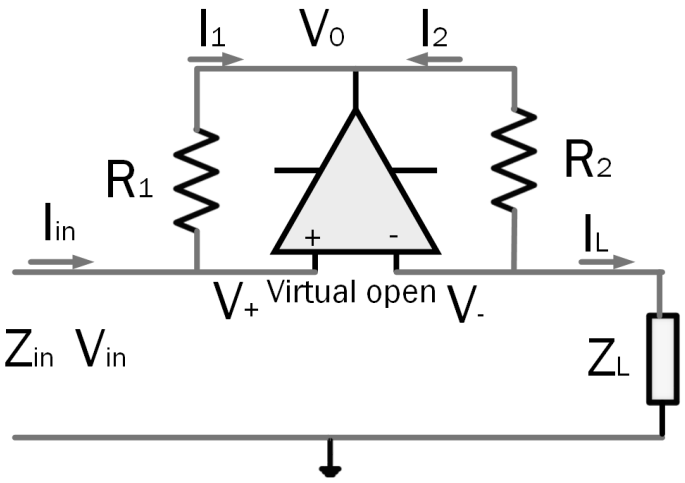

Figure 2.7: An op-amp based non-Foster impedance circuit.

2.4.1 Operational amplifier NIC model

The op-amp based non-Foster impedance circuit is a conventional approach exhibiting a positive feedback and works on the principle of current inversion, as discussed in section 2.3 [30]. As the zeros and poles of the op-amp are accurately defined, these are easy to stabilise. Also, the surface mount packages of op-amps are readily available, easy to design and less sensitive to the parasitic losses. Additionally, the design flexibility is contained due to the package solution that has high feedback gain and limited freedom of control. Due to this restriction in controlling of positive feedback large loop gain, the bandwidth is very limited and has a low operational range ($<$ 40 MHz). As shown in Fig. 2.7, the virtual open characteristics of an op-amp results in,

$$V_+ = V_- = I_L Z_L \tag{2.13}$$

and,

$$I_+ = I_- = 0 \tag{2.14}$$

The currents through the resistors are given as

$$I_1 = \frac{V_+ - V_0}{R_1} \tag{2.15}$$

and

$$I_2 = \frac{V_- - V_0}{R_2} = \frac{I_1 R_1}{R_2} \tag{2.16}$$

Hence, the current relationship in the circuit is given as

$$I_{in} = I_1 = \frac{I_2 R_2}{R_1} = -\frac{I_L R_2}{R_1} \tag{2.17}$$

Thus, the input impedance is given as

$$Z_{in} = \frac{V_{in}}{I_{in}} = \frac{I_L Z_L R_1}{-I_L R_2} = -\frac{R_1}{R_2} Z_L \tag{2.18}$$

Thus, it is shown that the negative impedance achieved due to the current I_{in} is inverted through the load Z_L. Hence, this approach is known as the current inversion method to obtain non-Foster impedance. A breadboard circuit design has been implemented to comprehend an op-amp based non-Foster impedance circuit at 10 MHz. As shown in Fig. 2.8, the current waveform observed at the output terminal is exactly in phase opposition to that of the input signal. As the polarity of voltage remains unchanged at both terminals, the current waveform undergoes inversion which implies the realisation of non-Foster characteristics. Also, the bandwidth is limited in an op-amp design due to high feedback fixed loop gain, which restricts its applications in VHF and higher frequency bands. A bipolar transistor approach with suitable biasing circuit can fine tune the loop gain and hence, the bandwidth enhancement could be envisioned.

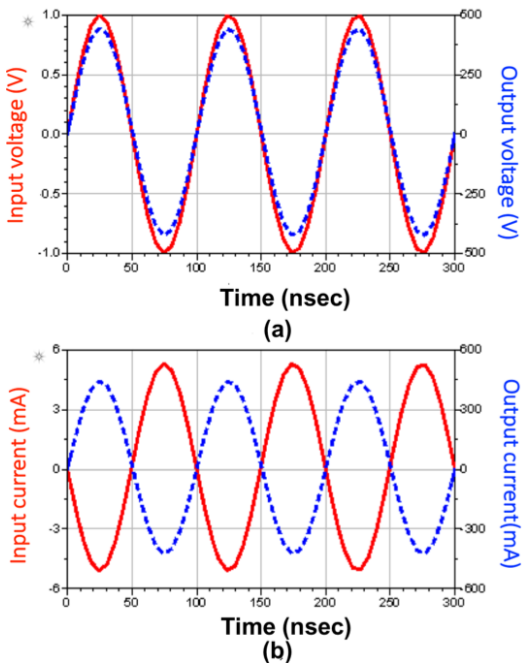

Figure 2.8: Measurements of current inverting negative impedance converter (INIC). (a) The input-output voltage across op-amp with load 1000 Ω and $R_1 = R_2$, is in-phase but attenuated for a 10 MHz waveform. (b) The input-output current is out of phase for same 10 MHz waveform.

2.4.2 Linvill's model

A BJT-based transistor design proposed by Linvill [1] provides an alternative approach to the previously mentioned op-amp based NFC. The circuit block between the load and input, which is responsible for generating negative impedance comprises of configurations that have different conversion ratio (k) [31]. This conversion ratio is dependent on the passive and the active network configuration.

Linvill model as shown in Fig. 2.9 is the focal point here, as it is highly suitable for our application. A two-port balanced floating series NFC circuit has its emitter terminals of cross-coupled transistors connected to the input port while the collector terminals are connected to load elements. This is an open-circuit model representation. On the contrary, a short-circuit model has collector terminals connected to its input port and the emitter terminals

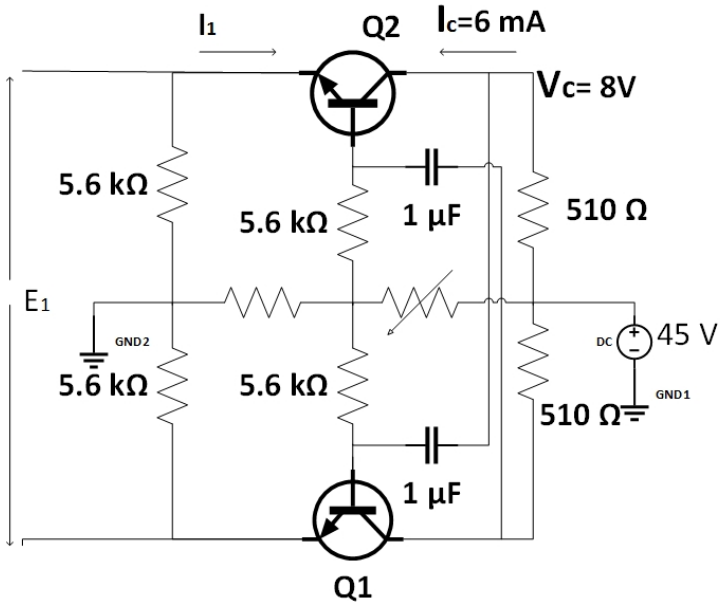

Figure 2.9: Configuration of OCS transistor based NFC by Linvill [1].

connected to the load. As shown in Fig. 2.9, the collector current of one transistor is fed to the base of the other and vice-versa. The biasing network is symmetrical for both the transistors and is isolated from the RF input-output path using dc blocking capacitors. Practically, entirety of current I_1 flows to the collector and cross-coupled back to the base of transistor. Thus, the input terminals are active due to the low emitter-base resistance, which results in the inversion of voltage across the load. An emitter resistor in the biasing network is responsible for current adjustments that assists the biasing stability. It is symmetrical to both the transistors and keeps the biasing point stable. A variable resistor is a better choice to shift the biasing point and tune the performance of transistors in order to achieve the desired non-Foster impedance.

The circuit in Fig. 2.9 can be modelled as shown in Fig. 2.10, where transistors are replaced by their equivalent circuit model with least approximations. Both the transistors are represented as T model, where emitter

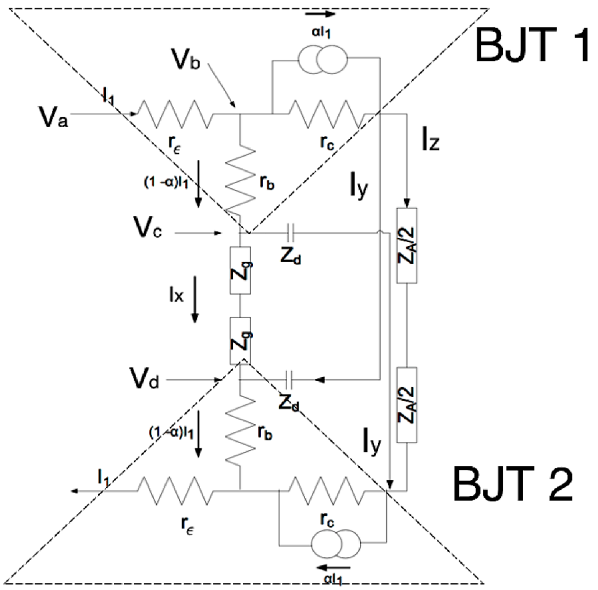

Figure 2.10: Equivalent circuit of OCS NFC circuit for circuit analysis.

and base terminals are replaced by their appropriate resistances r_ϵ and r_b respectively. α is a large signal current gain in common base transistor configuration which is defined as the ratio of collector current to the emitter current. The collector terminal is replaced by a parallel combination of current dependent current source and collector resistance r_c. Z_g and Z_d represents the base biasing current resistance and dc blocking capacitor along the feedback path respectively. As shown in Fig. 2.10, the voltage at different junctions can be calculated as

$$V_b = V_a - I_1 r_\epsilon \tag{2.19}$$

$$V_c = V_b - (1-\alpha) I_1 r_b \tag{2.20}$$

$$V_d = I_1 r_\epsilon + 1 - \alpha) I_1 r_b \tag{2.21}$$

Current, I_x through the base current setting resistance is calculated using the potential difference between V_c and V_d as

$$I_x = \frac{V_c - V_d}{2Z_g} \tag{2.22}$$

Furthermore,

$$I_x = \frac{V_a - 2I_1 r_\epsilon - 2(1-\alpha)I_1 r_b}{2Z_g} \tag{2.23}$$

Also, the current flowing through the feedback paths are given as

$$I_y = (1-\alpha)I_1 - I_x \tag{2.24}$$

and,

$$I_z = \alpha I_1 - I_y \tag{2.25}$$

Now, solving I_z and I_y in terms of V_1 and I_1

$$I_y = (1-\alpha)I_1 - \frac{V_a - 2I_1 r_\epsilon - 2(1-\alpha)I_1 r_b}{2Z_g} \tag{2.26}$$

and

$$I_z = (2\alpha - 1)I_1 + \frac{V_a - 2I_1 r_\epsilon - 2(1-\alpha)I_1 r_b}{2Z_g} \tag{2.27}$$

I_z can also be calculated by employing KVL at load loop,

$$I_z = \frac{V_d + I_y Z_d - (V_c - I_y Z_d)}{Z_A} \tag{2.28}$$

Now, equating both the equations of I_z, we get

$$V_d + 2I_y Z_d - V_c = \alpha I_1 Z_A - Z_A I_y \tag{2.29}$$

$$2I_1 r_\epsilon + 2(1-\alpha)I_1 r_b - V_a + 2I_y Z_d = \alpha I_1 Z_A - Z_A I_y \tag{2.30}$$

$$V_a - I_1(2r_\epsilon + 2(1-\alpha)r_b - \alpha Z_A) = (2Z_d + Z_A)I_y \tag{2.31}$$

Substituting I_y, we get

$$V_1 - I_1(2r_\epsilon + 2(1-\alpha)r_b - \alpha Z_A) = (2Z_d + Z_A)\left\{(1-\alpha)I_1 + \frac{V_1 - 2I_1 r_\epsilon - 2(1-\alpha)I_1 r_b}{2Z_g}\right\} \tag{2.32}$$

$$\frac{V_a}{I_1} = \frac{(2r_e + 2(1-\alpha)r_b + 2(1-\alpha)Z_g)\frac{(2Z_d+Z_A)}{2Z_g} + (2r_e + 2(1-\alpha)r_b - \alpha Z_A)}{\frac{2Z_g+2Z_d+Z_A}{2Z_g}} \tag{2.33}$$

$$Z_{in} = \frac{(2r_e + 2(1-\alpha)r_b)(2Z_d + Z_A) + 2Z_g(2r_e + 2(1-\alpha)r_b)}{2Z_g + 2Z_d + Z_A} - \frac{2\alpha Z_g Z_A - 2(1-\alpha)Z_g)(2Z_d + Z_A)}{2Z_g + 2Z_d + Z_A} \tag{2.34}$$

$$Z_{in} = \frac{(2r_e + 2(1-\alpha)r_b)(2Z_d + Z_A + 2Z_g)}{2Z_g + 2Z_d + Z_A} - \frac{2\alpha Z_g Z_A - 2(1-\alpha)Z_g)(2Z_d + Z_A)}{2Z_g + 2Z_d + Z_A} \tag{2.35}$$

$$Z_{in} = 2r_e + 2(1-\alpha)r_b - \frac{2\alpha Z_g Z_A - 2(1-\alpha)Z_g)(2Z_d + Z_A)}{2Z_g + 2Z_d + Z_A} \tag{2.36}$$

$$Z_{in} = 2r_e + (1-\alpha)\left(2r_b + \frac{2Z_g(2Z_d + Z_A)}{2Z_g + 2Z_d + Z_A}\right) - \frac{2\alpha Z_g Z_A}{2Z_g + 2Z_d + Z_A} \tag{2.37}$$

$$Z_{in} = 2r_e + (1-\alpha)\left(2r_b + \frac{2Z_g(2Z_d + Z_A)}{2Z_g + 2Z_d + Z_A}\right) - \frac{2\alpha Z_g Z_A(Z_g + Z_d)}{2Z_g + 2Z_d + Z_A}\frac{1}{Z_g + Z_d} \tag{2.38}$$

$$Z_{in} = 2r_e + (1-\alpha)\left(2r_b + \frac{2Z_g(2Z_d + Z_A)}{2Z_g + 2Z_d + Z_A}\right) - \alpha Z_P \frac{Z_g}{Z_g + Z_d} \tag{2.39}$$

Where, Z_P is the parallel combination of Z_A and $2(Z_g + Zd)$. At high frequencies, the impedance of dc blocking capacitors Z_d are nearly zero as they behave similar to a short-circuit for radio frequencies.

$$Z_{in} = 2r_e + (1-\alpha)2r_b + (1-\alpha)\frac{2Z_g Z_A}{2Z_g + Z_A} - \alpha Z_P \tag{2.40}$$

As Z_P in the absence of Z_d is equivalent to the parallel combination of Z_A and $2Z_g$. The updated equation becomes

$$Z_{in} = 2r_e + (1-\alpha)2r_b + (1-2\alpha)Z_P \tag{2.41}$$

While deriving, the approximation $\frac{Z_A}{r_c}$ is negligible, when the load and r_c are in the order of kilo ohms and mega ohms respectively. The first term has emitter resistance, r_ϵ which is inversely proportional to the emitter current ($r_\epsilon = 13\Omega$ at 2 mA). As the variation of emitter current is small due to the change in collector current, the typical value of r_ϵ is 25 Ω. The base resistance, r_b is typically few hundred ohms (200 Ω). The large signal cur-

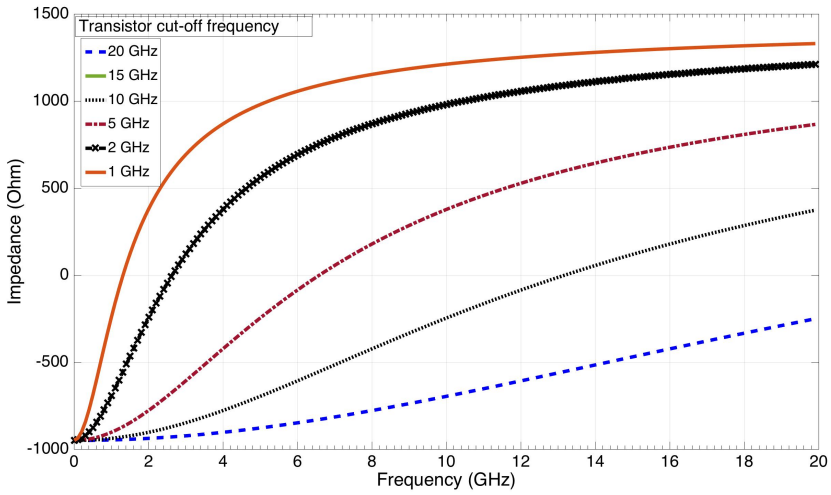

Figure 2.11: The input impedance calculation for 1k resistive load using different transistors. Transistors with high cut-off frequency offer better flatness in negative impedance.

rent gain, α is typically between 0.95 to 1 which minimises the second term in (2.41). The third term is close to -Z_P and poses to be the most dominating term offering negative impedance. Also, α is frequency dependent for transistors as

$$\alpha = \frac{\alpha_0}{1 + \frac{jf}{f_c}} \tag{2.42}$$

Where $\alpha_0 = 1$ and f_c = cut-off frequency. (2.41) and (2.42) are utilised to calculate input impedance for 1000 Ω load. Considering different cut-off frequencies of the transistor as shown in Fig. 2.11, it is observed that a transistor with high cut-off level is required for achieving a flat negative impedance. The constant negative impedance is noticeable up to one-tenth of the cut-off frequency. Hence, it is concluded that the transistor selection is very critical, and a 20 GHz cut-off frequency transistor leads operation of an NFC up to 2 GHz.

A BJT-based NFC operates on the principle of voltage inversion NFC by inverting the voltage across the load, while keeping the direction of the

current unchanged. The cross-coupled BJT has a biasing circuitry which makes it easy for tuning the loop gain of the transistor pair. Since, the product of loop gain and operational bandwidth is constant, this advantage of bandwidth control makes it useful for high-frequency operation up to VHF/UHF band. These factors encourage the development of a BJT-based NFC prototype in chapter 3 and the integration of NFC with an ESA in chapter 4.

The op-amp NFCs have limited bandwidth due to high feedback loop gain. Also, BJT-based NFCs are sensitive to parasitics as the poles and zeros are not well defined, which may further lead to high occurrences of stability issues. Various other novel design techniques for NFC implementation have also been presented in the thesis. These methodologies are broadly described in the next section.

2.5 Modern techniques for NFC design

In recent years, the NFC design has been focussed for applications beyond HF and VHF bands. Most of these NFC designs are primarily based on Linvill's model and are implemented as low-cost printed circuit technology with surface mount BJTs [32, 33, 22, 34, 35]. Apart from the conventional techniques, Weldon et al. [2] presented a simple two-transistor negative inductor which has been measured and fabricated in 0.5 μm CMOS process as shown in Fig. 2.12(a). The measured results demonstrates an inductance value of -95 nH up to 0.5 GHz, falling to -85 nH at 0.75 GHz and -63 nH at 1 GHz. An additional negative resistance of -260 Ω was also measured at low frequencies, as shown in Fig. 2.12(b) which falls down to -50 Ω at 1 GHz. This negative resistance may be mitigated with positive resistance or

may be used for gain applications.

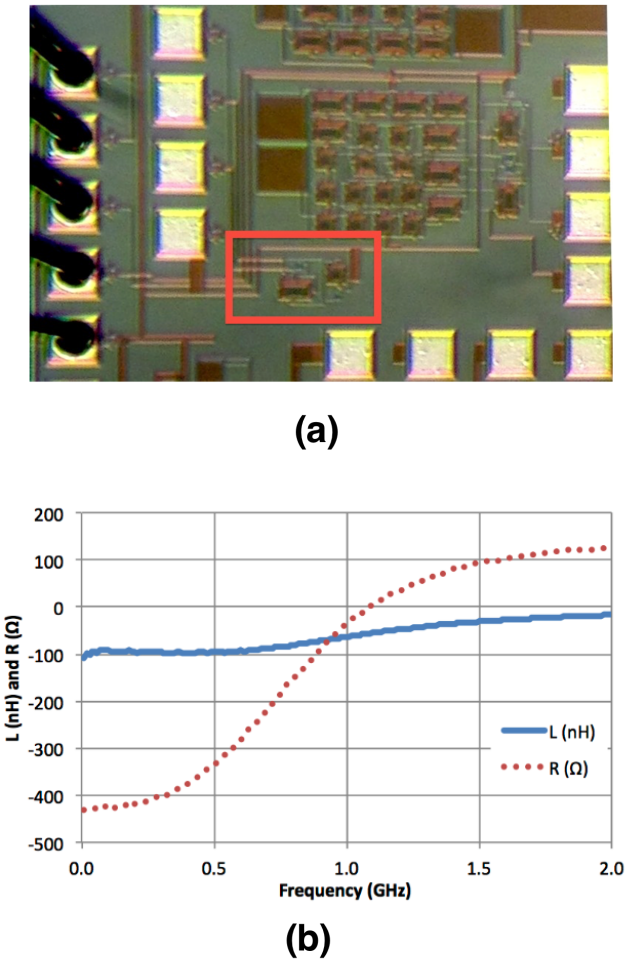

Figure 2.12: Figures from Weldon et al. [2]: (a) The red box showing the prototype negative inductance circuit. (b) The measured data from prototype circuit showing inductance (nH) and resistance (Ω).

A similar floating negative inductance is presented by White et al. [3] at HRL laboratories using the differential negative impedance inverters (NII) derived from Linvill's unbalanced NIC. The negative inductance IC has been contrived using the IBM 8 HP BiCMOS processor as shown in Fig. 2.13 which can be tuned in the range, $-64\ nH$ to $-40n\ H$. The experimental studies indicate impedance across the port to be very low. Hence, the IC is short-circuit-stable and is dc coupled at the terminals. This makes it useful

for a slot antenna to easily cancel out the susceptance.

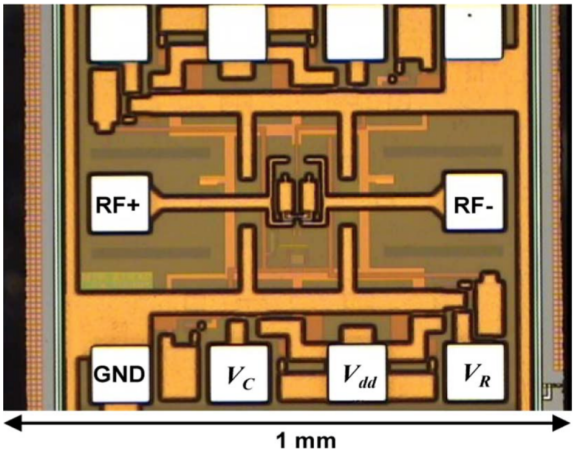

Figure 2.13: Figure from White et al. [3]: The photograph is showing the 1 mm^2 die of the negative inductance circuit.

Recently, Saadat et al. [4] presented the design and performance analysis of a negative inductor circuit based on the Linvill's open-circuit-stable topology. The inductor is implemented in a 65 nm CMOS processor, with the measurement of $-1\ nH$ from 100 MHz to 6 GHz. Additionally, a low power consumption of 5 mW was also achieved. The microphotograph of the proposed negative inductor is shown in Fig.2.14(a), whereas the satisfying agreement between simulated and measured results is shown in Fig. 2.14(b).

A GFET design is proposed [36] with an improved carrier mobility analysis. The schematic of GFET inclusive of parasitics has been shown in Fig. 2.15. An NFC implementation has been carried out using the proposed GFET approach in similarity to the BJT approach [29]. The main intention of this work is to explore the possibility of IC based non-Foster impedance circuits being similar to IC based capacitive NFC [37] and an inductive NFC [4]. The design of graphene based NFC has also been carried out in this chapter 3.

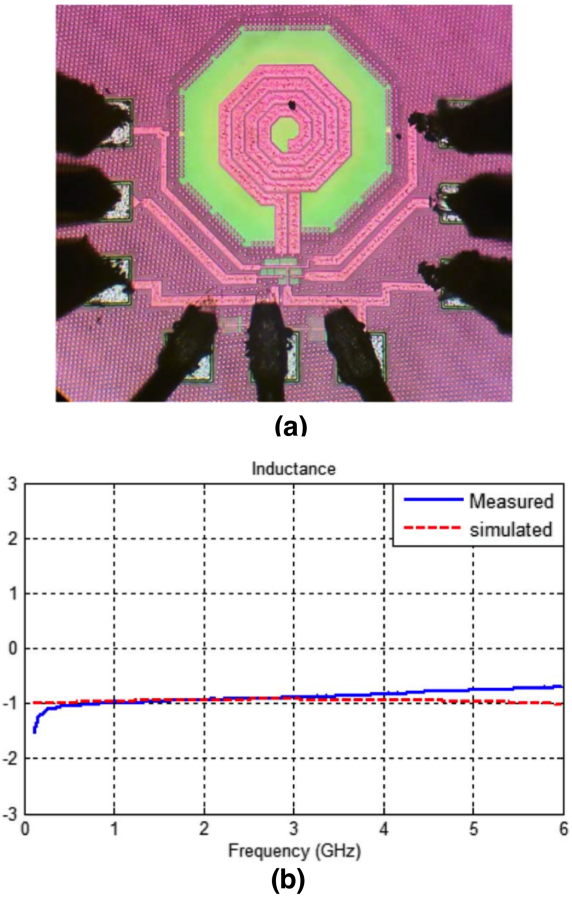

Figure 2.14: Figures from Saadat et al. [4]: (a) Microphotograph of the proposed negative inductor. (b) The comparison between measured and simulated negative inductance.

Further improvement to negative impedance generation accompanied by the development of GaAs fabrication process is materialised by the negative differential resistance based technique [38]. The tunnel diode is a p-n junction device in which, the voltage increases as the current through it decreases (exhibits negative resistance). The depletion region then, becomes thin (10 nm) as the p and n region are highly doped. The Fermi level moves above the conduction band for n-type and below the valence band for p-type such that the electrons freely move from the conduction band of n-region to the valance band of p-region. It is noteworthy that, the energy of particles do not change during this phenomenon. The fundamental limitation in

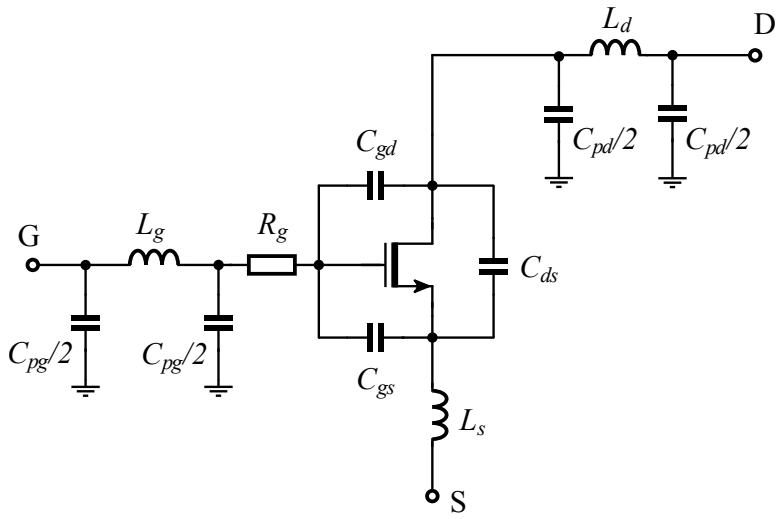

Figure 2.15: Schematic of GFET with parasitics inclusion.

the IC fabrication of a tunnel diode is its high junction capacitance. Chang [39] proposed the double-barrier structure having a thin GaAs sandwiched between two GaAlAs barriers shown in Fig. 2.16(a). The scanning electron microscope (SEM) of a quantum barrier RTD developed at the University of Leeds is also shown in Fig. 2.16(b). An RTD structure, when biased just beyond resonance, has a negative differential resistance (NDR) and a negative slope in the current versus voltage characteristics as shown in Fig. 2.17. This NDR region is the operating point of the RTD as a negative resistance device, which is also used for the negative element designs and finally for non-Foster matching networks. The RTD fabricated is sample biased at a negative differential resistance and offers -50 Ω resistance and a relatively low inductance as shown in Fig. 2.18.

As previously discussed, one of the most well-known NFC topologies is the BJT-based NFC where a BJT pair flips the direction of current (or voltage) through a load while maintaining the polarity of voltage (or current). Due to size constraints, it is difficult to incorporate these BJT-based NFCs within each element of the periodic MTM structure. Alternatives to the

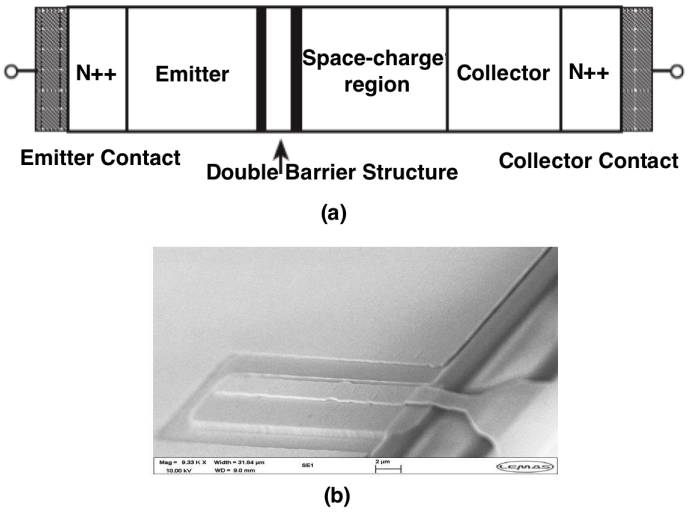

Figure 2.16: Design process of resonant tunnelling diode: (a) Double barrier structure of resonant tunnel diode. (b) SEM of a quantum barrier resonant tunnelling diode.

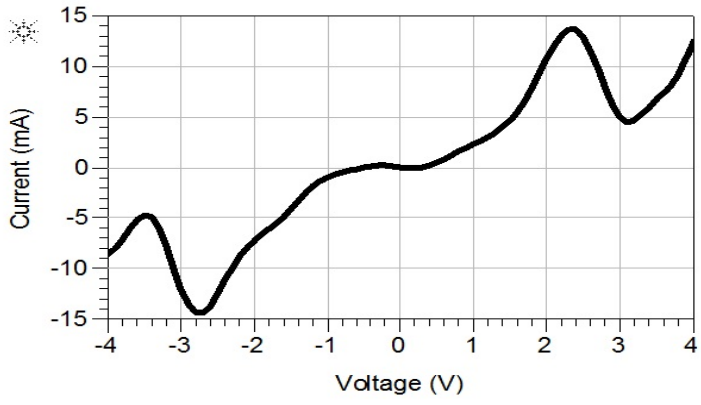

Figure 2.17: Current-voltage characteristics of diode showing negative resistance region for RF characterisation.

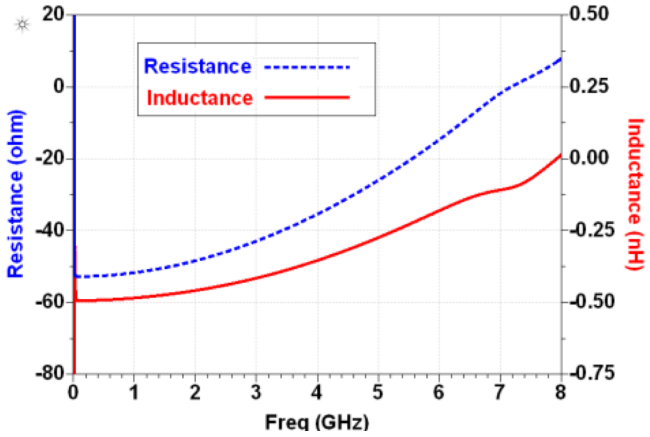

Figure 2.18: The resistance and inductance across the diode operating at negative resistance biasing region i.e. 2.75 V.

Linvill NFC approach have also been implemented through SiGe BiCMOS processes to overcome size limitations, parasitics reduction and to extend operational frequencies [4, 40]. A unique feature in RTD-based NFCs is the very low power consumption as compared to BJT-based designs which has also been presented in this thesis. Also, apart from the RTD, all circuit elements here are passive in nature. Thus, once a potentially stable RTD is established, it highly reduces the complexity of the circuit realisation process. Chapter 3.4 is dedicated to the implementation of RTD-based negative impedance that includes detailed designs. The next section discuss the practical challenges to realise a negative impedance device.

2.6 Compensation network for non-Foster circuits

Practical realisation of the aforementioned design approaches, except for the op-amp based design, is cumbersome due to their inherent potential instability. This section will provide an overview on the requirements of

the compensation circuits followed by the specific values of components needed to overcome the oscillatory behaviour of the NFCs. A non-ideal NFC has non-zero h_{11} and h_{22} which needs to be compensated using a passive network for making them approach wizero [41]. A passive network in series with the practical NFC at one port and in shunt at the other port can make the overall two-port network as an ideal NFC ($h_{11} = h_{22} = 0$). By circuit analysis of h matrix of the overall network with the inclusion of compensation network is given as

$$H = \begin{bmatrix} \frac{h_{11}+Z_2\Delta h}{1+h_{11}Y_1+h_{22}Z_2+Y_1Z_2\Delta h} & \frac{h_{12}}{1+h_{11}Y_1+h_{22}Z_2+Y_1Z_2} \\ \frac{h_{21}}{1+h_{11}Y_1+h_{22}Z_2+Y_1Z_2\Delta h} & \frac{h_{22}}{1+h_{11}Y_1+h_{22}Z_2+Y_1Z_2\Delta h} \end{bmatrix} \tag{2.43}$$

Where, $\Delta h = h_{11}h_{22} - h_{12}h_{21}$ An ideal current inversion NFC has a h matrix as

$$H = \begin{bmatrix} 0 & h_{12} \\ h_{21} & 0 \end{bmatrix} \tag{2.44}$$

Now, let $k = h_{12}.h_{21}$ Comparing (2.43) and (2.44),

$$Z_2 = \frac{-h_{11}}{\Delta h} \tag{2.45}$$

$$Y_1 = \frac{-h_{22}}{\Delta h} \tag{2.46}$$

Substituting (2.45) and (2.46) in (2.44), we get

$$H = \begin{bmatrix} 0 & -\frac{\Delta h}{h_{21}} \\ -\frac{\Delta h}{h_{12}} & 0 \end{bmatrix} \tag{2.47}$$

Also, the conversion factor k is

$$k = \frac{\Delta h^2}{h_{12}h_{21}} \tag{2.48}$$

Since, Z_2 and Y_1 are positive passive network elements, k factor is also positive. So, we arrive at two possible sets of conditions, Condition I

$$h_{11} \geq 0$$
$$h_{22} \geq 0$$
$$\Delta h < 0$$
$$h_{12}h_{21} > 0$$

and Condition II

$$h_{11} \leq 0$$
$$h_{22} \leq 0$$
$$\Delta h > 0$$
$$h_{12}h_{21} > 0$$

Condition I will be satisfied when

$$h_{11}h_{22} < h_{12}h_{21}$$

And, condition II will be satisfied when

$$h_1 1 h_2 2 > h_{12}h_{21}$$

When h_{11} or h_{22} of the non-ideal NFC is zero, only one compensation network is sufficient. If,

$$h_{11} = 0$$

(2.45) and (2.46) respectively becomes

$$Y_1 = \frac{h_{22}}{h_{12}h_{21}}$$

$$Z_2 = 0$$

Else,

$$h_{22} = 0$$

then, (2.45) and (2.46) respectively becomes

$$Z_2 = \frac{h_{11}}{h_{12}h_{21}}$$

$$Y_1 = 0$$

In both these cases, the h matrix of the compensated network is made up of non-ideal NFC having both non-zero h_{11} and h_{22} as shown in (2.48) is

$$k_{bothnonzero} = \frac{\Delta h^2}{h_{12}h_{21}} \tag{2.49}$$

and the conversion factor of compensated network made up of non-ideal NFC having either h_{11} or h_{22} is zero

$$k_{onenonzero} = h_{12}h_{21} \tag{2.50}$$

As we proceed, the condition to be satisfied is

$$\Delta h < 0$$

That means

$$h_{11}h_{22} < h_{12}h_{21}$$

$$\frac{h_{11}h_{22}}{h_{12}h_{21}} < 1 \tag{2.51}$$

We know that

$$h_{11}h_{22} > 0$$

Also,

$$h_{12}h_{21} > 0$$

It means

$$\frac{h_{11}h_{22}}{h_{12}h_{21}} > 0 \tag{2.52}$$

Using (2.51) and (2.52),

$$0 < \frac{h_{11}h_{22}}{h_{12}h_{21}} < 1 \tag{2.53}$$

Simplifying (2.49) further and using the above condition in (2.53)

$$\frac{k_{bothnonzero}}{h_{12}h_{21}} = \left(\frac{h_{11}h_{22}}{h_{12}h_{21}} - 1\right)^2 \leq 1$$

$$k_{bothnonzero} \leq h_{12}h_{21}$$

Now, using (2.50),

$$k_{bothnonzero} = k_{onenonzero} \tag{2.54}$$

From (2.53), it is concluded that the compensated network with both non zero h_{11} and h_{22} for non-ideal NFC has k less than the same network having one of the h_{11} or h_{22} as zero. This verifies that later case is a better prospect to achieve the input impedance as close to the load impedance. Also, it is a good practice to design the circuit in such a manner that either h_{11} or h_{22} could be approximated to zero. The addition of passive terminations control the location of poles and zeros and hence, brings stability to the overall circuit which is further discussed in next section.

2.7 Stability of non-Foster circuits

As mentioned earlier, the stability of such circuits alone is challenging as the negative impedance leads to oscillatory behaviour. An NFC is analysed

as h parameter matrix, and this h parameter intend to be useful for the stability and noise analysis of the circuit. One of the main challenges for NFC design, as with any other active component, is its stability. [42, 43] explored that when the first port of an NFC is passively loaded, it would lead to open-circuit stability (OCS) or short-circuit stability (SCS) at the second port. Also, loading of the second port with the same element leads to short-circuiting stability (SCS) or open-circuit stability (OCS) at the first port. Also, Brownlie [44] described that any ideal NFC (dc coupled) is inevitably open-circuit-unstable (OCU) at one port and short-circuit-unstable (SCU) at the other port. Hoskins observed that a very simple deviation from the ideal scenario is sufficient to reproduce the stability phenomenon in practical circuits [45].

Recent work by Stearns ([46], [47]) verifies that pole-zero analysis is not suitable for the high-order complex networks. It has also been inferred that the μ test for unconditional stability [48] is not appropriate for NFCs. The Routh-Hurwitz stability technique and frequency domain Nyquist criterion, which was previously congregated by Rajab et al. [49] considers the natural frequencies of the complete circuit and convinces to useful for NFC stability analysis.

As discussed, the stability analysis of an NFC has not been performed using the standard amplifier stability tests like μ test, k test, etc. The Nyquist criterion has been introduced in order to conduct stability testing in the frequency domain. It provides stability margins and a design procedure that allows us to engineer the composite materials to ensure stability over a range of structural geometries and periodicities. Hence, this technique is highly preferred for the further integration of the NFCs in the active MTM structures.

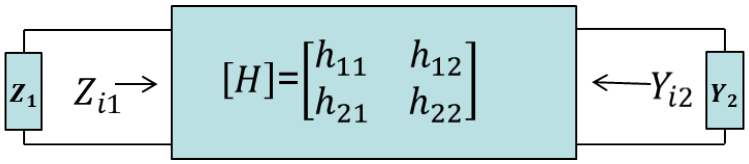

Figure 2.19: Two-port h-model of NFC circuit with passive terminations for stabilisation.

The fundamental study of NFC stability has been performed using the h-matrix in a two-port network as shown in Fig. 2.19. A practical or non-ideal NFC has a non-zero h_{11} and h_{22} which requires a passive compensation network to approximate them to zero. A passive network in series with a practical NFC at one port and a passive shunt network at the second port can make the overall two-port network to operate as an ideal NFC (h_{11}= h_{22}=0). In an NFC with a compensated circuit, the load impedance connected across the output port appears to be a negative impedance at the input port. The stability of NFC is dependent on the passive network connected to it. As a result, when performing the stability analysis of NFC, it is essential to consider the complete system (the NFC and its terminating network together). In a practical circuit, the open and short-circuit conditions are determined by large and small impedances respectively. Practical NFCs are SCS and OCU at one port and OCS and SCU at the other to achieve stability. SCS implies almost zero impedance at one port and hence no zeros are defined on the right half of s-plane. Also, OCS indicates almost infinite impedance at another port and hence no poles are defined on the right half of s-plane. This approach is valid if an NFC and its terminating network are linearly dependent on the frequency. On the contrary, if it is non-linearly dependency on frequency with SCS-OCU at one port and OCS-SCU at the other port, it is essential to prove that the NFC is voltage controlled at one port and current controlled at the other port.

Stability problem is a trivial issue in an ideal NFC ($h_{11} = h_{22} = 0$) due to its symmetry and the fact that both the ports are identical. However, for a practical NFC, it is required to be concerned about the stability issues. Consider a practical non-ideal NFC having h matrix as

$$h = \begin{bmatrix} h_{11} & h_{21} \\ h_{12} & h_{22} \end{bmatrix}$$

It is terminated by Z_1 and Y_2 as shown in Fig. 2.19

$$V_1 = h_{11}I_1 + h_{12}V_2$$
$$I_2 = h_{21}I_1 + h_{22}V_2$$

substituting $I_2 = -V_2Y_2$

$$V_2 = -\frac{h_{21}}{h_{22}Y_2}I_1 \tag{2.55}$$

That gives,

$$Z_{i1} = \frac{V_1}{I_1} = \frac{h_{11}h_{22} - h_{12}h_{21} + h_{22}Y_2}{h_{22} + Y_2} \tag{2.56}$$

Similarly,

$$Y_{i2} = \frac{h_{11}h_{22} - h_{12}h_{21} + h_{22}Z_1}{h_{22} + Z_1} \tag{2.57}$$

In general, Z_1 and Y_2 are the passive and positive real rational functions.

$$Z_1 = \frac{N_1(s)}{D_1(s)} \tag{2.58}$$

and

$$Y_2 = \frac{N_2(s)}{D_2(s)} \tag{2.59}$$

substituting (2.58) and (2.59) in (2.56) and (2.57) respectively, we get

$$Z_{i1} = \frac{\Delta h D_2(s) + h_{11}N_2(s)}{h_{22}D_2(s) + N_2(s)} \tag{2.60}$$

$$Y_{i2} = \frac{\Delta h D_1(s) + h_{22} N_1(s)}{h_{11} D_1(s) + N_1(s)} \tag{2.61}$$

And as per the condition I discussed earlier, rewriting the cases again

$$h_{11} \geq 0$$

$$h_{22} \geq 0$$

$$\Delta h < 0$$

$$h_{12} h_{21} > 0$$

Both the denominators of $Z_{i1}$and Y_{i2} have positive coefficients as these are Hurwitz polynomials. It also implies that, the input impedance and output admittance cannot have right half s-plane poles (decaying with time and stable). At poles, we get infinite input impedance (open-circuit) and infinite output admittance (short-circuit). This leads to OCS at port 1 and SCS at port 2. As $\Delta h < 0$, the numerators of both Z_{i1} and Y_{i2} have negative coefficients and hence, the input impedance and output admittance have left half s-plane zeros (unstable). At zeros, we get zero input impedance (short-circuit) and zero output admittance (open-circuit). This leads to SCU at port 1 and OCU at port 2. It concludes that two types of NFCs exists when its output port is terminated with a passive load.

(a) OCS NFC: have OCS at the input port and SCS at the output port. In the case of BJT-based NFC, it has emitters at the input-output ports of NFC.

(b) SCS NFC: have SCS at the input port and OCS at the output port. In the case of BJT-based NFC, it has collectors at the input-output ports of NFC.

While working on the NFC design process, the focus is mainly on the OCS NFC. This means that the compensation network connected with the load in shunt position and for the input, it is connected in a series position.

These components are quite different from the termination components, and the conditions for an NFC stability is given as

$$R_s < R_i \text{ (Short-circuit-stable)}$$

$$R_s > R_i \text{ (Open-circuit stable)}$$

If the above two conditions are not satisfied, the NFC becomes unstable and exhibits oscillations. Sussman-Fort recommended that the above mentioned inequalities shall be satisfied by at least a factor of two [33].

2.7.1 Routh-Hurwitz stability technique

The stability of NFC is determined by the location of its poles in the complex plane; the location of poles in the right-half of complex plane will imply instability. Routh-Hurwitz stability technique [50, 51] is used to identify the stability of NFC loaded loop. Khalid [49] verified that a negative inductor in series with the loop will always be unstable, however, a parallel negative RLC can be designed to be stable. In (2.60) and (2.61), the location of poles or zeros can be identified using the Routh-Hurwitz stability criterion. The polynomial is expanded and coefficients are placed in the Routh array [x,y]. The number of sign change occurrences in the first column decides the number of roots located on the right-hand side of s-plane which leads to the instability.

Stability techniques such as the Routh-Hurwitz criterion may be sufficient for an ideal or simple loaded two-port devices, but may pose difficulties when the fabricated NFC deviates from the ideal lumped component model. It is notable that, the lumped component model can be modified with the addition of an inductor, capacitor and/or a resistor. This process leads to the formation of a higher order characteristic polynomial of the

aforementioned technique and the associated analytical solutions will become more cumbersome. Also, as the NFC circuit will inevitably exhibit some variation from the ideal model, application of the Routh-Hurwitz criterion or even root finding would potentially require complicated fittings to implement higher order equivalent circuits. The Nyquist criterion will allow stability testing for periodic structures along with providing quantification of the stability margins in frequency domain. The Nyquist contour plot generated with the product of source impedance Z_s and load admittance Y_L are analysed to verify the stability at a given operating point.

2.7.2 Nyquist stability criterion

For higher order characteristic polynomials, calculations become increasingly cumbersome. Meanwhile, the NFC prototype will exhibit some variation from simulations or ideal NFC. Also, the parasitic effects in practical cases lead to the increased complexity in finding the roots from higher order characteristic polynomials. Frequency domain technique using Nyquist stability criterion would be the preferred option in such a scenario [52]. The Nyquist criterion will facilitate stability testing for periodic structures and also provide the stability margins in frequency domain. The Nyquist contour generated with the product of source impedance (Z_s) and load admittance (Y_l) is kept under analysis to verify the stability at a given operating point. Fig. 2.20 shows the block diagram of the NFC with stability components. Nyquist criterion [11] is based on the Cauchy's argument principle [53, 54], where the product $Z_s(s)Y_l(s)$ maps to a closed contour, C into the complex plane. This contour has an arc of an infinite radius that completely encloses the right-half of the complex s-plane. $Z_s(s)Y_l(s)$ is analytic within the contour C except at a finite number of poles and also with neither poles

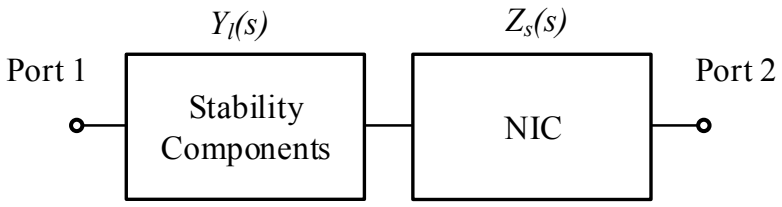

Figure 2.20: Stability element in series with floating two-port NFC to overcome stability issues.

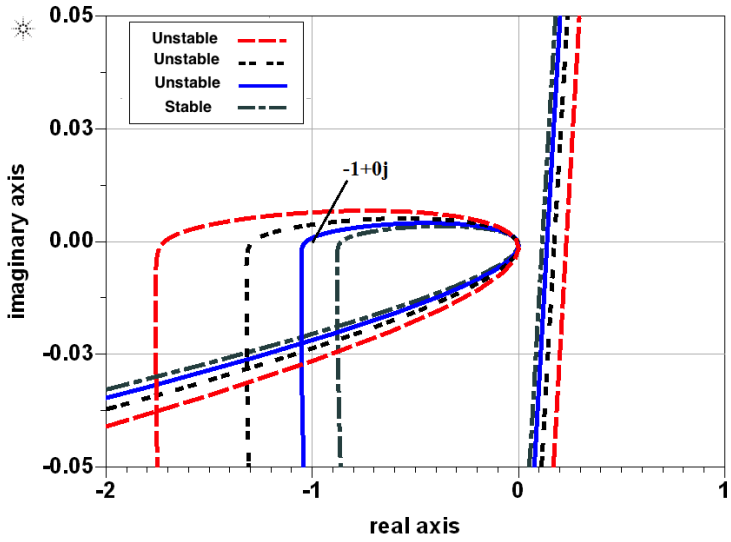

Figure 2.21: Frequency domain stability analysis using Nyquist contour: the encirclement of -1 implies unstable behaviour and adequate passive element results stability.

nor zeros on C. As per the Cauchy's argument principle,

$$N = Z - P$$

where, Z and P are the number of zeros and poles of $Z_s(s)Y_l(s)$ in C respectively while N is the number of encirclements of origin, considered in the same sense as C.

The number of clockwise encirclements of -1 with Nyquist contour of $Z_s(s)Y_l(s)$ describes the number of unstable poles of the closed loop system. So, an OCS NFC will have all impedance poles (or admittance zeros) in the left-half of the s-plane. Also, the admittance poles (or impedance zeros) of SCS NFC are located in the left-half s-plane only.

In a practical system, it is possible to set the condition that a stable system will not have any encirclement of the -1 point. An OCS NFC will have all impedance poles (or admittance zeros) in the left-half of s-plane and is therefore, represented by the source impedance. Conversely, the admittance poles (or impedance zeros) of an SCS NFC are located in the left-half plane only, so, the SCS NFC is represented by a load admittance. Fig. 2.21 shows the contour encircled -1 which has one pole in the right plane leading to instability. To eliminate -1 encirclement, selective stability components can be connected in series with the NFC. In a practical design, the parasitic effects are difficult to estimate to evaluate specific passive element requirements. A suitable load is sufficient to eliminate the -1 encirclement as shown in Fig. 2.21.

The previous literature provides both, the different design methodologies and the analysis of stability techniques. Subsequently, it is possible to apply these circuits to a practical antenna matching network in order to overcome the performance limitations of antennas and especially for ESAs.

2.8 Performance limitations of small antennas

The antenna resonance is achieved with the use of a matching network which usually consists of passive elements to resonate the reactance of antenna. These passive matching elements are capacitors for the inductive loop antennas and inductors in the case of a capacitive monopole. Passive matching technique always results in a narrow bandwidth due to the fundamental limitations of the antenna size as discussed earlier in chapter 1. Therefore, a different matching network is necessarily required to optimise the antenna operation at different frequencies. Furthermore, the availabil-

ity of tunable elements and switching mechanisms within the antenna or matching network is essential for variable frequency operation. However, the instantaneous bandwidth is always narrow.

An antenna operating in the 2.4 GHz band is relatively small compared to those in the VHF or UHF bands, due to the fundamental limit of Q that was envisioned by Wheeler [6]. An ESA at low frequency is hard to match owing to its high reactance and low radiation resistance. Chu [7] evaluated an approximate fundamental limit of minimum Q for different sizes of ideal antenna enclosed in a hypothetical sphere. This circuit model is based on the wave impedance of the spherical mode fields. Harrington [8] included circularly-polarized antennas in the existing Chu's limit and also related the effects of antenna gain, size and minimum Q for the near and far-fields. Later, Collin and Rothschild [9] and Fante [10] predicted that it is impossible to isolate the reactive field energy and radiated field energy due to their constant non-zero interaction. They all derived their minimum radiation Q based on a radiative field, travelling radially at the speed of light to enable the estimation of remaining non-radiated field. McLean [11] estimated an exact expression for minimum Q assuming the fact that the field components with $1/r^2$ are contributing to radiation energy and all other are non-radiated components. Yaghjian and Best [14] derived various methods of Q-estimation for different small dipole-type antennas and verified that the Q is nearly 1.5 times the Q derived through Chu's formulation when the radiating element configuration made optimum use of the volume within the circumscribing sphere. Thal [16] proposed a new Q, which includes the energy stored inside the imaginary sphere of the antenna, which was ignored in Chu's estimation. Moving ahead with Thal's work, Hansen and Collin [55] derived Q formulas for the lower-order TM mode. Next section

discusses the background of non-Foster inclusion in small antennas which is conveyed throughout this thesis.

2.9 Non-Foster matching for small antennas

Attempts have been made to match these high-Q small antennas and obtain bandwidth performance with non-Foster antennas (NFAs) being one of the solutions. As discussed previously, the NFC disobeys Foster's reactance theorem in where any passive, lossless and n-port network has a reactance or susceptance slope which is always proportional to the frequency [20]. In an NFA equivalent circuit, the impedance locus on Smith's chart may indicate anti-clockwise movement with increasing frequency due to the negative inductance or capacitance. Poggio and Mayes firstly proposed the application of NFCs for antenna bandwidth enhancement [56], where several NFCs were added to each line of a dipole arm. Later, they extended their work using an op-amp based non-Foster matching at the input of a dipole antenna. The former work on non-Foster matched antennas has been related to Q reduction of the antenna while the latter has been associated with the matching of high Q passive antennas using non-Foster elements. In practice, a small passive antenna is an arbitrary load with high Q with its maximum bandwidth (using passive lossless elements) limited by the Bode-Fano limit, irrespective of the number of matching stages. The theoretical work done so far was first experimentally seen by Bahr [57] by using current inverting NFC with a short monopole. Skahill [58] and Sussman [33] also continued similar work for significant improvements in bandwidth. This non-Foster behaviour can be achieved with bipolar junction transistor-based circuit models [1], CMOS circuitry [37], [4] and resonant tunnel diode based

circuits [5].

An attempt to match two-port antenna on one or both the ports has been done using the switchable or tunable matching networks, which has been presented in [59]. At low frequency, the wavelength is large and the antenna size becomes electrically small. Thus, it is inferred that the instantaneous bandwidth is proportional to the operating frequency. Also, it can be justified that matching of an antenna in the HF/VHF bands is difficult due to the fundamental antenna size limitations. An alternative approach to the passive matching has been achieved through broadband matching that matches the antenna impedance directly to the input impedance of an LNA [60]. This alternate impedance matching approach requires only a few components when compared to 50 Ω matching which indicates its clear advantage. Additionally, a gain improvement of at least 7 dB has been idealised in [61]. A comparative study of antenna-LNA co-design has been performed where one is matched to a 50 Ω with passive elements and the other has been co-designed with an antenna while maintaining the same transistors and bias conditions. A cylindrical monopole with an infinite ground plane, length of 60 cm and diameter of 10 cm in [62] operates between 30 MHz and 90 MHz. In this work, the input impedance of the antenna has been evaluated using an antenna model. An L-shaped matching network including two inductors of 477 nH and 51.9 nH respectively, obtains the matching at 60 MHz. A two-port model representation is also developed to compute the radiation efficiency of passively matched antenna. The efficiency of this passively matched antenna has been observed to be approximately 80 $\%$ with a narrow bandwidth of 3 MHz. In non-Foster matching approach, a series combination of -8.657 pF and -234.17 nH results in matching from 36 MHz to 90 MHz with an overall efficiency of 95 $\%$ throughout the band

[62].

An ESA can be modelled by its radiation resistance which is directly proportional to the squares of its operating frequency as well as the frequency independent reactive component. However, the reactive part of corresponding negative components is subjected to cancellation by matching a small resistance component with an inductive T transformer [63]. Two series inductors and a negative shunt inductor cancels out the frequency dependency of resistance and increases its value for resistive matching. Optimum selection of the inductor values is key in determining the final resistance value, i.e. 50 Ω [64].

The earliest works on non-Foster matching was proposed by A.D. Harris et al. using test antennas in [65]. The gain enhancement using a negative capacitor has been observed on a 16-foot unmatched whip antenna in the frequency band of 0.5 MHz-10 MHz. An equivalent lumped circuit for the input impedance of electrically small monopole antenna could be modelled as a capacitor with series radiation resistance. As the Q of antenna is high, the parallel equivalent circuit is also valid and has been represented as a parallel combination of radiation conductance and capacitance as shown in Fig. 2.22. The antenna capacitance then cancels out by the negative capacitance achieved due to non-Foster impedance circuit. However, the noise introduced by active elements in a non-Foster matched antenna was not considered and the performance was predominantly limited by external noises. Additionally, dynamic range and non-linear performance of non-Foster impedance have also been discussed by Harris. Two transmit antennas operating at two adjacent frequencies and a non-Foster impedance matched antenna have been considered as transmitter and receiver respectively. Three set of signals have been transmitted by this antenna pair:

two large signals, combination of a large and small signal and two small signals. The received power has been measured for each case. A large power reception has been recorded in the case of non-Foster impedance matched antenna due to its non-linear effects. Also, a conjugate reactive load element has been suggested for bandwidth enhancement in inductive dipole antennas by Poggio and Mayes in 1971 [66, 67]. The conjugate impedance matching term was introduced by Perry in 1973 to emphasise the partial realisation of active circuit based complex conjugate matching [68]. The maximum power transfer between generator and an antenna can be achieved when the internal impedance of generator is equal to the complex conjugate of antenna's input impedance. The non-Foster matching elements are all negative capacitors and the attained bandwidth attained has been in the range of 0.3 MHz-2.5MHz. Three active matching networks are also proposed; two of them are voltage inversion non-Foster impedance circuits implemented with op-amps, whereas, the third is a current inversion non-Foster impedance circuit which involves a transistor-based design topology.

An op-amp based NFC is used with a short monopole and low-noise preamplifier to achieve matching in the range of 30 MHz to 60 MHz in 1977 [57]. The realisation of a stable negative inductor is a cumbersome design procedure which is also difficult to implement in practical circuits.

Sussman-Fort has contributed to non-Foster matching of small antennas in the last decade [69], [70], [71], [72], [73], [74] and summarised in [33]. Unlike the previous one-port grounded shunt connected non-Foster impedance element, Sussman-Fort has proposed a floating series non-Foster impedance matching. Here, a negative capacitance in a shunt configuration with a small monopole antenna has been employed to reduce its overall

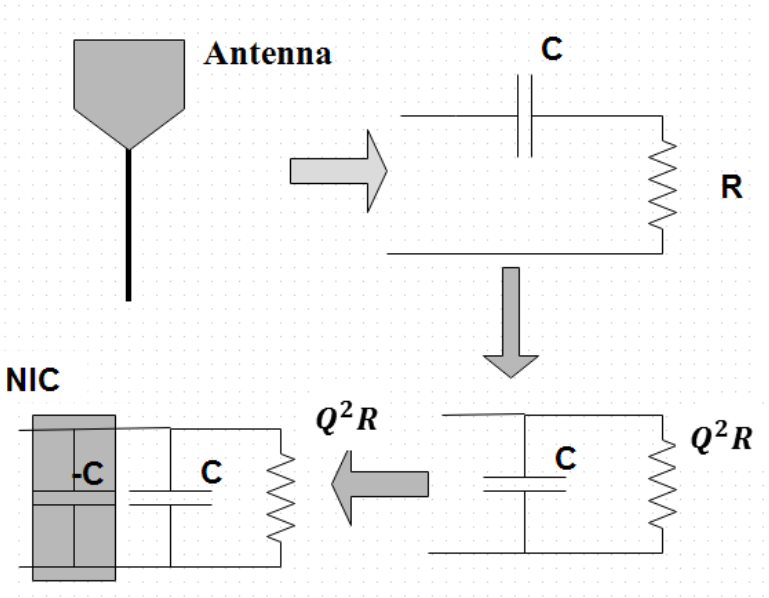

Figure 2.22: Parallel equivalent circuit model for a high Q electrically small monopole antenna using a shunt NFC.

reactance only for low frequencies as the parallel capacitance-conductance antenna model is valid only at low frequencies. Also, a series negative capacitance obtained from a non-Foster impedance circuit has been considered to attain the high-frequency performance. Sussman-Fort implemented the balanced Linvill based OCS NFCs using a cross-coupled BJT pair as a non-Foster impedance matching series element. Both gain and SNR improvement from 20 MHz to 120 MHz has been recorded [33]. Also, it is recommended that a negative LC matching network associated to an ESA could resolve the high voltage problems in transmit mode. To improve the power efficiency of antennas in transmit mode, class B and C biased non-Foster impedance circuits have been introduced.

Similar to the Harris approach [65], a recent experimental study shows that the reactive part of capacitive antennas can also be matched with a grounded shunt NFC [75]. An alternative approach to achieve the non-Foster matching using RTD-based circuits has been proposed in [5], whereas

chapter 3 discusses the development and measurement of a series floating non-Foster matching circuit to different capacitive ESAs. The antenna designed here is meander line shaped with low-frequency dependence on the desired frequency band and also has a low input resistance. Apart from the negative capacitance, additional positive resistance is offered by the NFC which increases the real input impedance. The inclusion of resistor affects the radiation efficiency and thus, the realised gain of antenna to a certain extent. However, by using a highly unstable inductive T-transformer and extra negative resistance components, the additional resistive matching can be avoided. The effect of capacitive non-Foster matching could then be realised with this slightly degraded but resistively matched antenna.

2.10 Summary

This chapter summarises the background for the realisation of non-Foster impedance through different design approaches, including conventional active elements (op-amp and BJT), as well as novel techniques. The focus of this thesis is the development of a two-port OCS NFC, which is suitable for our antenna applications. Also, the stability analysis has been accomplished which is essential for the practical realisation of these NFCs. h-parameters have also been discussed for realisation of NFCs, and evaluation of the stability conditions. A theoretical background about small antennas and various non-Foster matching techniques have been put forth in detail. Overall, this chapter forms the basis of the research contributions presented in the next chapters.

Chapter 3

Development of Non-Foster Impedance Circuits

This chapter presents the design and development of BJT-based NFC prototypes. The prototype of the two-port OCS, floating and BJT-based negative capacitance NFC has been developed and measured. The measurement results shows good agreement up to 1 GHz with the simulation results. The NFC design form factor is 40 mm by 20 mm including the biasing circuitry, which has been isolated from the RF path by dc blocking the capacitive and inductive choke elements.

A similar design approach has been implemented using a graphene device where both the BJTs have been replaced by a graphene FET model. The purpose of the GFET is to verify the desired performance and explore the possibilities of integrated chip solutions for realising the non-Foster characteristics.

Furthermore, it covers a compact non-Foster impedance solution based on the negative differential resistance devices. The negative resistance devices are fabricated and utilised as building blocks in various NFC designs.

The RTD-based device is capable of creating an effective negative inductance from a capacitive load, or a negative capacitance from an inductive load. Later, the operation, modelling and fabrication of the RTD has also been described. Since stability of any active device is an important design consideration, the RTD stability has also been analysed. Finally, the RTDs have been implemented to realise different NFCs.

In the aforementioned cases, extraction of impedance across the two port of the NFC is the key requirement. The circuit analysis has been performed in the next section for analytical estimation of impedance across the device.

3.1 Significance of admittance parameters

A two-port non-Foster impedance circuit requires Y - parameters to estimate the negative impedance across its terminals. These terminals are connected in series to the network to include the non-Foster behaviour. As shown in Fig. 3.1, the floating NFC offers negative impedance Z_{NFC} which is equal to $-Z_L$ in an ideal condition as discussed in the previous section. With the network circuit theory, we get

$$I_1 = -I_2 \tag{3.1}$$

$$V_1 - V_2 = I_1.Z_{NFC} \tag{3.2}$$

These equations together cannot be created as a Z parameter model due to the absence of a direct input-output voltage relationship. The two-port

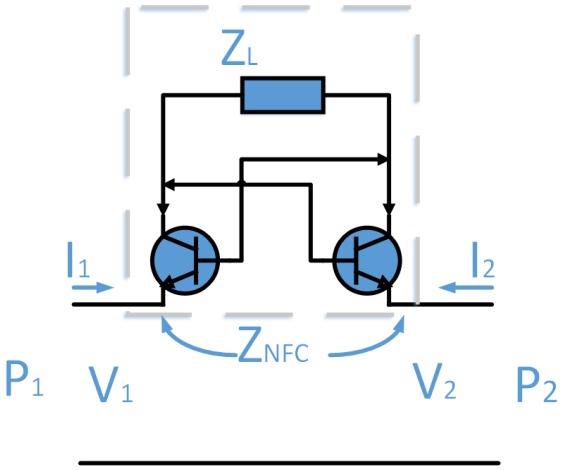

Figure 3.1: A floating two-port series NFC circuit model having equivalent negative impedance Z_{NFC}.

Y-parameters matrix is given as

$$\begin{bmatrix} I_1 \\ I_2 \end{bmatrix} = \begin{bmatrix} \frac{1}{Z_{NFC}} & \frac{-1}{Z_{NFC}} \\ \frac{-1}{Z_{NFC}} & \frac{1}{Z_{NFC}} \end{bmatrix} \begin{bmatrix} V_1 \\ V_2 \end{bmatrix} \tag{3.3}$$

Since, the representation of Z parameter matrix is not possible for a two-port floating NFC, the Y_{21} parameter is required to estimate total impedance across the terminal, which is given as

$$Z_{NFC} = \frac{-1}{Y_{21}} \tag{3.4}$$

The above analysis clearly shows that the estimation of Z_{NFC} in a floating two port non-Foster series element (balanced) using Z_{21} is not an appropriate way and is always estimated using Y-parameters. In the case of a grounded one-port non-Foster shunt element (unbalanced), either Z parameters or Y parameters or both are equally applicable. This analysis has been instrumental in extracting the negative capacitance which is witnessed

in rest of the chapters, covering the development of two-port non-Foster impedance circuits.

3.2 BJT-based NFC design

An OCS, two port floating NFC has a high impedance across the ports and the emitter terminal of bipolar transistor, which has been connected to input and output ports as shown in 2.9. As verified in Fig. 2.11, the transistor required for the design must have a very high cut-off frequency to achieve linearity at high frequencies. The BJT spice model used here is BFG 405W of NXP Semiconductors [76] having a cut-off frequency around 25 GHz. The theoretical analysis discussed in the section 2.4.2 justifies that the selected transistor can achieve a constant negative impedance up to 2.5 GHz (one-tenth of the transistor cut-off). However, the practical performance achieved would be lower than the theoretical estimation. TDK, Murata and Panasonic libraries have been referred for accurate analysis of the simulation model. The standard design libraries of transistors and circuit components are considered to include parasitic effects in all simulations. The design has been simulated and optimised using Keysight advanced design system (ADS) [77].

As discussed earlier, the NFC circuit has been designed with a common base transistor pair with voltage divider biasing. This biasing holds the base voltage at a fixed value independently as the base current provided to the divider circuit may be large compared to the usual base current. The NFC is designed using an FR-4 substrate with a dielectric constant of 4.4 and a thickness of 0.8 mm. The board size is 20 mm by 40 mm with the microstrip based 50-Ω traces connected to the surface mounted devices i.e.

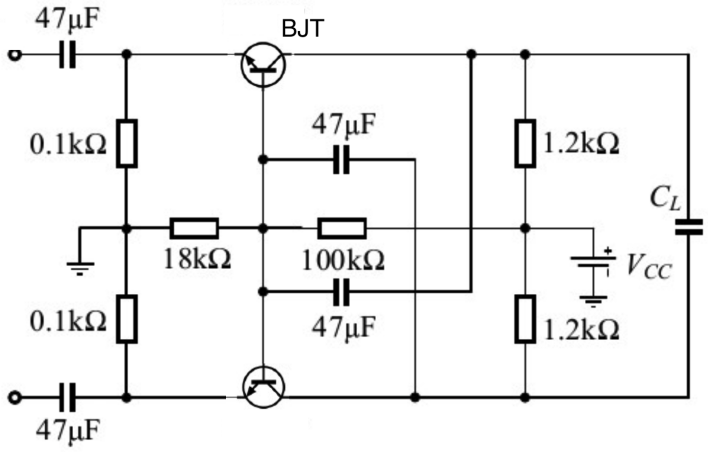

Figure 3.2: A floating BJT-based NFC schematic with essential biasing network and dc blocking capacitors.

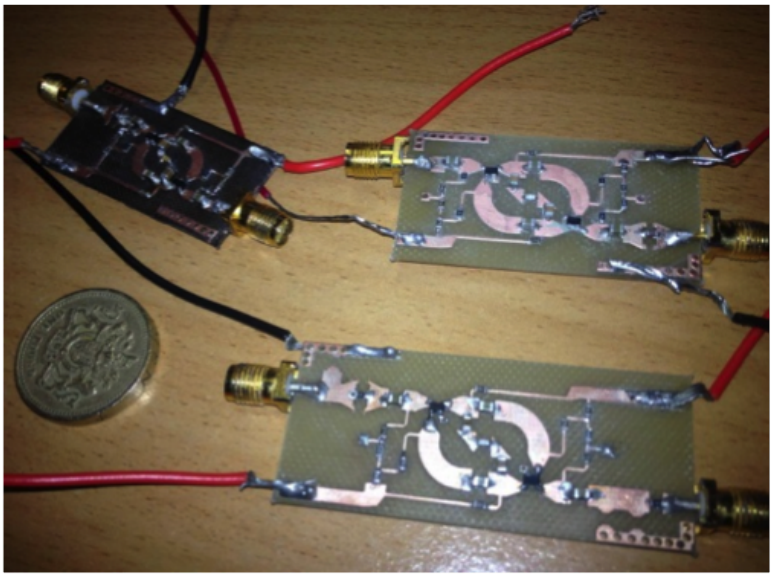

Figure 3.3: The fabricated prototypes of the BJT-based two-port NFC based on circuit diagram shown in 3.2.

transistors, inductors, capacitors and resistors. The RF choke in the dc lines additionally restricts the coupling of RF, as the dc biasing network trace lines are narrow and hence, offer high impedance to the high frequencies. It has been observed that the NFC is showing insertion losses instead of gain. However, the gain can be achieved either by operating the transistor as an amplifier or using the resistive load to induce negative resistance (gain).

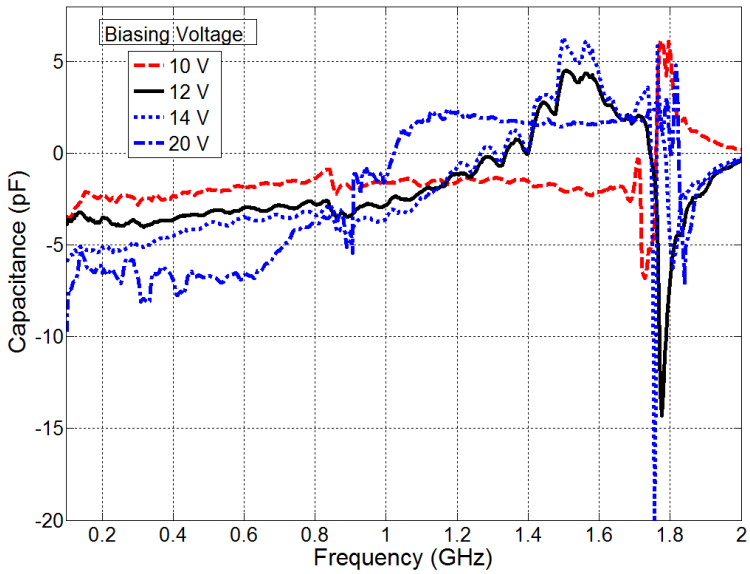

Figure 3.4: Tuning of the NFC with different biasing voltages for the load of 4.7pF.

The circuit diagram is shown in Fig. 3.2 and the corresponding prototype is shown in Fig. 3.3. With a load of 4.7 pF on the NFC, the expected measured negative capacitance can be tuned with a different voltage biasing as shown in Fig. 3.4. A biasing voltage of 14 V is sufficient to develop an almost constant capacitance of -4.7 pF between the two ports of the circuit. There is no dc coupling between these two ports which has been experimentally verified. Hence, the presented NFC is open-circuited stable.

The complete measurement and simulation results of the NFC at 14V biasing are shown in Fig. 3.5. It has been noticed that for a load of 4.7 pF, the negative capacitance till 1.2 GHz has been achieved. The post-processing of the measured data has been done using the Y-parameters as discussed in previous section. Additionally, the circuit has around 4 dB to 5 dB insertion loss and an acceptable return loss. The prototype of this NFC matches well with the simulation model and the theoretical calculations. The capacitive behaviour of the NFC is abruptly changed at high frequency due to the circuit instability. The stability technique discussed in the chapter 2 has been

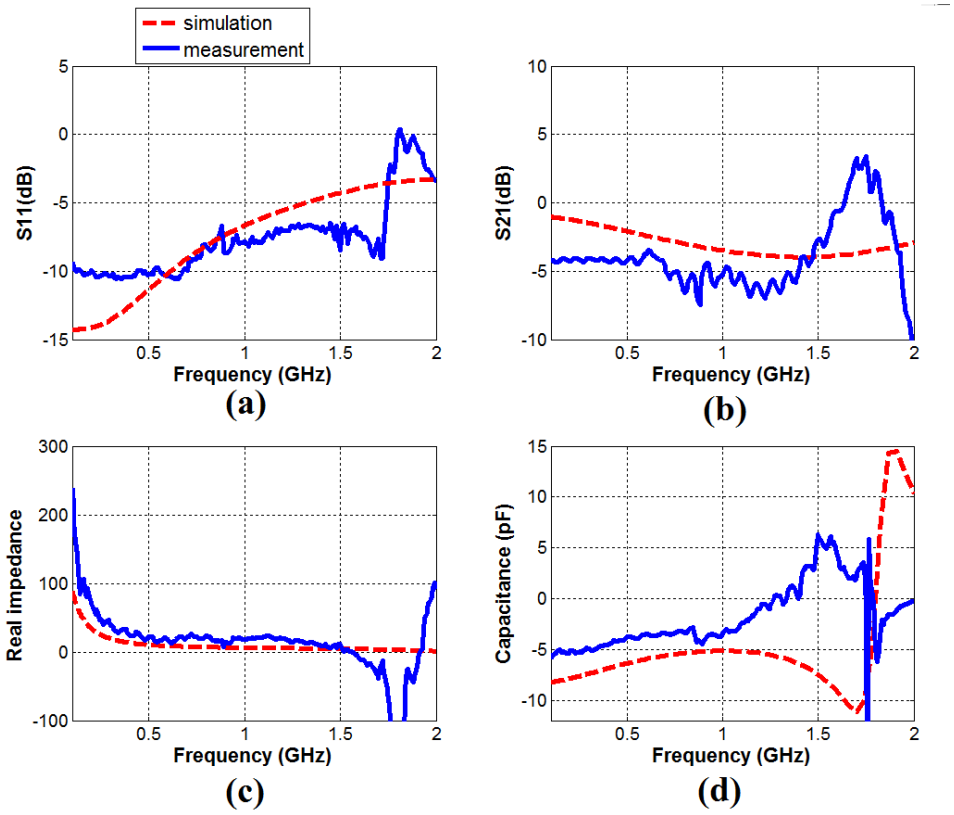

Figure 3.5: Simulation and measurement comparison of BJT based capacitive non-Foster impedance circuit biased at 14 V.

useful to stabilise the practical NFC design. A graphene approach for the realization of non-Foster impedance has been validated in next section using similar circuitry, but replacing the BJTs with GFETs.

3.3 GFET-based NFC design

In the past decade, a two-dimensional graphene material has been the area of interest for many researchers as it has ultrahigh carrier mobility. It is considered to be the gateway for next generation FETs beyond silicon. Due to the gapless band structure, the switching mechanism of GFET is quite poor and unsuitable for logic designs [78]. High carrier mobility (>200,000 $\mathrm{cm}^2/\mathrm{Vs}$) measured in suspended graphene [79, 80] still motivates GFET to

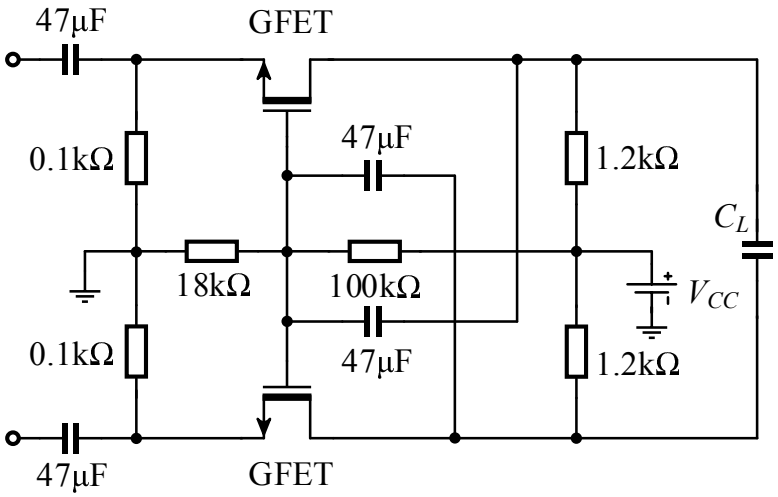

Figure 3.6: Schematic of the GFET-based NFC circuit.

be a potential candidate for analog/RF circuit applications [81]. Also, the GFET based RF system components like amplifiers [82, 83] and mixer [84] have been introduced in recent years.

The non-Foster impedance circuit using Linvill's approach with a GFET instead of BJT has been presented [29] which describes a GFET-based NFC circuit as shown in Fig. 3.6. For the first time, the usage of GFET for an NFC design is discussed and the negative capacitance simulation is presented. The verilog-A model of GFET with estimated parasitics as shown in Fig. 2.15 is used as an active element to achieve negative capacitance at VHF range. The electromagnetic (EM) model of a PCB layout including footprints of real components has also been taken into account while ensuring more realistic results. The simulation exhibits good negative capacitance up to 200 MHz. Excellent NFC tuning has been achieved by varying the load capacitance and supply voltage. The stability check based on Nyquist stability criterion has been performed up to 2 GHz to ensure the NFC design to be devoid of any oscillations.

More realistic results are obtained by the EM model of a printed circuit

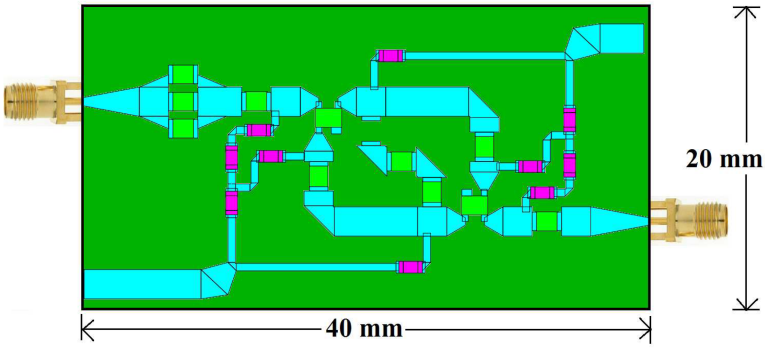

Figure 3.7: Layout including footprint of real components (except the GFET footprint).

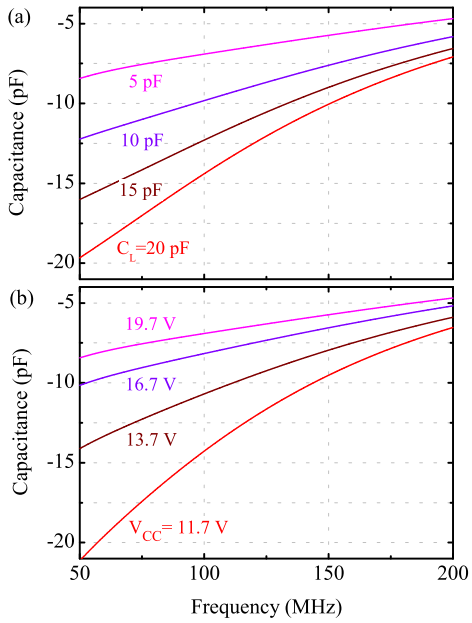

Figure 3.8: Simulated capacitance of the proposed NFC: (a) Load tuning (b) Voltage tuning.

board (PCB) layout (see Fig. 3.7) and then, by EM circuit co-simulation. The NFC prototype is built on a two port PCB with 0.8 mm FR-4 substrate. Transistors and surface mount RLC devices (package size 0805 and 0402) are connected with the 50 Ω microstrip transmission lines (not for dc bias wires). The footprints of all real components excluding that of GFETs have been taken into account while designing the layout. Good matching between the simulation results and measurements of the BJT-based NFC have been reported[85], ensuring the validity of the PCB model. The Gerber file of the optimised layout exported for fabrication is followed by the component placement. Fig. 3.8(a) shows the achieved negative capacitance against frequencies at different load capacitances. It can be seen that the negative capacitance is directly proportional to the load capacitance up to 200 MHz. Similar tuning can also be achieved by varying the supply voltage (see Fig. 3.8(b)).

During the design procedure of GFET-based NFC, it has been found that the low output resistance, primarily due to the poor saturation current of GFET, degrades the performance of NFC. By improving the output resistance, the maximum operation frequency can be increased and the variation of negative capacitance against frequency can also be reduced. In this work, the Q-point (quiescent point) is chosen within the measurement window rather than the optimum point to ensure more realistic results. Therefore, picking a better Q-point is one way to increase the output resistance. An alternative approach is to use the bilayer or multilayer GFETs which provides better saturation current.

The presented GFET-based NFC has been stabilised using the Nyquist stability technique as discussed in [29]. In this approach, the stable circuit must not have a clockwise encirclement of (-1+j0) point in the contour

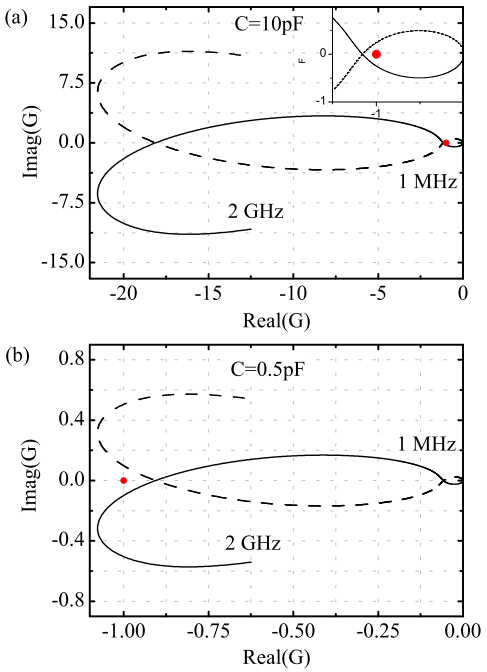

Figure 3.9: Complex plot of G(s) from 1 MHz to 2 GHz: (a) for C = 10 pF (b) for C = 0.5 pF. Dashed lines are the plots of G(s) from -1 MHz to -2 GHz. The inset is a zoomed in view close to (-1+j0) point.

which can be obtained from complex plot with the product of load admittance and source impedance (i.e. $G(s) = Y_l(s) * Z_s(s)$). Fig. 3.9 (a) shows the complex plot of G(s) from 1 MHz to 2 GHz (10 times the maximum operation frequency of the proposed NFC). In Fig. 3.9 (a), it is clearly shown that a series connected capacitor C = 10 pF does not stabilise the proposed NFC because due to the clockwise encirclement of point (-1+j0). However, when a series capacitor C = 0.5 pF is employed (see Fig. 3.9 (b)), the point (-1+j0) is moved out of the net encirclement stabilising the NFC. In the case of broadband applications, a suitable NFC is connected with some passive structures such as an ESA or the unit cell of MTM/meta-surface which act as load matching as well as a stability element. The BJT-based NFC prototype and the presented GFET approach have limitations on size and bandwidth at high frequencies. These constraints are outplayed with a novel RTD-based NFC which has been presented in the next section.

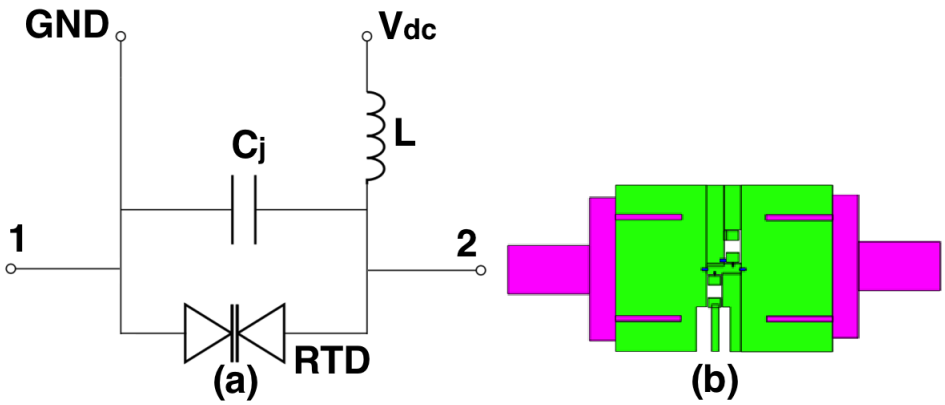

Figure 3.10: (a) The basic circuit diagram of RTD with junction capacitance and biasing circuitry. (b) The evaluation board layout of the RTD with end to end SMA connectors and biasing circuit at bottom layer.

3.4 RTD-based NFC design

NFCs have traditionally been implemented with transistor pairs to achieve negative impedance, but these have limitations on performance and bandwidth at high frequencies. At certain biasing voltages, double barrier RTDs behave as negative differential resistance (NDR) devices, which may be transformed to exhibit negative impedance. In contrast to the BJT-based NFC, these structures serve to gyrate the load impedance, such that an inductive load will lead to a negative capacitance and vice versa. The negative impedance behaviour for prototypes have been demonstrated to safely measure a sample with negative resistance at up to 3 GHz and a device gain of around 5 dB from dc to 4 GHz. Stability analysis of the RTD is discussed and verified using the Nyquist stability criterion. Stabilised negative capacitance NFCs show optimum performance from dc to a few GHz depending on the load value. Additionally, it is envisaged that, the RTDs can operate at frequency ranges up to THz, such that, this topology is extended to higher frequency operation subject to certain fabrication constraints.

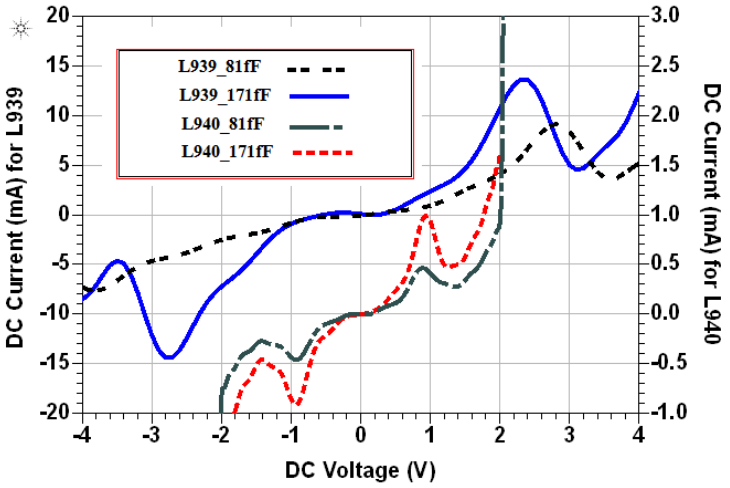

Figure 3.11: Measured I-V characteristics of the four RTD samples. Negative differential resistance regions are present at $\sim \pm 3$ V for the L939 samples, and at $\sim \pm 1$ V for the L940 samples. The best sample L939 with 171 fF capacitance has been used with biasing at 2.75 V.

3.4.1 Modelling and fabrication

An RTD is a resonant model diode, which is so called due to the transmission of electrons and therefore, the current depends on the alignment between the filled electron states in the emitter with the resonant quasi-confined allowed states in the well. This results in a negative differential resistance and negative slope in the current versus voltage characteristic when the structure is biased just beyond the resonance. This region of biasing where the RTD operates as a negative resistance device is used for the NFC design proposed in this thesis and will be utilised as the basic entity to realise floating and grounded negative reactances.

RTDs exhibit voltage-controlled behaviour where a single-valued current is obtained at different values of voltages. The high-frequency operational limit of an RTD is defined by the charging time constant of the device's capacitance. Hence, low capacitances equate to high-speed devices. Consideration of junction capacitance, negative resistance, parasitic resistance

and load coupling is necessary to model RTDs accurately at microwave frequencies [38, 86].

These RTD samples are fabricated using the GaAs technology. The basic circuit diagram and the layout of the evaluation board is shown in Fig. 3.10. Four prototypes of the RTDs are used in the study: the barrier thickness were 1.7 nm AlAs (L939) and 5 nm, $\mathrm{Al}_{(0.4)}\mathrm{Ga}_{(0.6)}\mathrm{As}(\mathrm{L940})$, with similar 5 nm well thickness. Two different top contact lengths resulted the in formation of 81 fF and 171 fF junction capacitances respectively with the devices being mounted on high frequency lead-less inductive device packages, wire bonded and ready for use as surface-mount devices. The I-V characteristics were measured using a Cascade Microtech wafer probe station and LCR meter. Each set of measured data was modelled to a polynomial function using a curve fitting tool and then exported to a microwave circuit simulator for circuit design and further modelling. Measured data of these samples are plotted in Fig. 3.11, with negative differential resistance (NDR) regions being clearly visible. As discussed earlier, the RTD must be biased at voltage level corresponding to the negative slope. NDR regions with sharp transitions are not preferred for the selection of biasing point, as they lead to high current sensitivity with voltage variation. The L939 sample with 171 fF capacitance emerges to be the most fruitful negative resistance region for our purpose.

All four samples have also undergone RF characterization, with the measured S_{21} plotted in Fig. 3.12. The L939 sample with 171 fF capacitance shows maximum transmission gain of around 5 dB up to 4 GHz. The RF performance of the diode at various biasing levels has been analysed as a two port network. For a selected sample, the impedance parameters have been extracted for different biasing as shown in Fig. 3.13. At 2.75 V biasing,

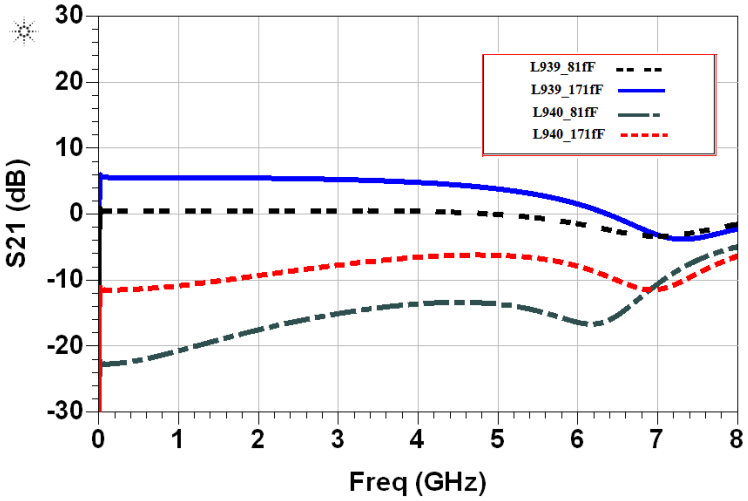

Figure 3.12: Transmission gain of different RTD samples biased at their individual negative resistance region. Sample L939 with 171 fF capacitance exhibits 5 dB gain up to 4 GHz and positive gain at up to around 6 GHz, however this may lead to instability and oscillation of the device.

the resistance measured in the device is around -50 Ω at low frequencies and this parameter increases with frequency. Also, the additional reactance offered by the device is quite small as compare to the resistance attained at lower frequencies and this has an effective contribution beyond 3 GHz, which accords significantly to degrade the expected circuit performance beyond this point. Due to the operation of the diode in the negative resistance mode, there are concerns with possible oscillations and instability.

3.4.2 Device stabilisation

The stabilisation of diode is mandatory in order to achieve the benefits of RTD-based NFCs. The circuit model analysis for the stable operation of RTDs has been investigated using the differential equation method [87]. Later, Frisch came up with a new condition wherein, all poles in a linear equivalent circuit of the diode, as shown in [88], can be shifted to the left half of the complex s-plane for the diode to be potentially stable. As dis-

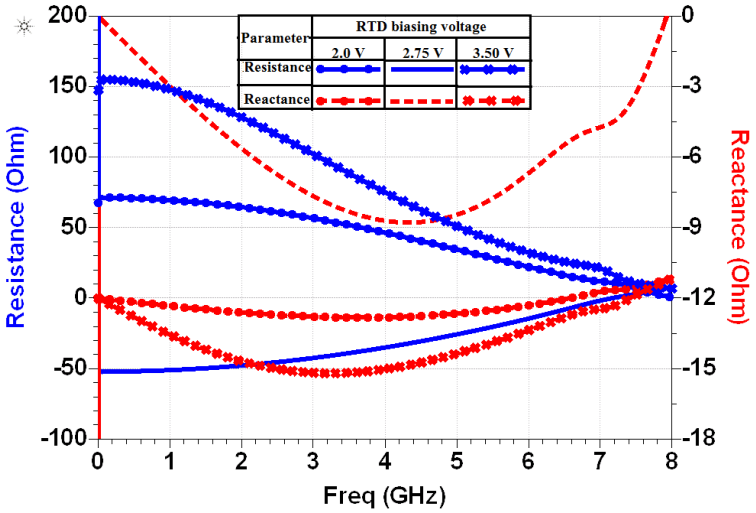

Figure 3.13: RF resistance and reactance shown by the RTD sample L939 with 171 fF capacitance, biased in the different voltages around the negative resistance region. The negative resistance and minimum reactance is noted at 2.75 V.

cussed in chapter 2, the conventional stability techniques are not suitable for the stability analysis of NFCs. Instead, a frequency domain Nyquist criterion is proposed, considering the natural frequencies of the complete circuit. Fig. 3.14 shows that the Nyquist contour no longer encircles the origin point as the series resistor increases from 50 Ω to 55 Ω and hence, selecting the latter will avoid the oscillatory behaviour. The positive resistance mitigates the effect of RTD resistance. When RTD is integrated with a passive load, the passive elements/structures itself behave as a stability component along with the load.

3.4.3 NFCs design methodology

An NFC is a n-port network design that does not obey the Foster's reactance theorem and its reactance or susceptance decreases with the increase in frequency. The one port short-circuited NFC has non-Foster behaviour at the input port. Similarly, the two port floating NFC exhibits this property across

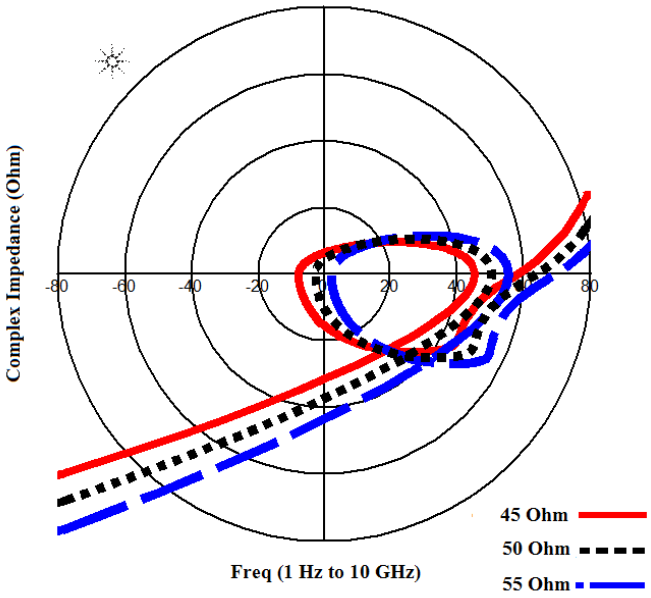

Figure 3.14: Test of RTD stability using the Nyquist stability criterion, for determination of stable component values. Encirclement of the origin in the complex plane implies instability.

the two ports. The transistor-based NFCs have been explored recently for active matching of ESAs [33]. The stable negative resistance RTD element discussed in the previous sections is utilised to develop a bilateral design for negative capacitance and inductance. A unique feature in these non-Foster designs is that all components except the RTD element are passive RLC components. Thus, it highly reduces the complexity of the circuit realisation once a potentially stable RTD is obtained.

Schemes for designing various open-circuited and short-circuited inductive and capacitive NFCs are shown in Fig. 3.15. The two port open-circuit design approach has been proposed here. The one port short-circuited version is inspired by [63]. The resistor elements within the passive network associated with the RTD provides stability to the complete NFC. It has been tested with Nyquist stability criterion which has been already discussed in chapter 2. It is also noted that an inductive load results in a negative ca-

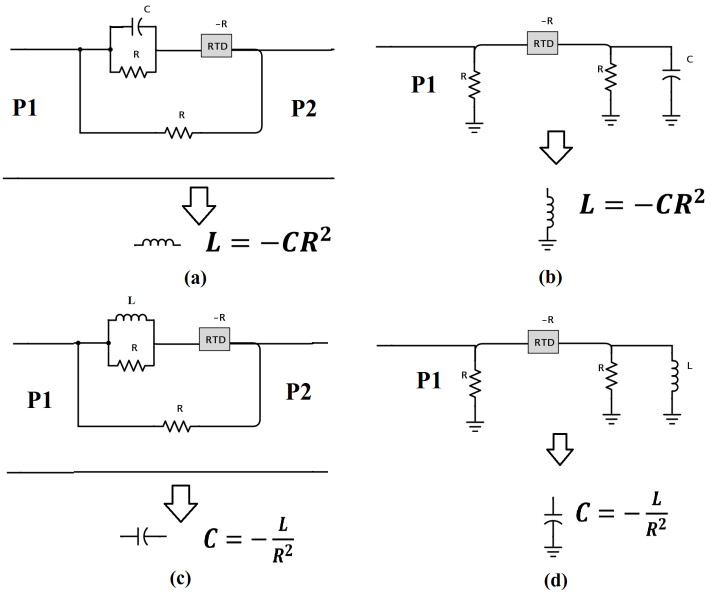

Figure 3.15: Design topologies of various NFCs using RTD elements. (a) A series negative inductor and (b) a shunt negative inductor made of an RTD, resistors and a capacitor. (c) A series negative capacitor and (d) a shunt negative capacitor made of an RTD, resistors and an inductor.

pacitance NFC, while a capacitive load gives a negative inductance NFC. Effectively, this property of inverting the current-voltage characteristics of a network results in a negative gyrator. This particular aspect may find applications at high frequencies, where implementation of negative inductors with inductive loads is troublesome.

Another property discussed here is that ideally, the resistor value is equal to the magnitude of the negative resistance offered by the RTD element. Since, the RTD has a frequency dependent resistance, the negative inductance and capacitance obtained also vary with frequency. Fig. 3.17 shows the realisation of a negative capacitance using an inductive load, in accordance to the circuit from Fig. 3.15(c) or Fig. 3.15(d). The decreased bandwidth of fabricated NFC as compared to the ideal case is evidently witnessed. The RTD may similarly be used to synthesise a negative inductor. Fig. 3.15(a) and Fig. 3.15(c) shows the two port inductive NFC and a capac-

itive NFC, respectively. In inductive NFC, a parallel RC circuit is connected in series with RTD having impedance -R which produces the impedance Z_1 as

$$Z_1 = \frac{R}{1 + j\omega CR} + (-R) = \frac{-j\omega CR^2}{1 + j\omega CR} \tag{3.5}$$

This Z_1 is associated in parallel with R to achieve overall impedance Z_a as

$$Z_a = \frac{\frac{-j\omega CR^2}{1+j\omega CR}R}{\frac{-j\omega CR^2}{1+j\omega CR} + R} = \frac{-j\omega CR^3}{R} = j\omega(-CR^2) = j\omega L_{effective} \tag{3.6}$$

Hence, $L_{effective} = -CR^2$ is the equivalent negative inductance across the two ports of the circuit. Similarly, Fig. 3.15(c) shows the equivalent capacitance $C = -\frac{L}{R^2}$. Fig. 3.15(b) and Fig. 3.15(d) are one port short-circuit negative inductance and capacitance respectively. Fig. 3.16 shows the negative inductance obtained with a capacitive load using the circuit topology as shown in Fig. 3.15(a) or Fig. 3.15(b). These inductive NFCs resonate at a single frequency as the internal inductance of the RTD is very small. Also, in the ideal condition, with the absence of RTD junction, the capacitance leads to a relatively constant inductance with frequency, as compared to the non-ideal case with a non-zero junction capacitance. It shows that the junction capacitance is the primary frequency-limiting feature of the device. As this junction capacitance can be reduced quite comfortably in the fabrication process, the maximum operating frequency of this NFC may be thus, increased substantially. The theoretical expressions in all cases of Fig. 3.15 shows negative impedance in an ideal situation when the circuit resistance is equal to the RTD impedance.

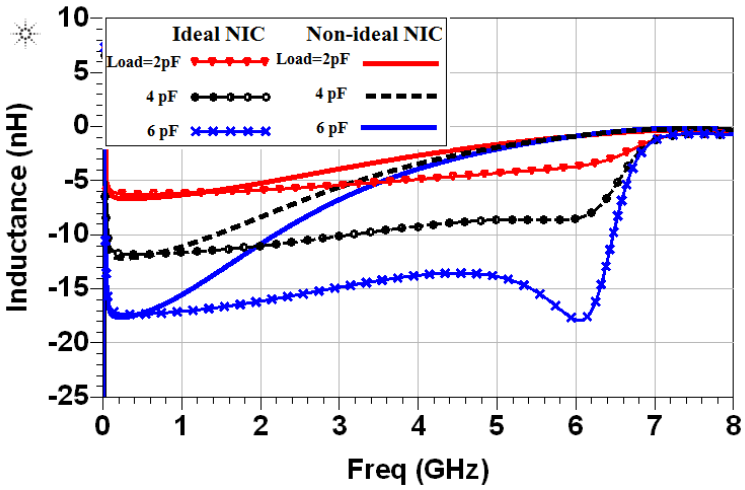

Figure 3.16: Inductive NFC with different load capacitance values.

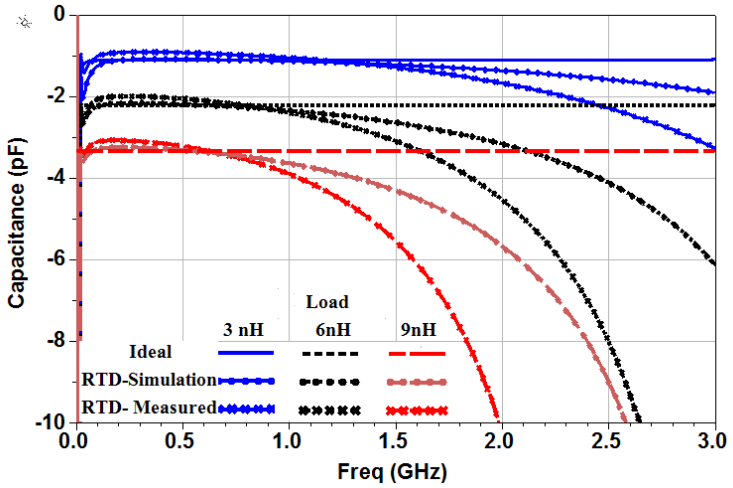

Figure 3.17: Negative capacitor NFC following the circuits from Figs. 3.15(c) or (d). The figure shows the effect of negative capacitance due to variation of load inductance values, and comparisons between using an ideal, simulated and measured RTD model. In either case, negative capacitance may be achieved, but bandwidth is minimum for the measured scenario due to the effective dominance of parasitic reactance.

Table 3.1: Comparison of different design techniques for realisation of non-Foster impedance.

	BJT	Op-Amp	GFET	RTD
Bandwidth	0.1 GHz-1 GHz	<40MHz	50MHz-150MHz	10MHz-2 GHz
Active element per design	2	1	2	1
Parasitic handling	Difficult	Easy	Difficult	Easy
Design flexibility	Good	Limited	Good	Excellent
Design complexity	Complex	Easy	Complex	Easy
Stability issues	High	Low	High	Low
Component availability	Abundant	Abundant	Rare	Rare
Cost	Cheap	Cheapest	Expensive	Expensive
Full design form factor	Big	Small	Big	Very small
Power consumption	High	Low	High	Very low
Periodic structure	Limited useful	Useful	Limited useful	Very useful

3.5 Summary

This chapter presents three techniques and design processes to achieve non-Foster impedance. The BJT-based negative capacitance NFC design is fabricated and tested. The integration of these BJT-based NFCs with the antenna is discussed in the next chapter. For the GFET-based technique, a novel graphene transistor has been validated by replacing the BJT in the existing design. Due to low output resistance, the performance of the graphene NFC is limited to a frequency of 200 MHz. Further, successful fabrication and characterisation of the GFET-based NFC is under progress. To overcome the size and bandwidth constraints, a novel implementation of an NFC is demonstrated using the RTDs. The RTD samples are measured and used as a two-port circuit element for NFC realisation. It has been shown that the device operates as a negative gyrator, exhibits stable negative reactance and resistance (i.e. gain) in the GHz regime and also differs significantly from previously demonstrated transistor-based devices. It is also noted that the bandwidth of these NFCs may be substantially improved by the reduction

of the device's junction capacitance. The different techniques for non-Foster impedance implementation has been further tabulated in Table 3.1.

The BJT-based prototype NFCs developed in this chapter are utilised as active inclusions to the passive antennas. Also, the BJT-based NFC integrated antennas are presented in the next chapter. Later, the possibility to match ESAs over broad bands has been presented using RTD-based NFCs.

Chapter 4

Non-Foster Matching of Electrically Small Antenna

The development of NFC devices, as explained in previous chapters, opens the path to its application in small antennas. The performance limitation of a passive small antenna in terms of its Q has already been discussed in section 2.8. This chapter furthers the evaluation of fundamental limitations of NFC integrated antennas using Chu's antenna model. Later, the integration of a BJT-based NFC element with an antenna is carried out to enhance the overall performance. Also, the comparison of impedance and radiation performance between an unmatched and NFC integrated antenna has been presented. Furthermore, the implementation of the proposed RTD-based NFC has been carried out to achieve the broadband matching of an ESA model. These NFCs are used to match the impedance of an ESA at low frequency, which is in general difficult due to the frequency-dependent radiation resistance.

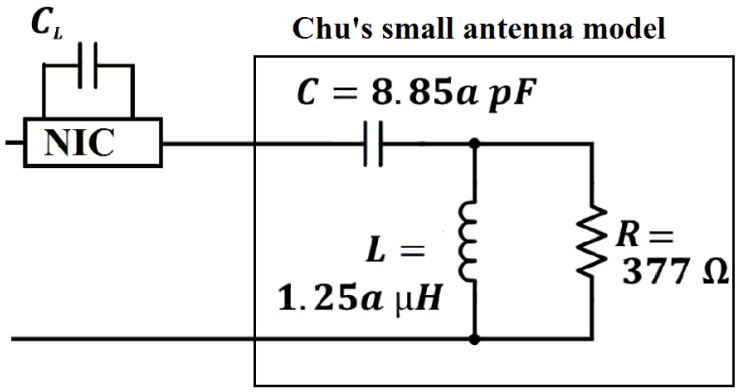

Figure 4.1: Chu's model for a small antenna revised with radiation resistance equalling the free space wave impedance, the capacitance in pF range and inductance in μH range. A non-Foster element introduced to cancel the capacitive reactance of the antenna.

4.1 Minimum Q calculation

This section presents the fundamental limit of Q for an antenna which has been integrated with non-Foster elements. Chu's fundamental Q-limit of small antennas has been revisited for NFC integrated antennas, where non-Foster elements are assumed to be within the Chu's sphere [89]. In other cases, where the NFCs do not belong as a part of the antenna, the fundamental limit for matching a high-Q antenna is defined by Bode-Fano [18], which has been revisited using a non-Foster matching technique. The non-Foster antenna overcomes Chu's fundamental limit or Bode-Fano limit of small antennas depending upon the configuration of its non-Foster elements as a part of antenna or matching network respectively. The simulation and measurements of the tunable capacitive non-Foster impedance circuit has been developed in the previous chapter and the same is employed here for circuit modelling. The Q of an ESA at resonance, is very low in contrast to being very high otherwise, which results in a narrow bandwidth performance. The overall loaded Q, Q_{loaded} of the circuit remains unchanged with

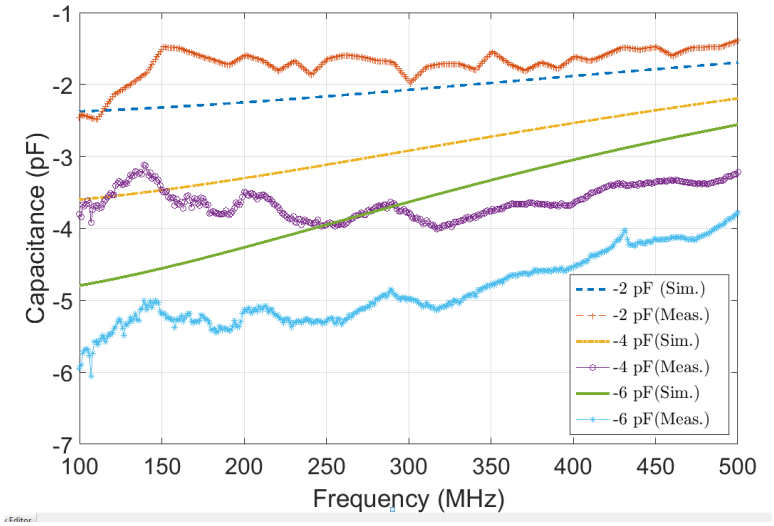

Figure 4.2: The simulated and measured values of capacitive NFCs for different loads in the VHF range.

a lossless matching network for the antenna. However, there is always a finite Q due to the presence of a lossy matching network (Q_m) along with Q of the antenna (Q_{ant}). The overall Q after matching network (Q_{loaded}) is given as

$$\frac{1}{Q_{loaded}} = \frac{1}{Q_{ant}} + \frac{1}{Q_m} \tag{4.1}$$

Chu [7] proposed the RLC-circuit model for the TM_1 mode where, the fields hovering outside the Chu's sphere are linked with antenna's impedance. The circuit resistance R, capacitance C and inductance L are given as

$$R = 1$$

$$C = L = a/c$$

where, a is the radius of Chu's sphere and c is the velocity of light.

For practical conditions, the values are re-calculated during the circuit implementation of this model. Free space wave impedance from the radially propagating electromagnetic field as seen from the surface of Chu's enclosed sphere is then given as

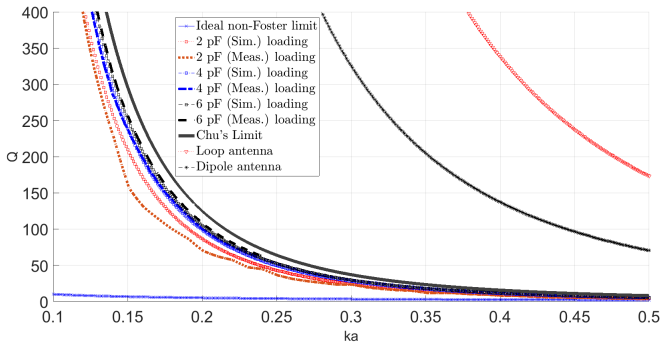

Figure 4.3: The variation of Q with antenna size for passive antennas and non-Foster loaded antennas. The Fundamental limit is satisfied well with the passive antennas but active NFC integrated antenna pushes the minimum Q-bound beyond Chu's limit.

$$R = \sqrt{\frac{\mu_0}{\epsilon_0}} = 120\pi = 377\ \Omega$$

Normalization of the RLC circuit model with free space wave impedance with the updated values of $C = a\epsilon_0$ and $L = a\mu_0$ are shown in Fig. 4.1.

Also, the Q estimation of antenna model for the wavenumber, $k = 2\pi/\lambda$ takes the form

$$Q = \frac{1}{(ka)^3} \tag{4.2}$$

The introduction of non-Foster characteristics in the antenna is expedited by adding negative capacitance or inductance elements to reduce the overall reactance. In Chu's model, it has been noticed that the antenna has a capacitance in the pF range and an inductance in the μH range as shown in Fig. 4.1. An equivalent BJT based negative inductance design in the μH range is a challenging task at VHF frequencies. That being said, a negative inductance in the nH range has been reported recently by Gregoire [40] and Saadat [4]. Additionally, an alternate approach has been proposed by Nagarkoti et al. [5] using RTDs to obtain negative inductance or capacitance of varying ranges. In this thesis, a BJT-based capacitive negative impedance circuit has been designed to achieve negative capacitance; C_{NFC} in the de-

sired frequency band. The capacitive NFC for different loading is shown in Fig. 4.2. A practical NFC integrated antenna a has non-zero net capacitance with a Q of

$$Q = \left| \frac{1}{(ka)^3} + \frac{C/C_{NFC}}{(ka)^3} + \frac{C/C_{NFC}}{(ka)} \right| \tag{4.3}$$

Ideally, the negative capacitance cancel the capacitance exhibited by the antenna i.e. $C = -C_{NFC}$, meaning that the Q of ideal NFC integrated antennas become

$$Q = \frac{1}{(ka)} \tag{4.4}$$

This gives an insight that the Q of an NFC integrated antenna is beyond Chu's estimation for the passive antenna. Fig. 4.3 shows the effects of non-Foster loading on the antenna with simulated and measured non-Foster elements. The ideal condition, at which the non-Foster capacitance fully cancels the antenna capacitance defines a new fundamental limit for a NFC integrated antenna. The Bode-Fano limit [18], which establishes the relationship between the bandwidth and Q for a given reflection coefficient Γ, is given as

$$BW = \frac{\pi}{Q \ln \frac{1}{|\Gamma|}} \tag{4.5}$$

Reduction in the antenna Q further explores the possibility of bandwidth improvement, which is a well-known application of NFC in antennas. Hence, the theoretical Q calculation is a good source of inspiration to integrate a BJT-based NFC with a small antenna under test.

4.2 BJT-based NFC integrated antenna

Printed NFCs have been investigated and developed for few applications, such as the broadband impedance matching of ESAs to exceed the Bode-

Fano bandwidth [18], [19], which talks about the difficulty to match the impedance of ESAs owing to their high Q [7]. Also, they exhibit high reactance and low frequency-dependent radiation resistance. Recently, there has been an interest in the application of NFCs to improve the bandwidth of small antennas [37, 33] and metamaterial structures [90, 91, 92, 93, 94, 95, 96, 97, 98, 52].

An antenna impedance matching topology is presented in this section after the successful development of a BJT-based capacitive NFC in the previous chapter. As discussed before, the non-Foster impedance circuits are intrinsically unstable due to the presence of a positive feedback loop and therefore, it cannot work alone. An additional passive load must be connected with the non-Foster element to shift the location of poles and zeros and hence to overcome the oscillatory behaviour as discussed in Chapter 2. Along with the previously mentioned external passive load, the stability of an NFC also depends on the biasing of active devices, internal load connected, transmission line modelling and the layout design. The stability can be achieved by controlling the positive feedback loop gain by using various methods. In the ideal case, theoretical analysis of stability has been estimated by frequency domain techniques as discussed in the earlier chapters. However, an engineering practice is required to realize a stable practical design. Fig. 4.4 shows the design topology, where stability components are replaced by a passive antenna element, performing non-Foster matching of the antenna as well as taking care of the stability of non-Foster impedance device. The prototype design process is summarised as follows.

1. Design of a Linvill based non-Foster impedance circuit using the circuit layout co-simulation.

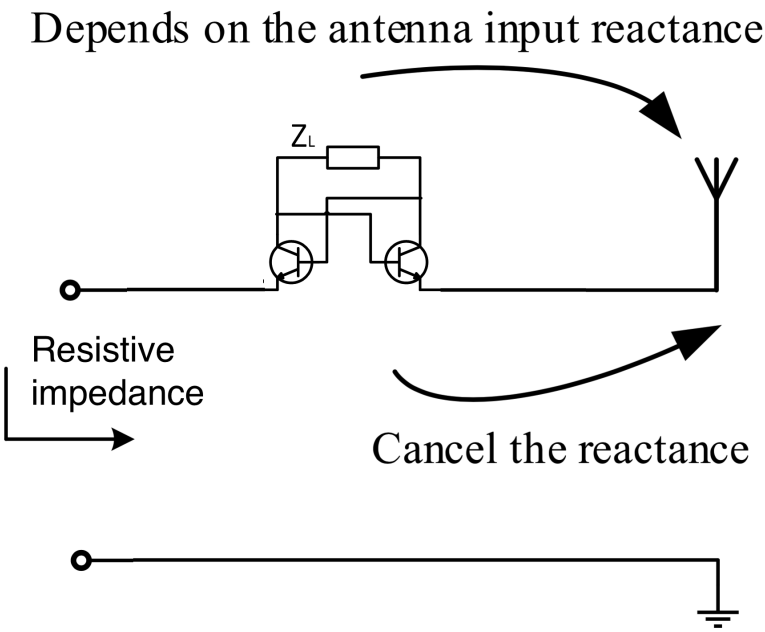

Figure 4.4: Cancellation of high reactance of small antenna using an NFC. Also, same antenna is acting as a stability load for the standalone unstable NFC.

2. Simulation of the input impedance of capacitive electrically small monopole and extraction of the capacitance.

3. Choosing the load capacitor for NFC (Z_L) close to the antenna capacitance.

4. Stability testing of an NFC and the antenna together using transient analysis as well as Nyquist stability criterion.

5. In the case of oscillation, modifying the NFC by changing Z_L and fine tuning of the transistor biasing voltage.

6. After the general theoretical stability calculation; the NFC prototype has been built with additional series antenna circuit model which is equivalent to the input impedance of the real antenna.

7. One of the two ports of the series combination of NFC and circuit

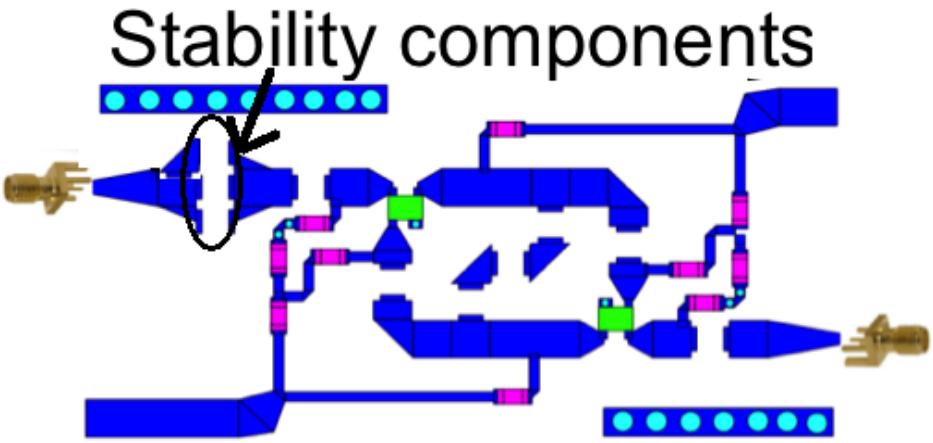

Figure 4.5: Stability components are connected in series with the NFC. These are replaced by 0 Ω resistor when NFC is integrated with the antenna.

model is terminated with 50 Ω and the other is connected to a spectrum analyser. The spikes noticed confirms the unstable design.

8. Changing the biasing voltage and value of the internal load of the non-Foster element Z_L to provide a degree of freedom for smoothing the spikes in the analyser measurements.

9. Once stability has been achieved; the existing circuit model is replaced by the equivalent series antenna.

The NFC design example based on the Linvill balanced floating approach has been fabricated and measured in section 3.2. It is stabilised with the passive stability components connected in series as shown in Fig. 4.5 and later replaced by a short-circuit with the antenna connected in series.

4.2.1 Impedance matching methodology

A monopole antenna with self-resonance at 1.5 GHz has a high reactance at the VHF band and a low radiation resistance, which is directly proportional

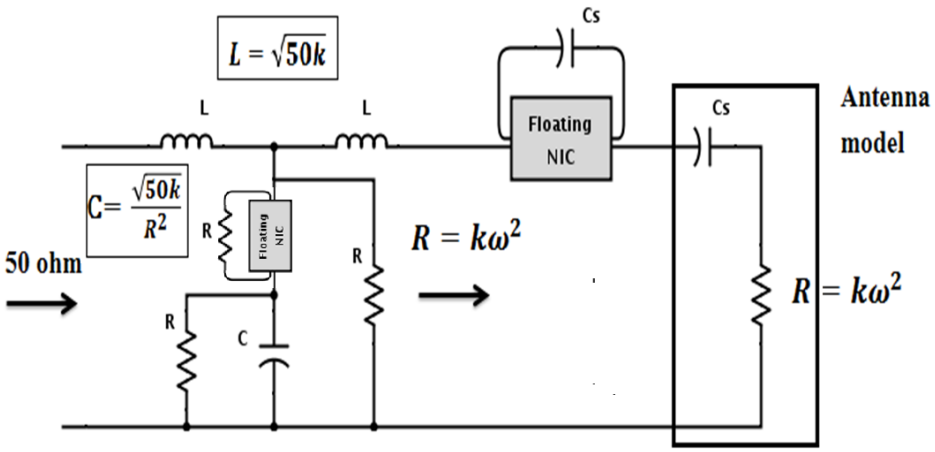

Figure 4.6: The basic non-Foster matching topology for impedance matching of an antenna model to 50 Ω [5]. This approach is ideal one and offers broadband matching. In this work, only one NFC integrated antenna has been built, tested and implemented.

to the square of the frequency. The basic topology for matching the antenna is shown in Fig. 4.6. The antenna can be modelled as a capacitor and a frequency dependent resistance which is valid up to the first resonance.

The series NFC cancels out the antenna reactance. As the resistance at VHF is very small and an ideal N: 1 transformer reflects the load impedance multiplied by N^2 across the decade bandwidth thus, preserving its quality factor [99]. But, the transformer approach is not suitable in ESAs due to its frequency square dependent radiation resistance. Hence, the frequency dependent real impedance can be nullified using a non-Foster inductive transformer presented in [33] or similar transformer circuit by including an NFC as shown in Fig. 4.6. Additionally, internal parasitics produce negative inductance and resistance in a capacitive NFC which, if suitably tuned can improve the matching of the real part to a certain extent. The real impedance

after the cancellation of the reactance is given as

$$Z_{real} = k\omega^2 \tag{4.6}$$

The series inductance L with Z_{real} and in parallel with R results in

$$Z_1 = \frac{(j\omega L + k\omega^2)R}{R + k\omega^2 + j\omega L} \tag{4.7}$$

The capacitor C and R are connected in parallel and are in series with $-R$ as obtained from an NFC approach, and in parallel with Z_1 which results

$$Z_2 = \frac{-j\omega CR^2}{1 + j\omega CR} || Z_1 \tag{4.8}$$

$$Z_2 = \frac{-j\omega CR^2}{1 + j\omega CR} || \frac{(j\omega L + k\omega^2)R}{R + k\omega^2 + j\omega L} \tag{4.9}$$

$$Z_2 = \frac{(-j\omega CR^3)(j\omega L + k\omega^2)}{-j\omega CR^3 - jk\omega^3 CR^2 + \omega^2 CR^2 L + j\omega LR + k\omega^2 R - \omega^2 CR^2 L + jk\omega^3 CR^2} \tag{4.10}$$

$$Z_2 = \frac{(-j\omega CR^3)(j\omega L + k\omega^2)}{-j\omega CR^3 + j\omega LR + k\omega^2 R} \tag{4.11}$$

The series inductor L with Z_2 gives the overall input impedance as

$$Z_{in} = Z_2 || j\omega L \tag{4.12}$$

$$Z_{in} = \frac{-jk\omega^3 CR^3 - \omega^2 L^2 R + jk\omega^3 LR}{-j\omega CR^3 + j\omega LR + k\omega^2 R} \tag{4.13}$$

By substituting $C = \frac{\sqrt{50k}}{R^2}$ and $L = \sqrt{50k}$, the factor k can be estimated by the curve that suitably fits the plot of real antenna impedance. The input impedance thus, becomes

$$Z_{in} = \frac{-jk\omega^3\sqrt{50k}R + \omega^2(50k)R + jk\omega^3\sqrt{50k}R}{-j\omega\sqrt{50k}R + j\omega\sqrt{50k}R + k\omega^2R} \tag{4.14}$$

Further simplification gives

$$Z_{in} = \frac{\omega^2(50k)R}{k\omega^2R} = 50 \tag{4.15}$$

Therefore, ideally, any ESA can be matched to 50 Ω independent of the frequency, using the non-Foster impedance circuits. In a practical sense, the matching is broadband due to the limited performance of the non-Foster impedance circuits. Also, a pair of NFCs can achieve better performance than a single NFC, which can cancel only the reactive part of the antenna. In this thesis, a single NFC behaving as a capacitance cancellation element with added series resistance increases the real impedance of the antenna and thus, improves the match. The losses introduced by the matching network can be eliminated by perfectly matching the reactance which facilitates the broadband matching by using minimum active non-Foster inclusion in the matching network. The additional losses incurred due to the active inclusion may affect the gain performance of the antenna. A condition for gain improvement as the NFC integrated to the antenna, has been discussed in the next section.

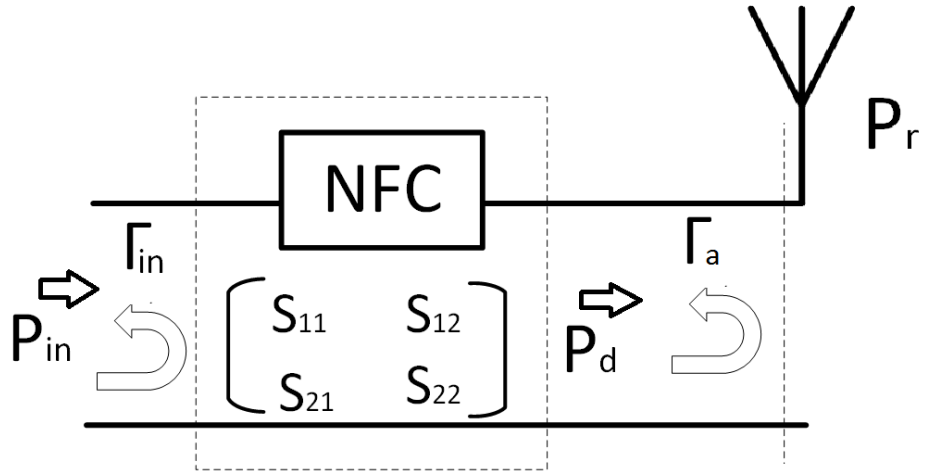

Figure 4.7: Antenna and a matching network with known S parameters to calculate the variation in realised gain.

4.2.2 Antenna gain with non-Foster matching

An NFC integration to the antenna may introduce resistive losses which may affect its efficiency. The efficiency of any antenna is the function of losses introduced and given by the ratio of its realised gain $G(\theta, \phi)$ and directivity $D(\theta, \phi)$. The power at the input of the antenna feeding the network and the power delivered to radiating element is not equal. Mismatch losses are the additional losses except for the antenna efficiency which can be significantly reduced by using non-Foster matching. In the case of an unmatched antenna, there is no matching network and hence, the mismatch, M_p at the input of the antenna can be given as

$$M_p = (1 - |\Gamma_a|^2) \tag{4.16}$$

A matching network added between the input and the antenna is shown in Fig. 4.7. The mismatch loss M_a has been calculated with the known

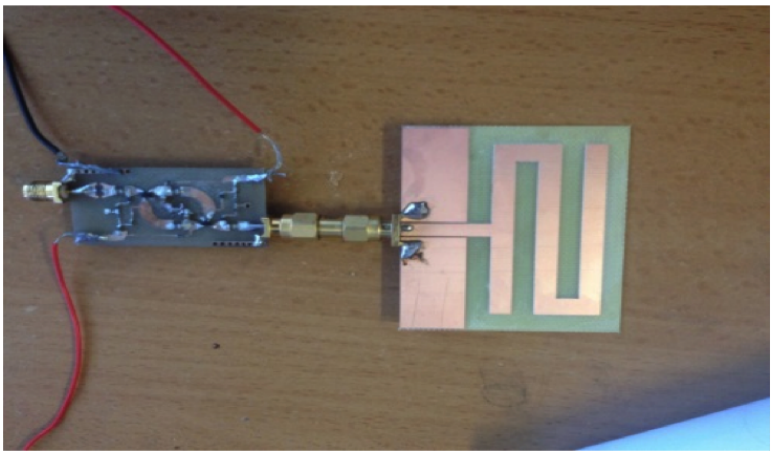

Figure 4.8: The two-port capacitive NFC matching network connected with the planer monopole via SMA connector.

two-port S-parameters of the matching network, given as

$$M_a = \frac{|S_{21}|^2}{|1 - S_{22}\Gamma_a|^2}(1 - |\Gamma_a|^2) \tag{4.17}$$

The radiation efficiency and directivity of the antenna element remains unchanged under any circumstances. Thus, the scope gain improvement is dependent on the ratio of mismatch losses with and without matching network.

$$G_{improvement} = \frac{|S_{21}|^2}{|1 - S_{22}\Gamma_a|^2} \tag{4.18}$$

The $|S_{21}|$ of non-Foster impedance matching circuit can be maximised and $|S_{22}|$ can be minimised. There is a scope of improvement in the realised gain of the NFC integrated antenna. In order to achieve the gain improvement condition, a selection of suitable small antenna under test (AUT) is required.

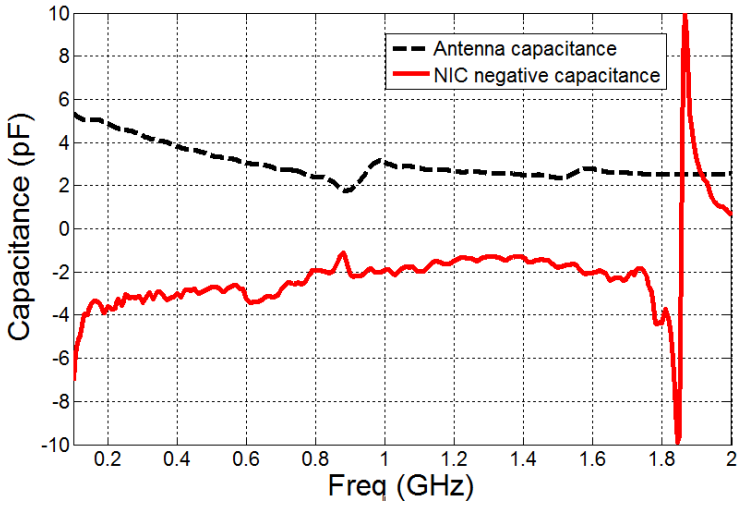

Figure 4.9: Antenna capacitance and negative capacitance obtain from a NFC. The NFC impedance is tuned with biasing voltage and load capacitance to mitigate the antenna capacitance.

4.2.3 Antenna design and geometry

A capacitive antenna geometry is suitable to integrate with capacitive NFC, which minimises the input reactance of the overall antenna system. The planar patch antenna, which is capacitive allows a negative capacitance and non-Foster element to cancel out the capacitance. The initial design analysis and geometrical layout of the proposed antenna was performed in Keysight ADS simulation software [77] as shown in Fig. 4.10. Fig. 4.11 shows the prototype of the proposed patch antenna and the inclusion of active NFC. The designed patch antenna comprises of a partial ground plane radiating structure in top side of the substrate. The low-cost dielectric FR-4 material is used as an antenna substrate with a relative permittivity of 4.4, loss tangent of 0.02 and substrate thickness of 1.6 mm. The feed-line, radiating patch and top layer ground plane are made of 35 μm thick copper layer. The SMA connector is utilized at the end of the microstrip feed-line and top layer ground plane. As the radiating patch end is terminated as open-circuit, the antenna input reactance is capacitive. Though, the shape of radiating patch

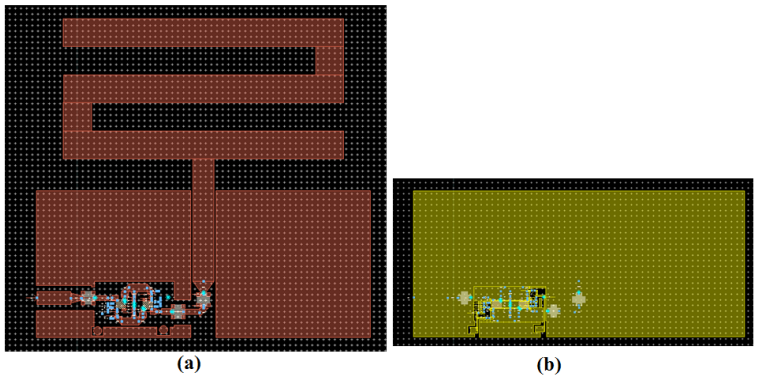

Figure 4.10: Antenna layout in ADS (a) Top layer for RF propagation (b) Bottom layer for dc biasing network. Both layers are sharing same ground plane and are connected through vias.

has been meandered for size reduction, these antennas have low radiation efficiency. The radiation resistance is reduced with the size of antenna as the ratio of ohmic losses of the antenna radiating element to the radiated power is increased.

A non-Foster impedance circuit is designed as a two-port network which is connected end to end with the monopole patch antenna via an SMA connector as shown in Fig. 4.8. The capacitance of the antenna has been extrapolated from the input reactance and with the known value of antenna reactance, the NFC negative capacitance has been determined as shown in Fig. 4.9. Furthermore, an NFC is integrated into the antenna with a form factor i.e. 60 mm by 50 mm, with a double layer topology. The electrical size of this antenna is $\lambda/10$ till 500 MHz and considered as an ESA. The dc biasing circuit has been kept on the lower side and the RF circuit on the top layer is connected through a plated conducting medium as shown in Fig. 4.11. The impedance and radiation measurements of antenna has been performed and discussed in next subsections.

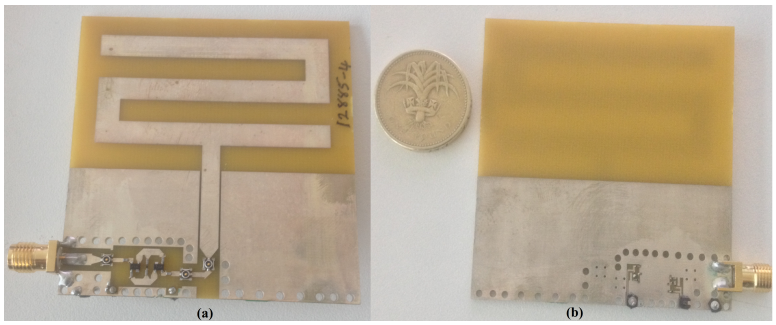

Figure 4.11: Non-Foster integrated antenna prototype with dc biasing network at the bottom layer. (a) Top layer (b) Bottom layer

4.2.4 Impedance measurements

The Murata coaxial connectors are installed in the circuit to perform experiments with minimum affect on the measurement . A passive antenna without NFC, an NFC integrated antenna and a standlone NFC can be measured by suitable tap of external SMA to Hirose adapters on Murata connectors. The default status of Murata coaxial connector switches is short-circuited and has a Hirose UFL connection at the top [100]. The inclusion of an external SMA to Hirose UFL adapters disconnects the default circuit and all the power is directed into/from the external SMA [101]. There are three Murata connectors in each NFC integrated antenna; two of them installed at the input and the output of the non-Foster matching network in RF-in and RF-out mode respectively; and the third connector is placed at the input of the antenna in RF-in mode. In Fig. 4.12, the RF layer of the two-port floating capacitive NFC portion constituting the part of NFC integrated antenna is connected to a VNA via the Murata switch connectors.

The preliminary test for antenna matching has been performed by comparing the impedance matching in the unmatched and non-Foster matched conditions. The return loss S_{11} parameters of the antenna with and without a non-Foster matching network can be easily measured if both the ports

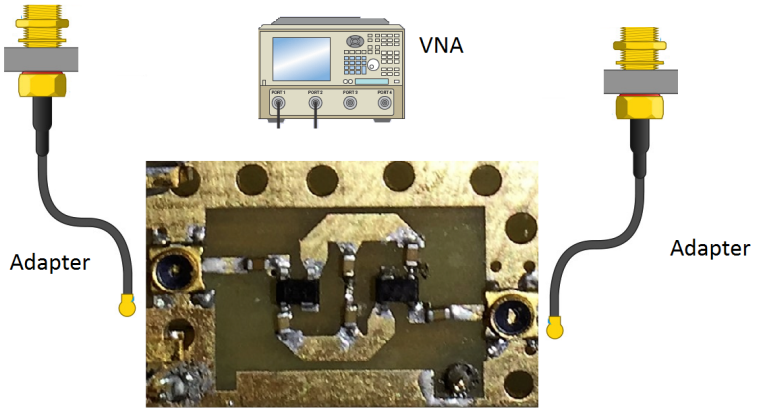

Figure 4.12: Murata switch connectors to tap in/out RF with Hirose UFL to SMA adapters for RF characterisation.

of NFC and the antenna port is terminated with 50 Ω. In compact non-Foster integrated antennas, the SMA to Hirose UFL adapters RF-in cables measures the antenna impedance with and without a non-Foster matching network by replacing the adapter location without disturbing the setup. Fig. 4.13 shows the return loss measurements with different dc biasing voltage and bandwidth improvement has been noticed at 11 V. Fig. 4.14 is a VSWR comparison between the tune matched antenna and unmatched passive antenna. However, impedance matching bandwidth assures that the bandwidth power is included in the circuit. Also, the power radiated may be different depending upon the circuit losses and the matching capabilities between the NFC output and antenna input. Hence, radiative measurement comparison between unmatched and non-Foster matched antenna have been carried out in next section to measure the effective radiation bandwidth.

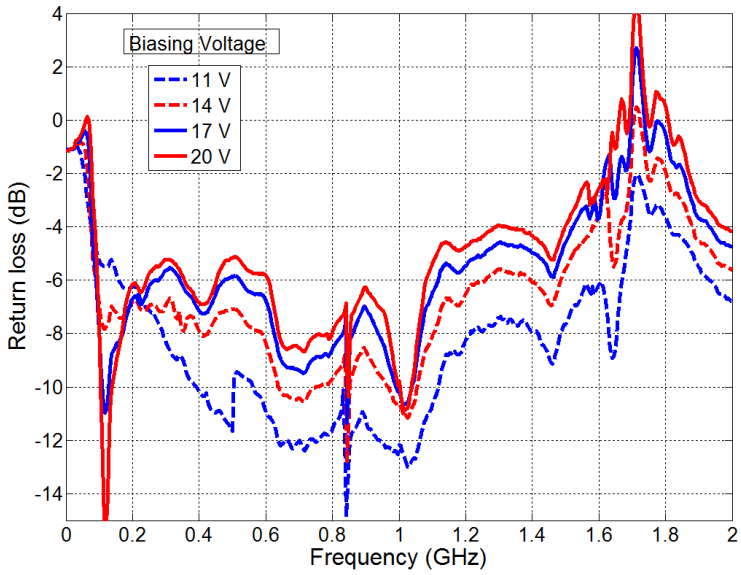

Figure 4.13: Return loss measurement with different biasing of transistors involved in non-Foster matching circuit.

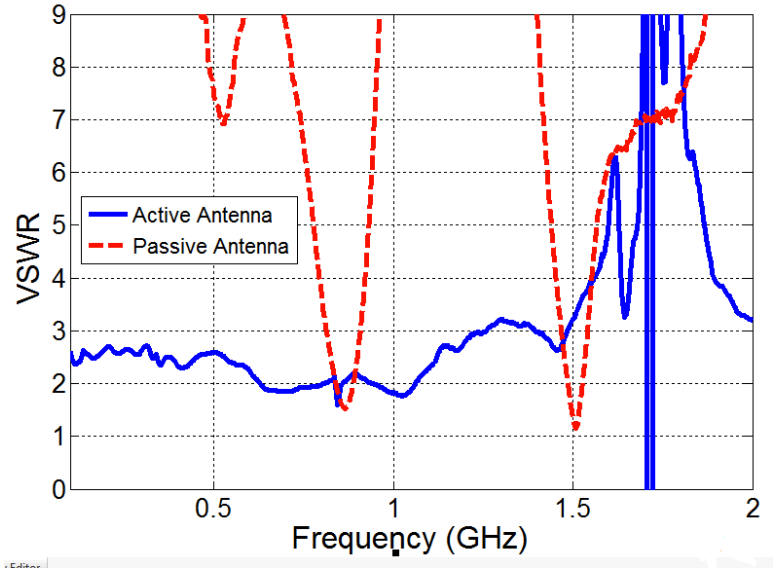

Figure 4.14: Comparison of VSWR measurements with and without non-Foster matching by tap in RF input at relevant Murata switch points.

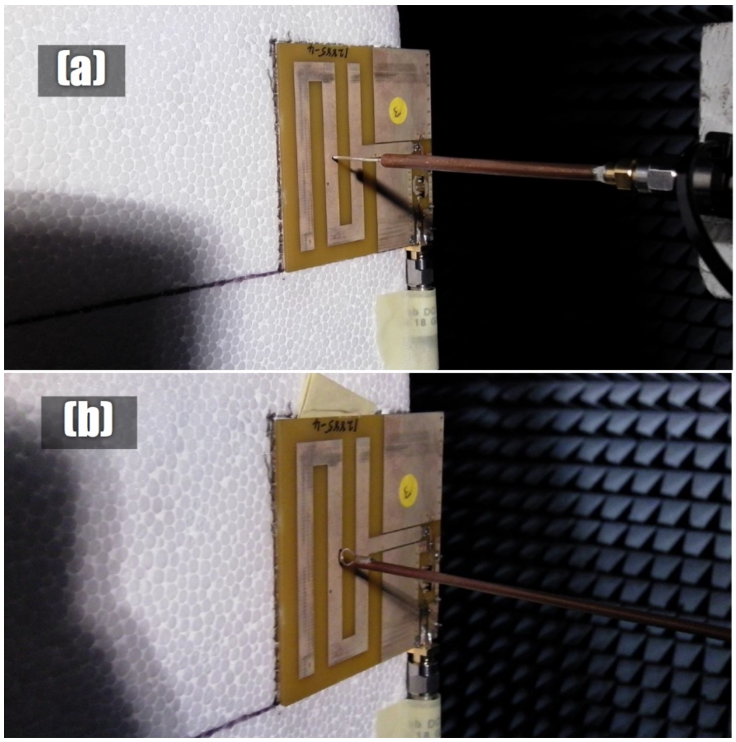

Figure 4.15: (a) Monopole probe for E_z component of near-field measurements. (b) Loop probe for H_x component of near-field measurements.

4.2.5 Radiation measurements

The improvement of impedance bandwidth is necessary to minimise the reflection losses and maximise the power transferred to the circuit. To ensure reasonable conducted power is radiated, a radiation bandwidth measurement is required. The radiation bandwidth may be less than the impedance bandwidth depending upon the internal losses of the non-Foster matching circuit. Radiation bandwidth improvement is the actual value which verifies the NFC enhancement of radiation efficiency for small antennas.

The radiative measurements are classified as far-field range and near-field range. The far-field setup is preferred for lower frequency antenna measurements, where simple pattern cut measurements are required. On the other hand, near-field setups are useful for higher frequency measurements, where complete pattern and polarisation information is needed.

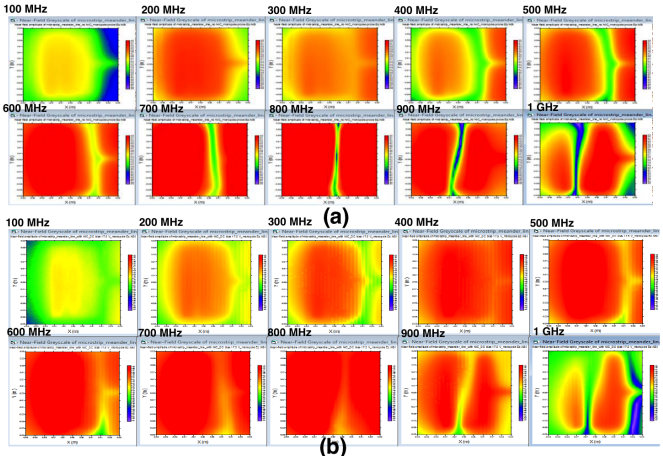

Figure 4.16: The amplitude of near-field E_z component measurements from 100 MHz to 1 GHz in (a) passive and (b) active matching antenna shown in Fig. 4.15 (a).

Far-field measurements are further classified as outdoor range, anechoic chamber and compact range. Similarly, near-field measurements are also sub-categorised as planar, cylindrical and spherical. Far-field measurement using an anechoic chamber and near-field measurements using planar technique have been performed in this work. Both these measurements are indoor, eliminating the issues concerning weather and electromagnetic interference. Also, an anechoic chamber based far-field setup has limitations in HF and lower VHF range because of the chamber size constrains. So, in such cases, near-field measurements are more reliable for under 500 MHz operating frequencies.

The near-field measurement technique works on the principle of scattering matrix theory developed by Kerns [102]. The planar near field measurement of an antenna has been carried out using a monopole probe placed normally to the near field region to measure E_z component and a loop probe to measure H_x component as shown in Fig. 4.15. This technique however, does not require an ideal probe, as it measures one field component at a point. Another benefit is that it is not important to have an ideal polari-

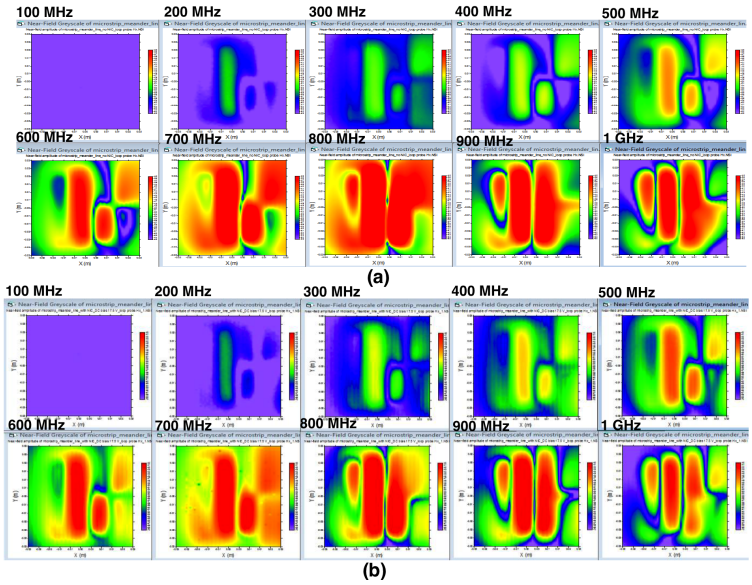

Figure 4.17: The phase of near-field H_x component measurements from 100 MHz to 1 GHz in (a) passive and (b) active matching antenna shown in Fig. 4.15(b).

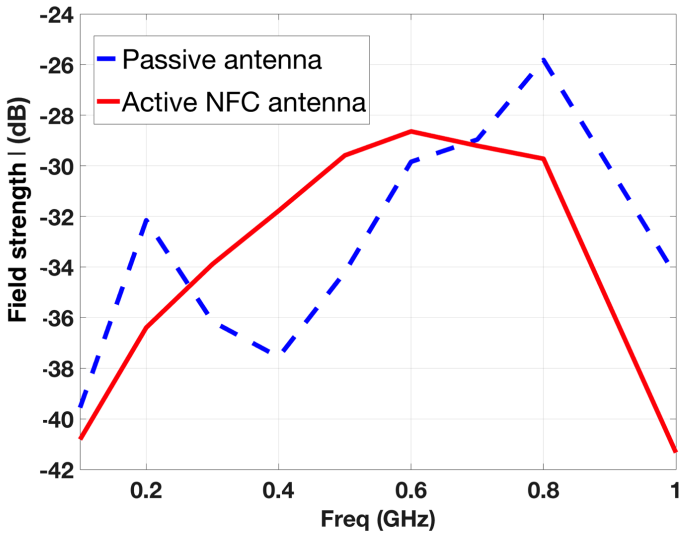

Figure 4.18: The comparison of field strength in passive and NFC antenna at the scan centre.

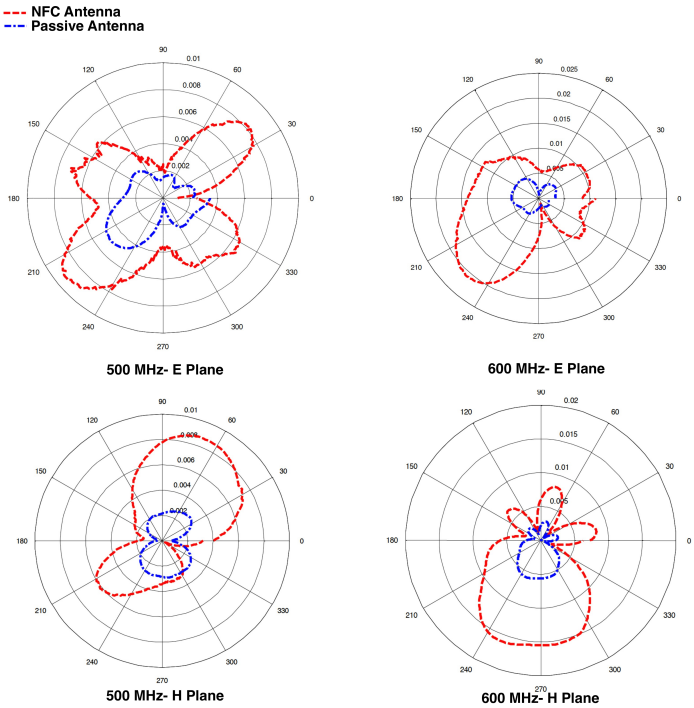

Figure 4.19: The comparison of far-field at 500 MHz and 600 MHz on passive and NFC antenna. Linear scale is used for visualisation of the effective variation.

sation of the active antenna under measurement. The multiple reflections are needed to be neglected and the measurements have to be made over a finite plane. The near-field measurements are very useful for far-field calculations using the Fourier transform of near field data. This extraction is accurately valid for directive antennas like horns, where the strong field component is normal to the finite measurement plane. The probe correction is required during the post-processing of data that basically involves two parts. First, the pattern correction, which is due to the probe's main component pattern. Second, the polarisation correction due to the probe's cross component pattern. The passive meander line antenna designed here shows poor directivity normal to the surface. However, it is useful to have the comparative study of the near-field measurement with or without an NFC.

The near-field measurement comparison for the amplitude of E_z component is shown in Fig. 4.16 and H_x component is shown in Fig. 4.17. The significant improvement in field strength, specifically for H_x has been achieved from 300 MHz to 600 MHz when the NFC is biased at 17.5 V, in both the cases. This observation is further verified by comparing the field strength at the scan centre with or without NFC. There a slight improvement in NFC integrated antenna from 300 MHz to 600 MHz bandwidth as shown in Fig. 4.18. The radiation bandwidth with the NFC is an effective bandwidth for gain enhancement but is less than the impedance match bandwidth. Thus, the gain improvement of few dBs has been recorded within radiation bandwidth.

The far-field measurements have been performed in an anechoic chamber for 500 MHz and 600 MHz frequencies in order to verify the similar improvements as in the case of near field measurements. The E-plane and H-plane pattern are compared for both discrete frequencies. As the gain improvement is limited, linear scale has been used in the polar plots. Due to the design complexity involved in BJT-based NFC antenna, the effective improvement in radiation bandwidth is limited. The next section deals with an alternate approach to achieve broadband matching using RTD-based NFC designs.

4.3 RTD-based NFC integrated antenna

Due to the large reactive input impedance and very low radiation resistance of an ESA, only a small amount of power is radiated to the far-field region and most of the input power is reflected or stored in the reactive near-field region. The quality factor Q may be reduced towards Chu's limit [7], thus

increasing the bandwidth through various schemes, such as, the use of multiple matching stages. However, there exists a fundamental gain-bandwidth restriction between the generator and the load, resulting in the achievement of only a finite bandwidth, even with a large number of matching sections. Furthermore, the circuit size and complexity will increase and resulting in the degradation of efficiency as the losses cumulate.

It is possible to overcome the gain-bandwidth limitations with a non-Foster approach using NFCs. The radiation resistance of an ESA has a frequency-squared dependence which is small at low frequencies (a few Ω). The reactive and resistive matching of the ESA has been performed with the RTD-based NFCs and the same is shown in Fig. 4.20. Two RTD NFC stages are required for matching: one each for the resistive and the reactive matching. An RTD-based capacitive NFC (nearest to the ESA) first cancels the positive antenna capacitance, leaving an approximate value of real impedance. The next stage is a resistive matching network that transforms the frequency dependent antenna resistance $R_a = k\omega^2$ to 50 Ω (or some other constant characteristic line impedance).

The antenna model resonates (unmatched) at 2.5 GHz, with a 10 dB bandwidth from 2 GHz to 3.5 GHz. At low frequencies, the antenna may be modelled as a capacitor with, $C = 5$ pF and a resistor with parameter, $k = 2{*}10^{-19}\ \Omega{\cdot}s^2$. The proposed topology in 4.20 is not built and tested but, the measured S-parameters of the RTDs are employed for circuit analysis. Using the measured RTD parameters, the antenna is matched through simulation for two cases employing the parameters from Table 4.1 in the circuit from Fig. 4.20. The improvement in impedance matching and bandwidth is evident from Fig. 4.21: ANT I is matched such that the lower frequency of the matched band has been reduced to 1 GHz; ANT II is matched to encom-

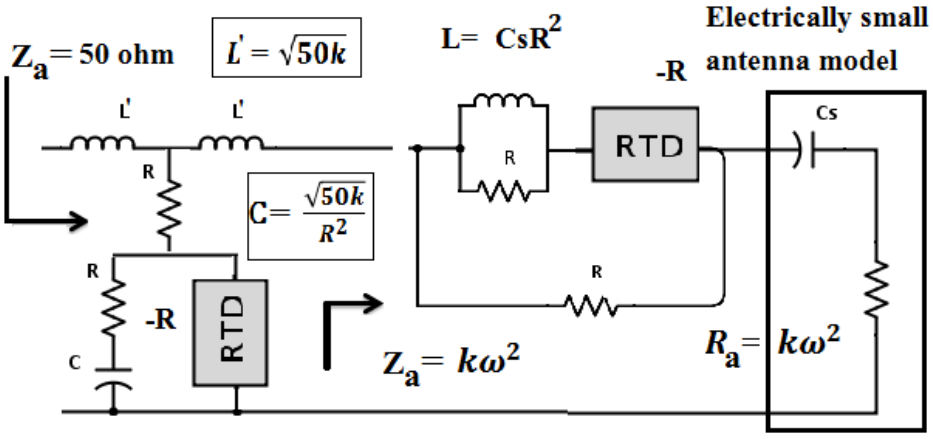

Figure 4.20: Matching of a capacitive ESA with two RTD devices. The capacitive part has been matched using the floating NFC circuit of Fig. 3.15(c). The resistive matching involves an RTD transformed to $-k\omega^2$ [5]. In this work, measured s-parameters of the RTD is used for circuit analysis of the matching network.

Table 4.1: Matching elements for antenna with 5 pF capacitance and frequency-dependent radiation resistance $R_a = k\omega^2$. ANT I is matched in the 1 to 2 GHz band. ANT II is matched at VHF/UHF.

Circuit elements	Ideal matching	Tuning ANT I	Tuning ANT II
Resistor (R)	-(RTD resistance)	52.7 Ω	60.2 Ω
Inductor 1 (L)	$C_s R^2$	41 nH	6 nH
Inductor 2 (L')	$\sqrt{50k}$	31 nH	13 nH
Capacitor (C)	$\frac{\sqrt{50k}}{R^2}$	12.5 pF	1.6 pF

pass the VHF and UHF bands, up to and around 1 GHz. In both these cases, the measured parameters from the RTD is used in simulation of Fig. 4.20. We note that an ideal RTD with reduced junction capacitance would match the antenna from 150 MHz to 5 GHz and above.

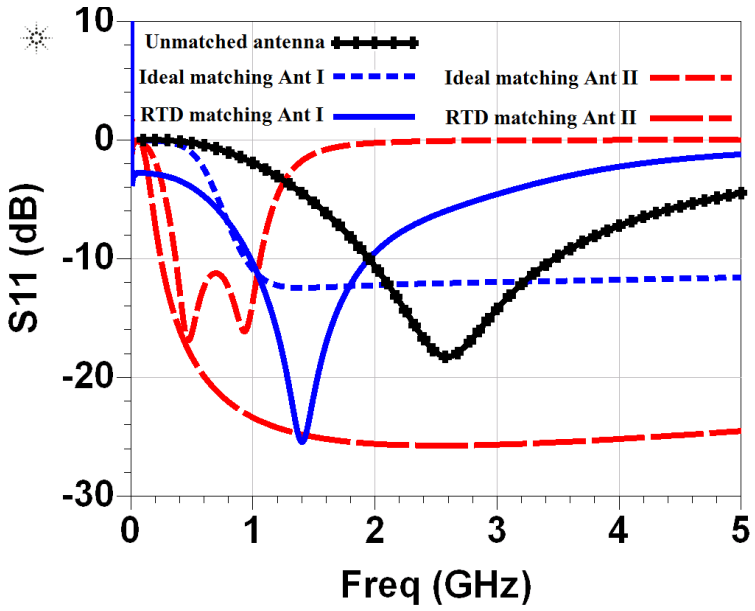

Figure 4.21: Reflection coefficient comparison with different matching approaches. The unmatched antenna resonates at around 2.5 GHz, and shows very poor matching at low frequencies. By varying the matching circuit with the elements from Table 4.1, very good impedance matching is demonstrated below 1 GHz, and from 1 to 2 GHz.

4.4 Summary

This chapter presents the fundamental limitations of the Q for an NFC integrated antenna. Later, the integration of BJT-based NFCs with the antenna has been carried out. A topology has been proposed for matching an ESA and a method for gain improvement using an NFC has also been discussed. An antenna design has been proposed, fabricated and tested in a conductive as well as a radiative environment. Far-field measurements below 500 MHz are not supported by the size of the anechoic chamber available, but are well covered by near-field measurement techniques. It has now been observed that the NFC integrated antenna exhibits some radiation efficiency improvements in near-fields from 300 MHz to 600 MHz. It implies a better impedance match as more energy is transferred to the antenna (assuming the source has the same level at all frequencies). Further, far-field mea-

surements have been carried out for 500 MHz and 600 MHz cases, which validate the near-field results. As the proposed antenna is electrically small in the VHF band, the improvement in radiation efficiency is one of the positive aspects of non-Foster techniques in the antenna applications.

In order to achieve broadband performance, RTD-based NFC devices may be used to match the impedance of both the resistive and reactive parts of an ESA over bandwidths that are not possible using the regular BJT-based NFCs or passive matching techniques. An antenna which is resonant at 2.5 GHz is matched to better than 10 dB return loss for two cases: (1) from 1 to 2 GHz and; (2) for VHF/UHF bands up to 1 GHz. This could be potentially useful in low-power, wide-band receiver applications. Further, an RTD-based NFC antenna is needed to be prototyped and measured.

Finally, the inclusion of active devices in the antenna leads to additional noise, which in turn affects the performance of the non-Foster integrated antenna in receiver applications. The noise present in the NFCs, which is subsequently carried to the antenna and receiver, affects the overall system performance; this is examined in further detail in the next chapter.

Chapter 5

Noise Analysis and System Performance of Non-Foster Antennas

This chapter presents the simulation and testing of noise figures for a two-port BJT-based NFC which has been prototyped in chapter 3. As the NFC is not a gain device similar to a low-noise amplifier, the possibility of uncertainty in noise figure measurements is quite high. The measurement exhibits minimum variation and validates the theoretical uncertainty in calculations. Due to the noise figure associated with NFC, it imposes certain restrictions on the scope of SNR improvement in receive mode NFC integrated antennas. Furthermore, the SNR improved bandwidth is calculated for the antenna prototype integrated with NFC. The radiation and SNR improvement bandwidth in NFC integrated antenna has been analysed which paves the investigation for the possibility of simultaneous power and information transfer of communication system in terms of channel capacity and power delivery respectively.

5.1 Noise in transistors

Apart from the improvement in bandwidth, as discussed in previous chapters, the study of noise introduced due to active circuitry is an important aspect for research in the non-Foster impedance circuits. The active element constitutes the primary source of noise with the additional cumulative effects of NFC load noise and loop resonator noise. The noise figure of an antenna is also dependent upon its aperture size and are related to each other in inverse proportion[103]. As there is a necessity to keep the antenna electrically small, the noise figure improvement is challenged with the increase in physical size and it is preferred to select high noise performance transistors. Selecting a suitable transistor can mitigate the noise addition to the NFC integrated antenna.

In the case of BJT-based NFCs, a BJT pair is connected in with the feedback loop which drives the current from lower potential to a higher potential in order to develop a negative impedance at the input terminals. These BJTs exhibit mainly shot, flicker and thermal noises. The flicker noise in a transistor is relatively very low [104, 105] at high frequencies as it is inversely proportional to the frequency and sometimes called as $1/f$ noise. In VHF and microwave frequency regime, the flicker noise does not have an effective contribution to the overall circuit noise. Also, non-linearities in NFCs along with the Johnson-Nyquist noise from the conductive losses have a considerable effect in terms of noise addition [98]. Practically, by employing a unique design topology, it is possible to minimise Johnson-Nyquist noise in NFC circuits. Hence, it is understood that these transistors are the main source of shot or i^2 noises which has a significant contribution in overall NFC noise. The noise model of BJT comprises of two "shot-noise" gen-

erators for each of its two junctions and a thermal noise generator located in the base region. The detailed analytical noise model of the transistor is published in [106, 107, 108, 109].

Transistors are used in the microwave field as an efficient active device which facilitates a simple way to evaluate the and characterise performances of active devices. The characterisation of any two-port network requires the determination of its four noise parameters that are, the minimum noise figure F_{min}, equivalent noise resistance R_n , optimum source complex admittance Y_{opt} and source admittance Y_s. The relationship between these parameters [110] is expressed as

$$F = F_{min} + \frac{R_n}{G_s} \mid Y_s - Y_{opt} \mid^2 \tag{5.1}$$

where $Y_s = G_s + jB_s$ is the source admittance.

The design of a low-noise amplifier is governed by these noise parameters. The design involves a technique based on Smith's chart using the constant noise figure encircles to achieve the required trade-off between noise figure and the available gain [111]. However, this approach is not valid for a two-port network subjected to a feedback impedance such as an oscillator or broadband amplifier [112]. The BJT-based NFCs presented in this thesis has a similar positive feedback configuration. The effect of feedback on noise figures is analysed using a set of equations that lead to highly accurate practical noise figure measurements. Niclas [113] described a specific case of a transistor with lossy input and output matching in a lossy feedback network. However, the results are not generic in nature. Also, Iversen [114] estimated that the correlation admittance is required to calculate overall noise figure. Later, Lam [115] explains use of basic noise figure equation

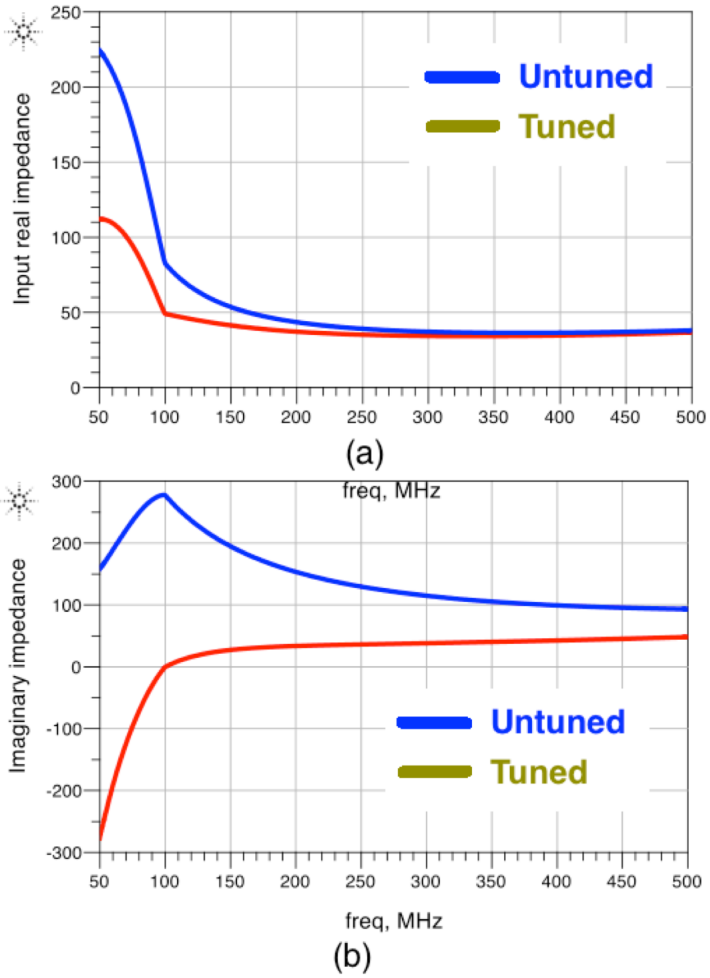

Figure 5.1: The input/output impedance of two-port NFC (a) untuned (b) tuned. The passive matching network required at both ports to tune the impedance and minimise the mismatch loss.

(5.1) and immittance parameters to obtain the noise figure of a two-port network with feedback. These parameters also reflect the contribution of feedback network to the circuit. Since, NFC design based on the transistor with feedback mechanism is an integral part of receiver circuit, the study and analysis of noise contribution in the BJT-based NFC is critical.

5.2 Noise figure in BJT-based NFC

An important aspect of BJT-based NFC prototype developed in chapter 3 is the analysis and measurement of noise which has been introduced primarily by the transistors. The noise figure in a NFC is an important parameter for further applications. This indicates to be the main motivation behind the use of a two-port design and not directly integrating the NFC with an antenna. The most challenging aspect of the noise measurement is matching the input and output port impedance of the NFC for employing the Y-Factor technique. This can be resolved using an additional matching network to minimise the mismatch loss. The real/imaginary input impedance of the non-tuned and tuned matching have been shown in Fig. 5.1. The simulated noise figure using tuned matching at NFC ports is shown in Fig. 5.2. It is common to encounter noise figure measurements of two-port NFCs that differ from simulation results which may be due to various reasons. It may probably persist due to the inaccurate consideration of all possible noise parameters in the simulation model. Also, these parameters include solder joints between components, noise characteristics of a non-linear substrate, passive components and microstrip traces which cumulatively affect the real circuit.

The other issue to be noted is that of noise figure uncertainty in measurements that leads to further inaccuracies. This uncertainty is due to the errors within components and circuit of measuring instruments. This also includes errors due to the analog-to-digital converter, detector, mixer non-linearities, analytical round-off effects, saturation effects and gain instability during measurements. Another cause for uncertainty may explained away due to the mismatch which is a reflection between the device under

consideration and the devices that follow it. The standing waves makes the power to emerge from source (incident to the load) to change from its initial value with a reflection-less load. This uncertainty can be minimised by careful selection of measurement components and with the use of relevant mitigation techniques.

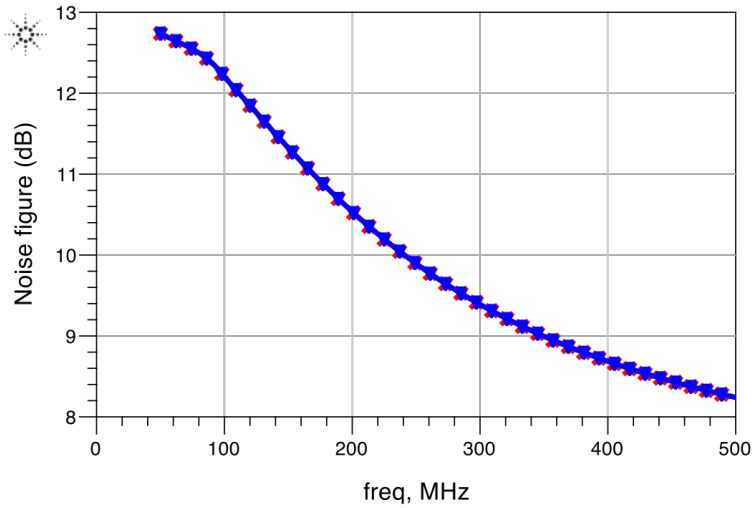

Figure 5.2: The noise figure of simulated NFC using Keysight ADS simulator. The simulation consider the noise model of the BJT for more realistic results.

5.2.1 Noise measurement technique

A noise source must have a calibrated output noise level to make significant noise figure measurements. It is represented by the excess noise ratio (ENR). ENR is expressed in dB as a difference between hot temperature (T_h, noise source ON) and cold temperature(T_c, noise source OFF), divided by the room temperature(T_0).

$$ENR_{dB} = 10log_{10}\frac{T_h - T_c}{T_0} \tag{5.2}$$

A low ENR noise source is advantageous if noise figure of the device under test (DUT) is very low. Also, it is favourable if the impedance match between the noise source and DUT changes minimally while toggling the source between ON and OFF states. A low ENR source contains an inbuilt attenuator which limits the ENR and reduces the sensitivity in reflection coefficient between both the states. In this thesis, the gain and output noise of the BJT are sensitive to changes in input impedance which can lead to errors in both gain and noise figure measurements. Additionally, it is noted that with a lower difference between the noise source ENR and the DUT noise figure there are higher chances of accurate measurements. For these measurements, an Agilent 346B noise source is used with an ENR of 14-15 dB. Corrections are also applied for the adapter losses of connectors between the concerned devices. The Friis formula discussed in the appendix gives noise factor (linear scale noise figure) of a cascaded system as

$$F_{total} = F_{DUT} + \frac{F_{instrument} - 1}{G_{DUT}} \tag{5.3}$$

The second quantity in (5.3) is often called the second stage contribution. The effective noise factor for the measurement instrument should be small. This indicates that with second stage contribution being negligible, the total noise factor measured will determine the overall noise factor of DUT.

The total noise factor (F_{total}), DUT noise factor (F_{DUT}), and DUT gain(G_{DUT}) depend on the reflection mismatch at the noise source output Γ_{source} [116, 117]. Similarly, noise figure of the second stage measurement equipment is a function of the DUT output reflection coefficient Γ_{output}. This leads to

modification of (5.3) as

$$F_{total}(\Gamma_{source}) = F_{DUT}(\Gamma_{source}) + \frac{F_{instrument}(\Gamma_{output}) - 1}{G_{DUT}(\Gamma_{source})} \tag{5.4}$$

For the calculation of the DUT noise figure, the value of Γ_{source} at each measurement frequency is required. Also, the S-parameter matrix of the DUT is necessary to calculate the G_{DUT} and Γ_{output}, while the four noise parameters of receiver are required to calculate the $F_{instrument}(\Gamma_{output})$ using (5.4). However, this technique provides an insertion gain measurement instead of a power gain measurement and gives $F_{instrument}(\Gamma_{source})$ instead of $F_{instrument}(\Gamma_{output})$. This error can be reduced by inserting a tuner between the DUT and the measurement receiver to achieve $F_{instrument}(\Gamma_{output})$ $= F_{instrument}(\Gamma_{source})$. Nevertheless, this leads to the need for considering the tuner attenuation and becomes cumbersome for broadband measurements [118]. To overcome this tedious method, inserting a low-noise pre-amplifier between the DUT and receiver is a better way to achieve more accurate measurements.

$$F_{instrument+preamp} = F_{preamp} + \frac{F_{instrument} - 1}{G_{preamp}} \tag{5.5}$$

As shown in (5.5), the pre-amplifier reduces the noise figure of the measurement instrument to such an extent that the numerator of the second stage contribution term in (5.3) and (5.4) is very small making the denominator of DUT gain term to be low. Some spectrum analysers have an inbuilt pre-amplifier option, but some need an external one. The measurements carried out here use the Rohde and Schwarz FSP40, which contains no inbuilt pre-amplifier. The application firmware FSV-K30 provides an enormous reduction in instrument noise figure. If the instrument noise figure

is already lower than that of the pre-amplifier selected, the pre-amplifier would only reduce measurement accuracy. The noise source used is connected to the 28V dc supply from the front panel of the spectrum analyser and has an ENR of 14-15 dB in the desired measurement bandwidth. This noise source connected to the DUT input and output is further connected to the measuring instrument as shown in Fig. 5.3.

The measurement of the noise figure has been performed in a mini-anechoic chamber to avoid the interference of surrounding noise as shown in Fig. 5.4 (a). As the input and output ports of the NFC are not matched to 50 Ω, a passive π-network is used which can match the NFC ports at the measurement frequency and minimises the mismatch loss. Later, this noise induced by the additional network is de-embedded. A single measurement of the noise figure by considering enough resonance points is shown in Fig. 5.4 (b). Multiple runs may lead to variation in measured data to a considerable extent, which has already been defined as the noise figure uncertainty. A sample size of 10 measurements is plotted in Fig. 5.4 (c), along with the maxima - minima envelopes and mean values against the frequency. At each frequency point, the maximum variation relative to the mean values is considered as the calculated noise figure uncertainty from the measurement data available.

$$NF_{uncertainty} = \frac{NF_{max.}(dB) - NF_{min.}(dB)}{NF_{mean}(dB)} * 100 \tag{5.6}$$

Where, $NF_{max.}$, $NF_{min.}$ and NF_{mean} are maximum, minimum and mean noise figures respectively, among all iterations at the frequency of interest.

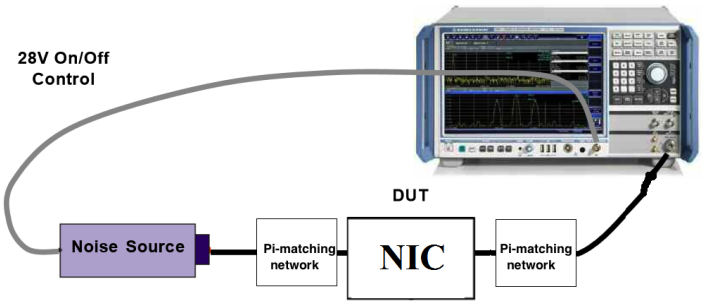

Figure 5.3: The noise figure measurement setup showing the NIC/NFC as DUT. The mismatch losses between each junction is minimised by additional π-matching network.

5.2.2 Noise figure uncertainty calculation

The sources of uncertainty are mainly due to the ENR of noise source, impedance mismatch between the noise source and the instrument during the calibration process and the impedance mismatch at each of the three junctions among the noise source for the DUT and instrument in the measurement process [119]. It is very common to observe some random jitters during measurement and hence, it is a good practice to take an average over a sufficient number of readings.

Taylor's theorem can be applied to find the uncertainty of F_{DUT},

$$\delta F_{DUT} = \frac{\partial F_1}{\partial F_{total}}\delta F_{total} + \frac{\partial F_1}{\partial F_{DUT}}\delta F_{DUT} + \frac{\partial F_1}{\partial G_{DUT}}\delta G_{DUT}. \tag{5.7}$$

The three uncertainty terms are due to the measurement instrument, i.e. the spectrum analyser (SA) and DUT. The ENR of the noise source also contributes to the uncertainty and needs to be included in the scenario. The overall uncertainty equation in dB is given as

$$\delta NF_{DUT} = \sqrt{P^2 + Q^2 + R^2 + S^2} \tag{5.8}$$

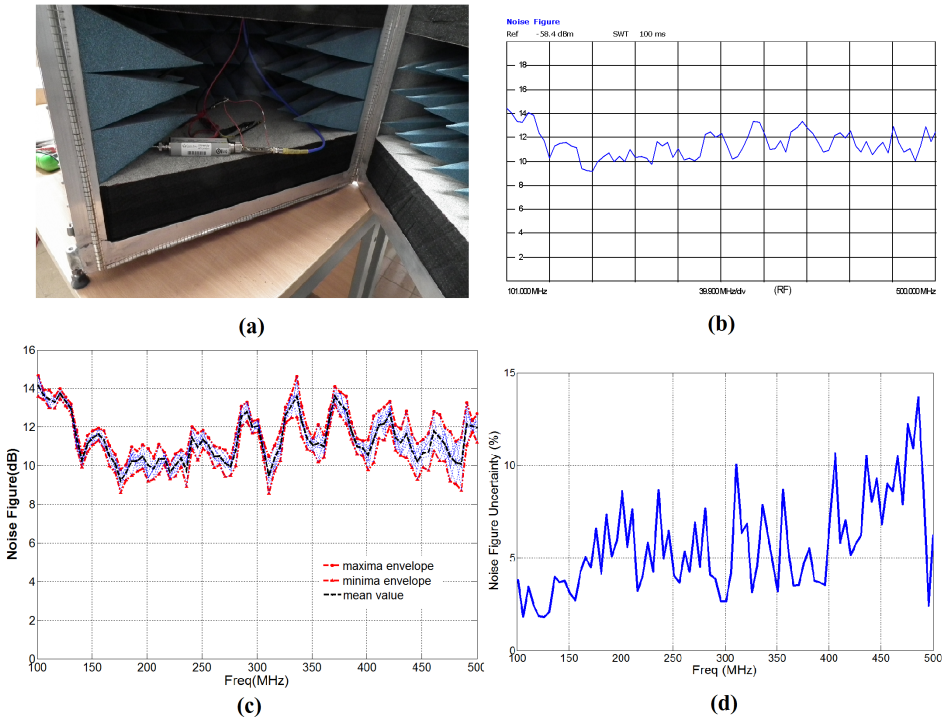

Figure 5.4: (a) Noise measurement setup in mini-anechoic chamber (b) A single noise figure measurement (c) Multiple measurement analysis of noise figure (d) Noise figure uncertainty.

Where,

$$P = \frac{F_{total}}{F_{DUT}} \delta NF_{total} \tag{5.9}$$

$$Q = \frac{F_{SA} - 1}{F_{DUT} G_{DUT}} \delta NF_{SA} \tag{5.10}$$

$$R = \frac{F_{total} - 1}{F_{DUT} G_{DUT}} \delta G_{DUT,dB} \tag{5.11}$$

$$S = \left(\frac{F_{total}}{F_{DUT}} - \frac{F_{SA}}{F_{DUT} G_{DUT}} \right) \delta ENR_{dB} \tag{5.12}$$

The standing wave generated at each interface due to the mismatch also contribute to uncertainties. These calculations are based on the reflection coefficient. There are negative or positive uncertainty values and the one

Table 5.1: Mismatch uncertainty at each junction as shown in Fig. 5.3

Interface	Symbol	Maximum uncertainty
Noise source to DUT input	δ_1	0.33 dB
DUT output to SA input	δ_2	0.5 dB
Noise source to SA input	δ_3	0.22 dB

with a larger magnitude is considered for that particular interface. The negative uncertainty is equal to -20log(1-Γ_{Source} Γ_{Load}) dB and the positive uncertainty is equal to +20log(1+Γ_{Source} Γ_{Load}) dB. As shown in Table 5.1, maximum uncertainties of all interfaces are reported with the information about reflection coefficients. The total noise figure uncertainty of the DUT and SA connected in cascade is calculated as

$$\delta NF_{total} = \sqrt{\delta_1^2 + (SA_{NF-uncertainty-dB})^2}. \tag{5.13}$$

The uncertainty in the calibration of SA noise figure is given as

$$\delta NF_{SA} = \sqrt{\delta_3^2 + (SA_{NF-uncertainty-dB})^2}. \tag{5.14}$$

Similarly, the uncertainty in gain measurement of DUT is

$$\delta G_{DUT} = \sqrt{\delta_1^2 + \delta_2^2 + \delta_3^2 + (SA_{NF-uncertainty-dB})^2}. \tag{5.15}$$

The noise source ENR values are also uncertain in nature as they are specified by the supplier as approximately 0.2 dB (δENR_{dB}= 0.2 dB) in the Agilent 346B noise source data-sheet [120]. The noise figure uncertainty of the spectrum analyser after loading the FS-K30 high precision noise figure measurement firmware[121] is reduced to 0.05 dB ($SA_{NF-uncertainty-dB}$= 0.05

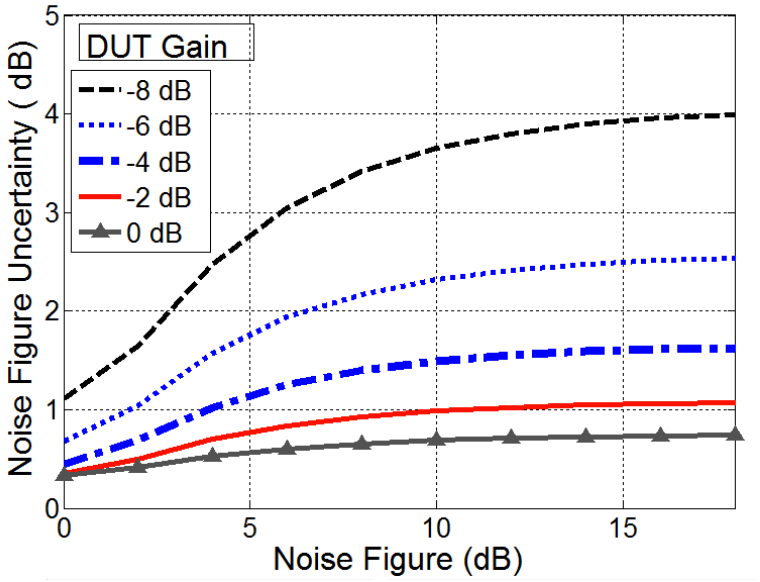

Figure 5.5: Variation of noise figure uncertainty with DUT noise figure. The uncertainty is increasing with the DUT insertion loss.

dB), as claimed by the supplier. The equations (5.13),(5.14) and (5.15) are substituted in (5.12) for the calculation of noise figure uncertainty of DUT with (5.8). It is assumed that the total cascaded noise figure is equal to the noise figure of DUT as the firmware FS-K30 reduces the noise figure of spectrum analyser to an extremely low value.

As shown in Fig. 5.4 (d), the maximum noise figure uncertainty measured for the NFC across the frequency band is 13.8%. The theoretical analysis of the measurement uncertainty is shown in Fig. 5.5. As the DUT has 4 dB insertion loss and approximately 10 dB noise figure, a maximum uncertainty of 1.5 dB is observed from the figure (i.e. 15%). Hence, this theoretical analysis closely matches with the measurement.

The noise analysis and measurement of two-port floating BJT based NFC circuit has been carried out using the conventional Y-factor method with few adjustments. Additional pre-amplification is required for overcoming poor gain issues of the NFCs, which is achieved by employing a pre-amplifier.

Also, a tuning circuit is used to reduce the mismatch at the noise measurement frequency, since the NFC is not terminated at 50 ohms, across the band. The device noise figure ranges between 9 dB to 14 dB through the band of 100 MHz to 500 MHz. The simulation output suggests close agreement with the measured results as well as analytical calculations. Also, it is observed that the uncertainty in the noise measurement is pertinent due to the low gain and unwanted mismatch losses even after tuning both the ports of the DUT. Though, non-Foster matching in receiver mode improves the bandwidth but with the presence of high noise figures, the integrated BJT-based NFC device poses to be a possible source for degrading SNR. The SNR improvement is limited by a few factors which will be discussed in the next section.

5.3 Fundamental limit for SNR improvement

The NFC integrated antennas in receive mode have added noise with the presence of active non-Foster element. This noise degrades the SNR in addition to the bandwidth improvement. The SNR improvement with the non-Foster matching antenna is discussed in [33], where one port grounded SCS NFC is integrated with the antenna. Signal and noise power has been received by the antenna in transmitter ON and OFF conditions respectively. The power has been measured with and without non-Foster matching by the receiver system. However, SNR improvement in [33] is not validated with the simulation and measurements. Also, the various other contributions of noise i.e., atmospheric noise, circuit noise and the receiver noise have not been addressed clearly.

At the front-end of receiver system, noise gets incorporated with the in-

put signal due to the atmospheric effects and unwanted signal interference. This result in the rise of noise floor and the signal strength gets degraded due to the path loss effect. Hence, SNR is an important parameter in the receiver chain. Also, the output SNR is dependent on the input SNR of the receiver and also with the noise figure of the receiver chain. The input SNR is a function of the power transmitted, antenna transmission gain, atmospheric transmission coefficient, temperature, receiver antenna gain and receiver noise figure.

This section goes further to define the fundamental limit of maximum noise added by non-Foster elements to achieve SNR improvements. Various parameters are studied to set the noise limit, and it has been noticed that the measured noise of non-Foster elements is beyond this noise limit in practical situations. This SNR degradation due to the noise introduced by active circuitry is the main reason for degradation of channel capacity and subsequently, the system performance of the receiver system.

5.3.1 Mismatch loss

The output of any antenna is connected to a low noise amplifier, which is the first component of a receiver chain. The amplifier has a low noise figure and high gain, which results in negligible second stage contribution. Thus, the internal noise floor of the receiver block emerges to be very close to the system noise floor and therefore adding minimal noise to the antenna output at SNR level. The reasons for SNR degradation are the mismatch loss and noise added due to the non-Foster circuitry. Apart from the noise introduced by non-Foster active circuitry, mismatch loss is often ignored in noise figure analysis, as mismatching loss equally attenuates the input signal and external noise thereby having no effect on the SNR at the output. The

mismatch loss (M) is the ratio of incident power to the difference between incident and reflected power.

$$M = 1 - |\Gamma|^2 \tag{5.16}$$

However, a poorly matched antenna with low radiation efficiency degrades the received power level below the receiver noise floor. This also occurs when the external noise level is not high on the internal noise floor. Therefore, the SNR obtained at the output of the antenna becomes internally noise-limited when the noise level is reduced below the system internal noise floor. A high noise figure is recorded due to the lowering of the SNR from the expected value. As discussed in chapter 4, an NFC integrated antenna improves the bandwidth while decreasing the mismatch loss when compared to the passive antenna. This is an important factor that explores the possibility of an improved SNR at the output of antenna as compared to the input terminal. The calculation of the minimum required noise figure of the non-Foster circuit is proposed in next section.

5.3.2 Calculation of non-Foster noise limit

The noise figure of a passive antenna and non-Foster antenna can be calculated from Fig. 5.6 using the Friis formula [122]. Detailed calculations of the cascaded noise figure is presented in Appendix A.

The noise factor for unmatched antenna is given as

$$F_{passive} = \frac{T_a M_p + T_{rx}}{T_a M_p} \tag{5.17}$$

In case of an antenna with efficiency η_a, the noise factor can be redefined

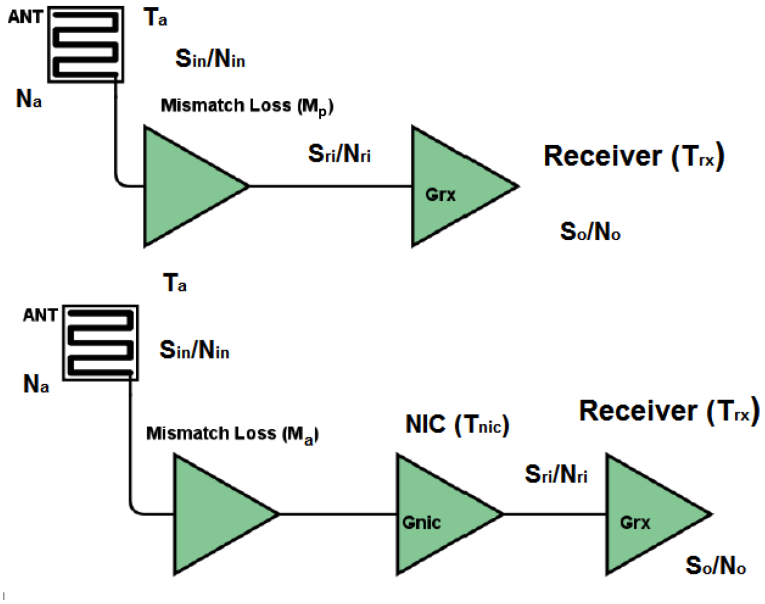

Figure 5.6: Noise figure analysis comparison between unmatched and non-Foster antenna. The mismatch loss reduction is achieved with non-Foster at the cost of added noise.

as [123]:

$$F_{passive} = \eta_a + \frac{M_p(1-\eta_a)T_0 + T_{rx}}{M_p T_a} \tag{5.18}$$

Also, the noise factor for the NFC matched antenna is given as

$$F_{non-Foster} = \frac{[(M_a T_a + T_{nfc})G_{nfc} + T_{rx}]G_{rx}}{G_{nfc}G_{rx}M_a S_{in} T_a}. \tag{5.19}$$

For an antenna with efficiency η_a, the noise factor from an antenna input to the receiver system, $F_{non-Foster}$ is redefined as

$$F_{non-Foster} = \eta_a + \frac{M_a(1-\eta_a)T_0 G_{nfc} + T_{nfc}G_{nfc} + T_{rx}}{M_a T_a G_{nfc}} \tag{5.20}$$

The maximum noise figure of an NFC or NIC added in order to achieve

the system SNR improvement is obtained from (5.18) and (A.17) if

$$F_{non-Foster} < F_{passive} \tag{5.21}$$

and,

$$\eta_a + \frac{M_a(1-\eta_a)T_0G_{nfc} + T_{nfc}G_{nfc} + T_{rx}}{M_aT_aG_{nfc}} < \eta_a + \frac{M_p(1-\eta_a)T_0 + T_{rx}}{M_pT_a} \tag{5.22}$$

$$\frac{T_{nfc}}{M_a} + \frac{T_{rx}}{M_aG_{nfc}} < \frac{T_{rx}}{M_p} \tag{5.23}$$

Substituting $M_f = M_a/M_p$ and further solving, we get

$$SNRIF = (1+(10^{NF_{rx}(dB)/10}-1)(M_f - L_{nfc})) - 10^{NF_{nfc}(dB)/10}; SNRIF > 0 \tag{5.24}$$

The factor SNRIF (SNR improvement factor) needs to be greater than zero in order to achieve SNR improvement with given parameters. The NFC loss factor, L_{loss} is given as $1/G_{nfc}$. Also, the mismatch factor M_f is the linear ratio of mismatch loss in matched and unmatched conditions. As the non-Foster elements improves the bandwidth, the majority of bandwidth M_f is typically greater than 1. M_f can be redefined using (5.16) as

$$M_f = \frac{M_a}{M_p} = \frac{1-|\Gamma_a|^2}{1-|\Gamma_p|^2} \tag{5.25}$$

where, $|\Gamma_p|$ and $|\Gamma_a|$ are the reflection coefficients in unmatched and matched antenna respectively.

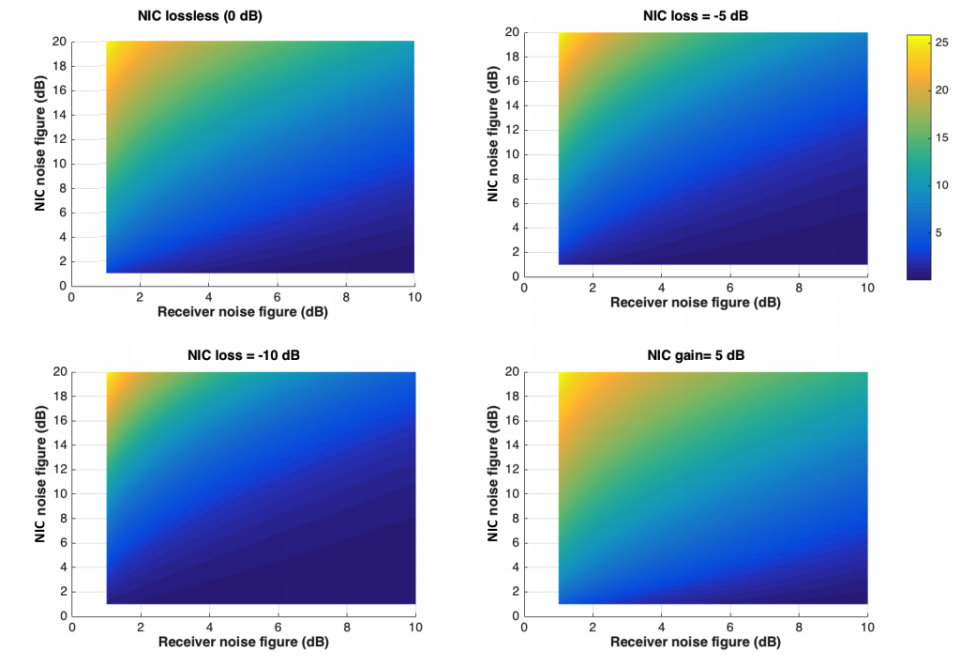

Figure 5.7: Mismatch factor requirements for the NFC-matched antenna. In this figure the mismatch factor requirement, M_f, is calculated such that SNRIF=0, which is the boundary representing improvement of the NFC-matched antenna compared to the passive antenna. For different NIC/NFC losses (or gain) (L_{nfc}), M_f is plotted for a range of values of the receiver noise figure, NF_{rx}, and the maximum acceptable noise figure of the NFC, NF_{nfc}. The colour bar shows the range of calculated M_f values, which represents the minimum value of M_f that would guarantee an improvement of performance of the NFC antenna compared to the passive antenna.

A poor receiver enhances the noise figure limit and a high gain (low-loss) NFC element decreases the noise figure limit. Furthermore, there is a trade-off between NFC gain and its stability. A two-port NFC with gain will oscillate, while a stable NFC will add insertion loss, resulting in G_{nfc} being between 0 and 1, while L_{loss} is would be greater than 1. It is evident from (5.24) that the dependency of the upper limit of NFC noise for SNR improvement is not critically dependent upon the NFC gain while M_f is the main influencing factor as the second term becomes negligible. Fig. 5.7 is the general calculation plot showing the range of M_f required to maximise the upper limit of NFC noise figure for SNR improvement with the variation

of receiver noise figure and different NFC gain/loss/lossless conditions. It is clearly visible from (5.24) and Fig. 5.7 that with a high value of M_f (or better matching), high noise figure of NFC element is acceptable for SNR improvement. The maximum value of M_f is also limited which is dependent upon the reflections in unmatched and matched cases.

The maximum value of M_f depends on the maximum of numerator and minimum of denominator. Ideally, $|\Gamma_a| = 0$ and numerator of M_f is equals to 1. Now, the minimum denominator of M_f is dependent upon the minimum value of M_p, which is dependent on the extremely high reflection coefficient Γ_p of a passive antenna across the bandwidth. The theoretical calculations considering the designed NFC whose insertion loss and noise figure is measured and known, is used with (5.24) to estimate the value of M_f required for achieving the SNR improvement.

5.3.3 Example calculation(NF_{rx}=3 dB, L_{loss}=4 dB and NF_{nfc}=10 dB)

It is beneficial to calculate the boundary at which a practical NFC-matched antenna will show improved performance compared to a passive antenna. In this subsection an example calculation is provided using (5.24) to estimate the bound of the return loss for a passive antenna which would guarantee the performance improvement of NFC antenna. Previously in this chapter, a non-Foster element (capacitive NFC) is individually characterised as a two-port device with 4-5 dB loss in the 100MHz to 500MHz frequency band and it has been noticed that the noise figure measured is 8 dB-12 dB range using the conventional Y-factor technique. The NFC loss factor, L_{loss}=4 dB= 2.5.

It is also assumed that receiver noise figure is 3 dB , $NF_{rx} = 3\ dB$ and noise factor of receiver is 1.99. We further consider an NFC noise figure of NF_{nfc}= 10 dB (noise factor=10) and in order to satisfy (5.24) we calculate,

$$(1 + (2 - 1)(M_f - 2.5) > 10 \Rightarrow M_f > 11.5 \tag{5.26}$$

for the bound SNRIF>0. As discussed in the previous subsection, for ideal NFC matching, Γ=0 (M_a=1), we therefore require $M_p < \frac{1}{11.5}$ in order to achieve the M_f inequality condition for an improved SNR. This in turn gives a range of values for the passively-matched antenna's reflection coefficient, for which the NFC antenna will have better performance.

$$|\Gamma_p| > \sqrt{1 - M_p} > 0.9555 \tag{5.27}$$

Hence, the condition of reflection coefficient for an unmatched antenna in ideal condition is

$$0\ dB > S_{11p} > -0.395\ dB \tag{5.28}$$

when matched antenna has reflection coefficient $S_{11a} = -\infty$ dB (or 0 in linear scale). From this result, it is clear that even a relatively poorly-matched passive antenna (say $S_{11p} = -3$ dB) will have a better performance than a high-noise NFC antenna.

In the previous calculation the requirement was set for a perfectly matched NFC antenna, with $S_{11a} = \infty$ dB. However, assuming that a non-ideal matching requirement is set, the reflection coefficient S_{11a}=-10 dB. In such a situation, M_a= 0.9486 and M_p<0.0824 for achieving the M_f>11.5 condition. Hence,

$$|\Gamma_p| > \sqrt{1 - 0.0824} > 0.9578 \tag{5.29}$$

and so, the condition for reflection coefficient across the band of an unmatched antenna to achieve SNR improvement, considering the matched antenna has 10 dB return loss, which tightens slightly to

$$0\ dB > S_{11p} > -0.373\ dB \tag{5.30}$$

This verifies that in order for a passive unmatched antenna to achieve SNR improvement with the integration of this particular NFC (NF=10 dB Loss= 4 dB) and a 3 dB receiver, it must initially have an extremely poor return loss. With the aforementioned NFC and receiver combination, SNR improvement is not possible for a passive antenna with return loss better than 0.4 dB. So, it is actually better for the antenna to remain unmatched, rather than to use this poorly performing NFC match.

The values considered in these example calculations are constant with frequency, but practical measured data is frequency dependent which has been introduced in the next subsection for the practical NFC integrated antenna.

5.3.4 SNR improvement bandwidth in proposed design

SNR improvement bandwidth can be defined as the frequency band for which an NFC integrated antenna has better SNR performance as compared to the unmatched antenna. In the practical conditions, the antenna under considerations has been designed, developed and measured in chapter 4 and is shown in Fig. 4.11. The reflection losses in the antenna for both, the matched and unmatched condition are shown in 4.14. As shown in Fig.5.4, the measured noise figure of a non-Foster element has been measured alone across the frequency band. Additionally, the insertion loss of the NFC has

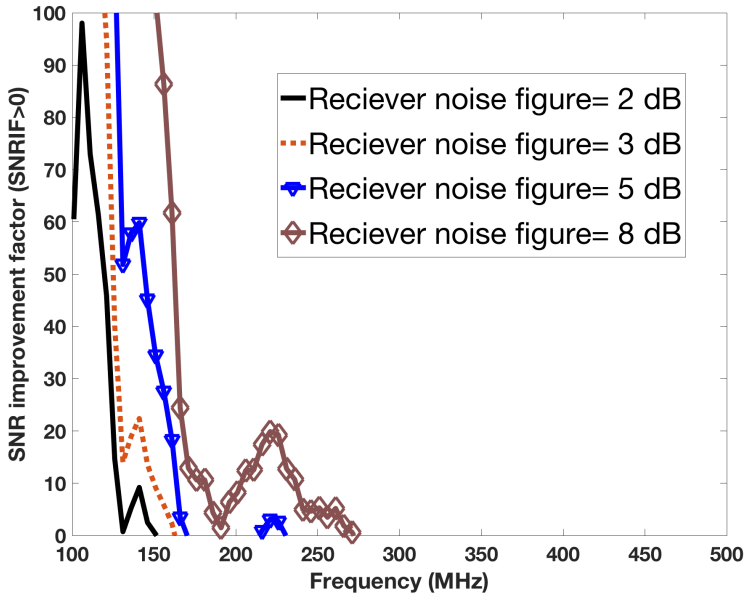

Figure 5.8: The variation in SNR improvement factor with frequency in the non-Foster integrated antenna with different receiver noise figure. SNRIF>0 is achieved for wideband frequencies using a poor receiver. 50 MHz and 170 MHz bandwidths are attained with 2 dB and 8 dB receiver respectively.

been measured in chapter 3.

Using the mentioned measured data in (5.24), the SNRIF has been calculated for different receiver noise figures as shown in Fig. 5.8. As discussed earlier, the SNR improvement is highly dependent upon the condition SNRIF>0 and it has been noticed from Fig. 5.8 that SNR improvement bandwidth is limited by the high end receiver selection which validates the work presented by Sussman-Fort [33]. A poor receiver results in a wider SNR improvement bandwidth and this affects the system noise performance, while it is difficult to achieve a reasonable bandwidth using the expected high quality receiver. As shown in Fig. 5.8, a 2 dB noise figure receiver is able to provide 50 MHz bandwidth while 8 dB receiver is offering 170 MHz bandwidth approximately. This bandwidth is attained at different frequencies and it is much less than the impedance matching bandwidth

and radiation bandwidth discussed in chapter 4. The effect of non-Foster noise and limited SNR improvement on the system performance is discussed in the next section.

5.4 Channel capacity and power delivery

In a communication system, the antenna application for information transfer is presented in [124, 125], whereas an antenna for power transfer applications is exploited in [126, 127, 128]. The narrowband behaviour of an ESA restricts its applications for simultaneous information and power transfer capabilities [129, 130]. A pair of identical ESAs are tuned to resonate at same frequency; one acts as a transmitter and delivers the maximum power to the receiving ESA placed in the far-field [130]. Due to this narrowband characteristic of both the ESAs, we assume that the bandwidth is nearly zero and hence, the capacity for information transmission is zero. The increase in information carrying capacity is possible by reallocating the input power over a selected bandwidth instead of the power input at resonance frequency. This technique of power allocation to sub-channels is termed the water filling algorithm [131]. The power allocation channels are decided based on the impedance/radiation bandwidth and hence are dependent upon the type of matching. The investigation for the performance of non-Foster integrated antennas is being performed to maximise the total channel capacity and deliver power simultaneously.

Shannon's channel capacity equation [132] presents the maximum rate of data transmission over a system when the signal is perturbed by noise produced by various sources. As discussed in chapter 4, the purpose of the non-Foster approach is to reduce the Q-bound and improve the impedance

and radiation bandwidth for power transfer. However, as discussed in the previous section, the noisy NFC matched antenna has limited SNR improvement as compared to its passive counterpart. Subsequently, it limits the channel capacity and the ability for information transfer in the communication system. It is the conventional belief that the only way to achieve a reliable communication link over a noisy channel is to minimise the error probability, by reducing the data rate. Shannon exhibited that communication can take place at a certain maximum rate, called the capacity of the channel, with a specified minimum error probability [132].

The power transfer in the receiver antenna system is dependent on the radiation bandwidth, while the non-Foster integration improves the total power delivered to the receiver as discussed in chapter 4. However, the information transfer to the receiver has been estimated with Shannon's channel capacity calculation. The maximum channel capacity estimates the maximum data rate that is possible with the given antenna receiver system. The Shannon's capacity considers the maximum data rate in the presence of noise. In this calculation, it has been assumed that both the noise as well as the received signal have a Gaussian distribution. In consideration of the water-filling algorithm, the input power is equally distributed to the N channels with a constant bandwidth, ΔB and also, the SNR at different channels are considered in power allocation processes. The total channel capacity is given [133] as

$$C_s = \sum_{m=1}^{M} \log_2 \left[1 + \frac{\eta_p(f_m) P_i(f_m)}{P_N(f_m)} \right] \Delta B \tag{5.31}$$

Where, $P_i(f_m)$ is the input power allocated to the i^{th} frequency band ΔB. $\eta_p(f_m)$ is the efficiency of power transmission between transmitter and re-

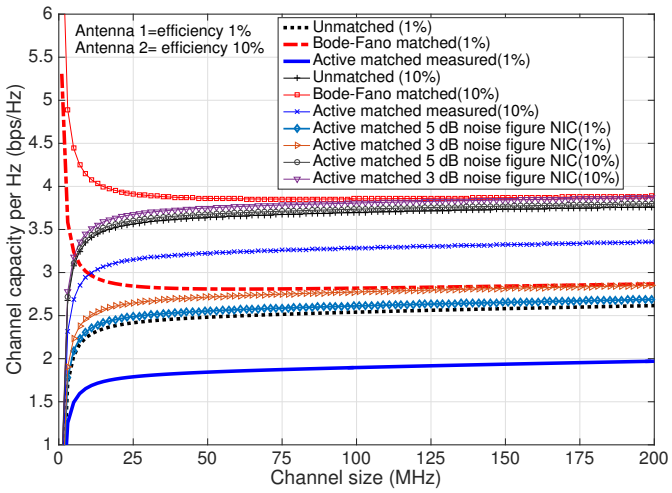

Figure 5.9: Channel capacity per Hz bandwidth with different channel sizes. Bode-Fano matching improves channel capacity for small channels due to narrowband characteristics. The NFC integrated antenna has poor channel capacity as there is no SNR improvement in the impedance/radiation bandwidth. Low noise figure conditions and high efficiency can improve the channel capacity and system performance.

ceiver. $P_N(f_m)$ is the introduced noise power to the system. Input power, added noise power and efficiency are all frequency dependent parameters.

The total channel capacity per unit bandwidth has been estimated in the unmatched antenna, passive matched antenna and the non-Foster matching conditions. In all three cases, the variation of the total channel capacity per unit bandwidth with different channel bandwidth from 1 MHz to 200 MHz is shown in Fig. 5.9. The total channel capacity is directly proportional to the efficiency. Hence, 10% efficiency antenna has better information transfer capacity as compared with identical 1% efficient antenna. The passive matching (Bode-Fano limit) can overcome the channel capacity of the unmatched antenna for small channel size, i.e. up to 5 MHz channel size in 1% efficiency antenna and up to 27 MHz channel size in 10% efficiency antenna. The improvement in Bode-Fano passive lossless matching is due to the absence of noisy active elements as in non-Foster active matching tech-

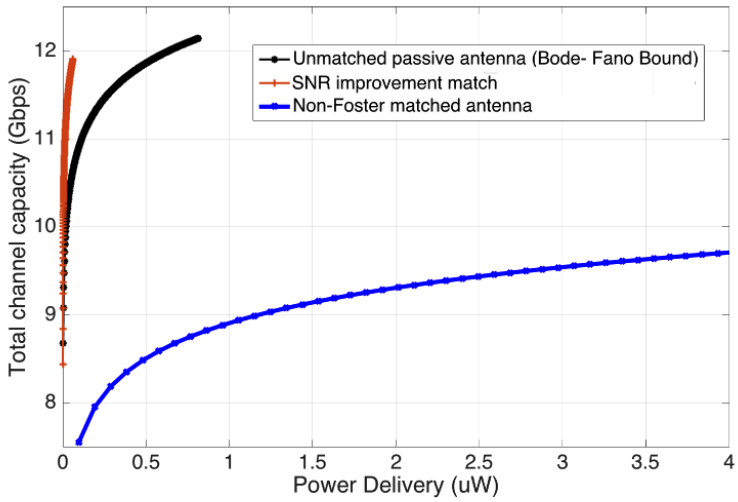

Figure 5.10: The power delivery is improved with non-Foster antennas, but the information carrying capacity decreases as compared to the passive antenna. Additionally, it decreases in comparison to the SNR improvement match case, where the input power is allocated in the SNR improvement frequency band, as shown in Fig. 5.8. The power delivery is minimal in this case because of poor impedance matching or radiation efficiency at the SNR improvement bandwidth.

nique. The measured noise figure of the NFC is high, which in turn limits the SNR improvement bandwidth under 300 MHz as discussed in the previous section. Fig. 4.18 shows that the non-Foster matching may improve the radiation efficiency from 300 MHz to 600 MHz. Thus, the input power is allocated into the channels within the aforementioned band using the water-filling method. The non-Foster integrated antenna presented in this thesis has radiation bandwidth different from its SNR improvement bandwidth. As shown in Fig. 5.8, there is no SNR improvement in the received non-Foster matching/radiation bandwidth and therefore, the total channel capacity falls even with SNR improvement. Hence, the developed NFC in this thesis has high noise figure and with an NFC noise figure of, say 5 dB or better can improve the SNR and channel capacity as shown in Fig. 5.9.

The power delivery (P_d) from the two identical antennas, one acting as

a transmitter and the other as a receiver, can be calculated [133] as

$$P_d = \sum_{m=1}^{M} |P_i(f_m)\eta_p(f_m)| \tag{5.32}$$

Where, $P_i(f_m)$ is the input power allocated to the i^{th} frequency band similar to the (5.31). Also, $\eta_p(f_m)$ is the power transmission efficiency between the identical transmitter and receiver antennas. A pair of identical NFC integrated antenna have an effective improvement in power transfer capability over their passive counterparts irrespective of SNR improvement constraints. However, the receiver antenna has poor SNR in the non-Foster matching bandwidth, which adds noise to the received signal. For an input power in the range of μW, the total power delivered to the receiver is improved for the NFC integrated antenna, however, the total channel capacity is degraded in comparison to the passive antenna, as shown in Fig. 5.10. In the case of power allocation to channels in SNR improvement bandwidth instead of impedance/radiation bandwidth, the power delivery is negligible due to high mismatch loss.

This analysis for estimation of the total channel capacity and power delivery contradicts the conclusions of Yeung [133], where it is reported that non-Foster matching improves the total channel capacity and power delivery simultaneously. This difference in the presented work is primarily due to two reasons: firstly, the radiation improvement frequencies of the presented NFC matched antenna do not coincide with the SNR improvement frequencies and; secondly, [133] does not consider the high noise figure of the NFC which is mainly responsible for the degradation of total channel capacity.

5.5 Summary

This chapter analyses the inclusion of active noise on antennas with integrated non-Foster characteristics. The noise introduced in the NFC has been studied through simulation and measurements. The condition for SNR improvement has been derived and the effect of the high measured noise figure of the NFC has also been discussed. The output SNR improvement is dependent on the increased magnitude of all quantities except for the receiver noise figure. The reduction of receiver noise figure further enhances the output SNR. This high noise figure results in practical limitations for achieving SNR improvement with non-Foster integration of antennas. In the presented practical non-Foster integrated antenna, there is no overlap between the SNR improvement bandwidth and true matching bandwidth. Hence, the total channel capacity degrades with the non-Foster integration. SNR degradation has no effect on the total power transferred to the receiver block by the non-Foster integrated antenna owing to its broadband characteristics. However, the total channel capacity of the receiver system is affected, which limits the applications of non-Foster integrated antennas for information or data communication. Also, an NFC as a gain device which does not perform well with stable operation and a lossy NFC offers limited improvement in the efficiency of the antenna, that depends on the matching improvement. An NFC integrated antenna with overlapping radiation bands and SNR improvement bandwidth could in theory, improve the total channel capacity. Also, an NFC with a reasonably low noise figure could improve the SNR over the desired band. However, it is not possible to realise such an improvement in this work and the analysis presented here indicates that it may be doubtful to attain an overall channel capacity improvement.

Chapter 6

Conclusions and Future Work

6.1 Conclusion

In Chapter 2, a detailed literature review for the realisation of two-port network has been presented along with the various methods for NFC stabilisation and different techniques for achieving non-Foster impedance. Further, the detailed background of the non-Foster matching of antenna has been discussed.

Chapter 3 deals with the design and development of an open circuit stable, two-port floating, BJT-based negative capacitance NFC prototype. The measurement results of the stable fabricated sample showed decent agreement up to 1 GHz. Also, the design and stability analysis of a graphene FET based NFC has been investigated. Further, a novel and stable RTD-based non-Foster impedance circuit has been proposed. Capacitive and inductive NFC measured results agreed well with the simulations and ideal characteristics up to 2 GHz.

Chapter 4 defines the minimum Q for a non-Foster antenna, furthering the practical NFC integration with small antennas. Broadband impedance

matching up to 1 GHz has been achieved and a limited true radiation bandwidth improvement from 300 MHz to 600 MHz has been validated for BJT-based NFC integrated antenna with near-field and far-field measurements. Similarly, an RTD-based NFC solution for broadband matching of ESA model has been attained. However, further development and measurements of RTD-based NFC integrated antenna is still under progress.

Chapter 5 investigates the total noise added to the circuit due to non-Foster inclusion. The transistor shot noise dominates the overall noise and the most contributory in the noise figure of NFC. This chapter also presents the measurements of noise figure of BJT-based NFC as 9 dB to 14 dB in the frequency range of 100 MHz to 500 MHz. The high noise figure was also analysed to obtain the SNR performance of the non-Foster integrated antenna in receive mode. The presented analysis shows that the BJT-based non-Foster antenna is broadband in nature and can improve the power reception in the communication link. However, the SNR improvement frequencies are not same as the frequencies showing improvement in radiation characteristics. Hence, the total channel capacity and system performance degrades with the inclusion of the active devices. An NFC with low noise figure (<5 dB) can improve the system performance and the same has not as yet been realised.

Non-Foster based active MTMs applied as an electromagnetic absorbers or reflector designs with wide-band performance do not require the gain behaviour of the NFC. These do emerge to be potential candidates for application with the existing performance of NFCs. In Appendix B, a proposed use of a compact, flexible and less stability sensitive RTD-based NFC is examined for integration with MTM absorber to give wideband performance (0.6 GHz to 1.1 GHz) and up to 45° angle of incidence.

6.2 Future work

The high noise figure of BJT-based NFCs presents a challenge for the use of devices in receive mode antennas. Also, antenna array application is restricted due to the additional factors, i.e. design complexity, form factor, poor parasitic control and high stability sensitivity. The advantages of RTD-based NFCs over BJTs makes them a highly potential candidate for array configuration. As the noise figure of RTD-based NFCs is not yet performed due to the availability of limited diode samples. The noise figure of an RTD-based NFC needs to be measured and should fall below the estimated noise figure limit for a non-Foster matched antenna.

These BJT and RTD-based NFCs have non-linearity issues in the transmit mode. The NFC impedance may vary with increasing input power and affects the matching capability. A large-signal non-linear model is required to be developed for each design approach to estimate the maximum input power that can safely be applied without affecting the performance.

The present BJT-based non-Foster integrated antennas are only suitable for improving power reception and not for information or data reception due to the high added noise. Additional work is required to minimise the effects of added non-Foster noise to the system. These NFCs are suitable for metamaterial applications since, the noise and gain parameters of NFC are not primary concerns, as is the case with antennas. Further efforts are needed to be put in for prototyping and testing of the presented RTD-based metamaterial absorber. Also, the RTD-based high impedance surfaces need to be designed and implemented. Further, credible work has to be done on the new fundamental limits of the thin active metamaterial absorber and high impedance surface, beyond the existing passive design.

Appendix A

Friis formula calculation for a non-Foster system

A.1 Basics of Friis formula

Noise factor (F) for a two port device or element is a figure of merit that relates the SNR of the input to the SNR of the output. A device with added noise N_a and gain G is shown in Fig. A.1 and the equation of noise factor is given as

$$F = \frac{(S/N)_{in}}{(S/N)_{out}} \tag{A.1}$$

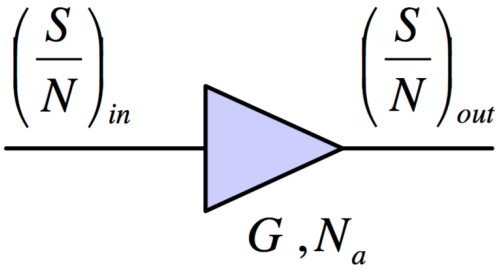

Figure A.1: A two-port representation for defining the noise figure.

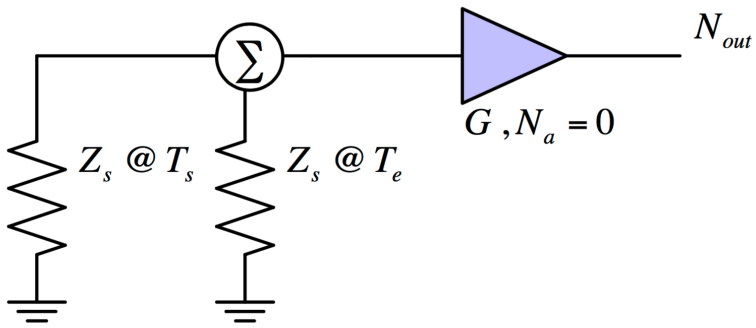

Figure A.2: An effective noise temperature representation for the evaluation of output noise power.

The noise figure (NF) is the decibel representation of a linear noise factor. The gain G is the ratio of output signal to the input signal. The noise factor can be written as

$$F = \frac{S_{in}N_{out}}{S_{out}N_{in}} = \frac{N_{out}}{GN_{in}} \tag{A.2}$$

As the noise is additive in nature, output noise is sum of amplified input noise and the added noise by the device.

$$N_{out} = GN_{in} + N_a \tag{A.3}$$

The added thermal noise N_a is proportional to the noise temperature T_e of a resistor Z_s. Fig. A.1 can be redefined as Fig. A.2 showing the input noise temperature and added noise as an effective noise temperature. The output noise power can be written as

$$N_{out} = GkT_sB + GkT_eB \tag{A.4}$$

where, B is the bandwidth in Hz and k is the Boltzman's constant in J/degree

K. The noise factor becomes

$$F = \frac{GkT_sB + GkT_eB}{GkT_sB} = 1 + \frac{T_e}{T_s} \tag{A.5}$$

and therefore,

$$T_e = T_s(F - 1) \tag{A.6}$$

Friis's analysis demonstrates the effect on overall noise factor when two or more stages are added. Multiple stages of the devices are cascaded together with gain $G_1$and G_2 along with the corresponding added noise temperature $T_{e1}$and T_{e2}. The noise power at output of first stage is

$$N_{out1} = G_1kT_sB + kT_{e1}B \tag{A.7}$$

The noise power at the output of second stage is

$$N_{out2} = G_2N_{out1} + kT_{e2}B = G_1G_2kT_sB + G_2kT_{e1}B + kT_{e2}B \tag{A.8}$$

$$N_{out2} = G_2N_{out1} + N_{a2} = G_1G_2kT_sB + G_2kT_s(F_1 - 1)B + kT_s(F_2 - 1)B \tag{A.9}$$

Using (A.2), the overall noise factor of two cascaded stages can be given as

$$F_{total} = F_1 + \frac{F_2 - 1}{G_1} \tag{A.10}$$

This equation proves that the first stage noise figure is the main factor affecting the overall noise figure. The second stage contribution can be reduced by making the gain of the first stage large. For n cascade stages of gain G_1, G_2, G_3.... G_n and noise factors F_1, F_2, F_3... F_n, the overall noise factor can

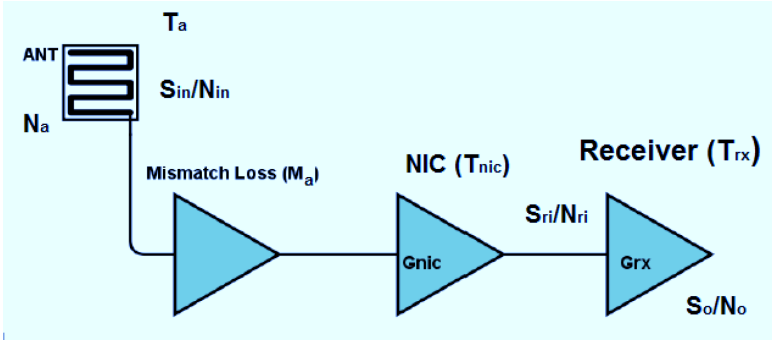

Figure A.3: The non-Foster antenna integrated with the receiver for overall noise figure calculation.

be derived as

$$F_{total} = F_1 + \frac{F_2 - 1}{G_1} + \frac{F_3 - 1}{G_1 G_2} .... + \frac{F_n - 1}{G_1 G_2 .. G_{n-1}} \tag{A.11}$$

This also proves that the minimum system noise figure can be attained when the first stage has minimum noise factor and a maximum gain. This results in least contribution of noise added during other stages.

A.2 Noise calculation for non-Foster antenna

This section discuss the application of Friis formula for a non-Foster antenna. Due to the atmospheric noise temperature T_a, the input noise power is given as $N_{in} = kT_aB$.Where, k is a Boltzmann's constant and B is the bandwidth.

As shown in Fig. A.3, M_a is the mismatch loss of the antenna and G_{nic} is gain of the NIC integrated with antenna. The noise temperature at the receiver output is given as

$$T_{out} = [(M_aT_a + T_{nic})G_{nic} + T_{rx}]G_{rx} \tag{A.12}$$

and therefore, output noise power is

$$N_{out} = kB[(M_a T_a + T_{nic})G_{nic} + T_{rx}]G_{rx} \tag{A.13}$$

Also, considering the input signal power S_{in}, the output signal power is given as

$$S_{out} = G_{nic} G_{rx} M_a S_{in} \tag{A.14}$$

The noise factor for the overall cascaded system is given as

$$F = \frac{N_{out} S_{in}}{N_{in} S_{out}} \tag{A.15}$$

$$F = \frac{[(M_a T_a + T_{nic})G_{nic} + T_{rx}]G_{rx}}{G_{nic} G_{rx} M_a S_{in} T_a}. \tag{A.16}$$

For an antenna with efficiency η_a, the noise factor from antenna input to the receiver system, F is redefined as

$$F = \eta_a + \frac{M_a(1-\eta_a)T_0 G_{nic} + T_{nic} G_{nic} + T_{rx}}{M_a T_a G_{nic}} \tag{A.17}$$

Above expression is clearly shows that the noise factor is high for a poor efficiency antenna.

Appendix B

RTD-based active metamaterial absorber

B.1 Introduction

MTM offers a diverse range of properties, such as negative permittivity ϵ, negative permeability μ and negative refractive index n [134], [135], [136]. They are not designed necessarily to operate at the level of material composition, but instead through the geometry of individual unit cells that encompass the effective material. The drawback is that they show high dispersion and are therefore narrow-banded and lossy in nature. Incorporation of active parameters into MTMs may be used to compensate for the dispersion. Discussion of Non-Foster impedance circuits for antenna applications so far, have been proposed as a potential candidate for wideband MTMs [90]. Frequency independent fast wave propagation, with phase velocity greater than the speed of light was recently demonstrated in an NFC-loaded wave guide structure [22]. The improvement of existing MTMs has been investigated using active inclusions as loads within each unit cell of a

structure [93], [137].

The BJT-based non-Foster impedance circuits have large form factor and complex design methods which restricts its integration in periodic structures like antenna array and MTMs. Also, BJT-based designs are tricky to realise series or shunt RLC loaded non-Foster impedance due to less control on the parasitics. Cross-coupled transistors have a positive feedback loop resulting in high sensitivity to stability. Hence, realization for the requirement of multiple stable BJT-based NFCs for a periodic MTM structure is a challenging task. Each BJT-based NFC has a decent power consumption which may lead to sufficient power requirement for active MTM structure.

An RTD-based NFC is more compact wherein, each design has one active element i.e. RTD and few passive elements. The design is very flexible with limited parasitics and also, it easy to design all possible non-Foster impedance configurations as discussed in chapter 3.4. In addition to this, series and parallel RLC loaded NFCs are easy to implement with the RTD approach as shown in Fig. B.1. Due to the absence of cross-coupled feedback loop, it is less sensitive to stability. Finally, very low power consumption is an added advantage for array applications. These properties of RTD-based designs makes them a potential candidate for array and MTM applications.

B.2 Active wideband absorber

A perfect electromagnetic absorber can be achieved by two-dimensional (2D) MTMs. As discussed earlier, conventional MTMs have their fundamental bandwidth limitations. Realisation of conventional MTM absorbers requires tailoring at the top of periodic electric resonators and spaced dielectric substrate as well as the bottom layer, to obtain impedance matching

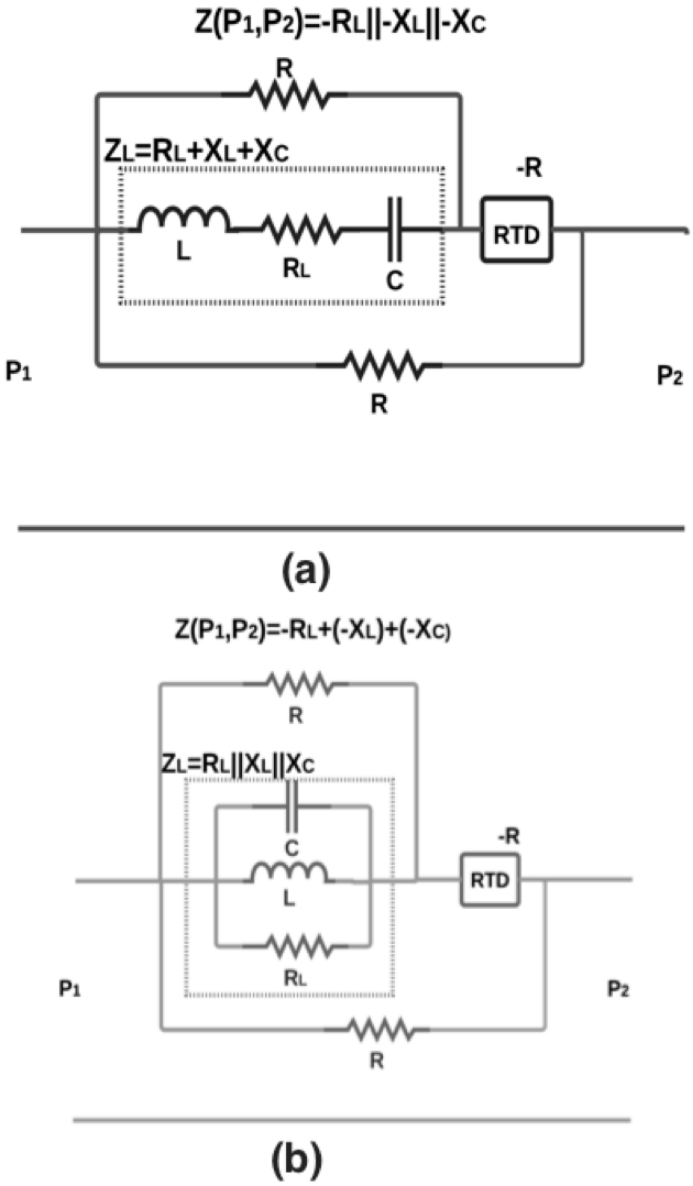

Figure B.1: RLC loaded NFC design approach using an RTD (a) A floating two-port circuit having equivalent impedance is the parallel combination of negative resistance, negative inductance and negative capacitance. (b) An equivalent impedance is the series combination of negative resistance, negative inductance and negative capacitance.

to the free space impedance i.e. 377 Ω. These microwave absorbers have the ability to absorb the incident electromagnetic waves with nearly unit absorption coefficient. The narrow bandwidth, polarization-sensitivity and narrow-angle of incidence are few limitations of passive MTMs despite of their high absorption coefficient.

The efforts to overcome these limitations have been exhibited by [138], [139], [140] and [141], in order to achieve bandwidth enhancement and improved angle of incidence. However, the structures become complicated and cover frequencies at THz and optical ranges. [142] proposed the insertion of metallic paths to substrate and improve the absorption bandwidth to certain extent. A novel active MTM absorber with non-Foster load is proposed in [21]. The analytical demonstration of an effective circuit model has been done for obliquely incident plane waves with both transverse-electric (TE) and transverse-magnetic (TM) polarisations. The circuit model includes material losses where stability theory has been presented for the non-Foster inclusion. As the standalone behaviour of NFCs is oscillatory in nature, passive MTM acts as a load similar to the non-Foster matched antenna. Similar to the antenna application, a two-port floating RTD has been integrated with unit cell of MTM to achieve a wideband and wide-angle MTM absorber. Electromagnetic absorption on a wide-band active MTM absorber and its passive counterpart, with wide-angle incidence for both TE and TM polarisations have been compared.

B.3 Effective circuit model

As shown in Fig. B.2, the structure of the novel active MTM absorber design has two-layer MTM structure with periodic metal square patch arrays on

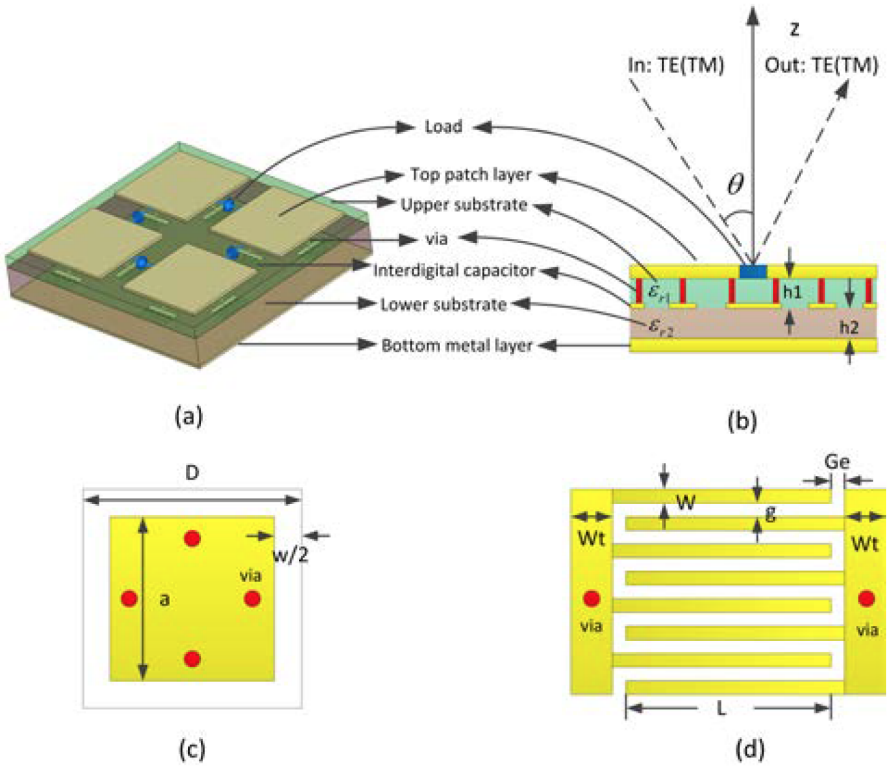

Figure B.2: MTM absorber structure (a) Top layer patch pattern including the non-Foster loads at the gap. (b) Side view showing the vias connecting inter-digital capacitor to top layer. (c) Each patch element at the top and the vias. (d) The inter-digital capacitor sandwiched between the substrate.

the top substrate layer and metal back on the bottom of the lower substrate layer. The non-Foster impedance circuits are connected between adjacent patches in the two-dimensional top layer. Further, each pair of the patch are connected by an inter-digital capacitor to increase the capacitance while keeping the structure electrically small. The inter-digital capacitors are sandwiched between the two substrate layers and are connected through vias with top layer patch arrays to minimize the coupling. Neglecting the mutual coupling effects by each element, the effective surface impedance of the structure can be defined similar to [143], as a parallel connection to: the grid impedance (Z_g), the substrate impedance (Z_s), the inter-digital impedance (Z_{int}), and the active non-Foster load (Z_L).

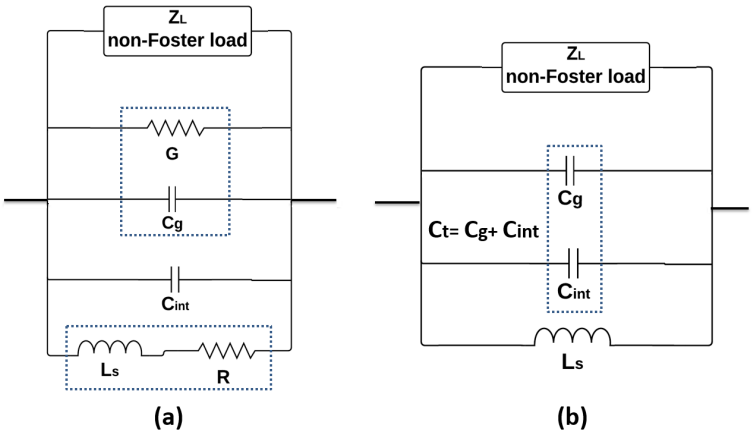

Figure B.3: (a) The effective circuit model of the non-Foster loaded active MTM absorber. (b) The simplified approximate model excluding the resistive and material losses.

$$Z_{MA} = Z_g||Z_s||Z_{int}||Z_L \tag{B.1}$$

These parasitics change the surface impedance at high frequencies and limit the operation only to lower frequencies. The grid impedance Z_g can be modelled in a parallel combination of electrical conductance G and capacitance C_g. Similarly, the substrate impedance can also be modelled as a series resistance R and inductance L_s. Also, the capacitance of the interdigital capacitor is C_{int}. As discussed previously, the effective circuit model of the MTM absorber is shown in Fig. B.3(a). The detailed expression for TE and TM polarisation are presented in [21]. The active non-Foster load value is critical for achieving a wideband and wide-angle incidence MTM absorber for both TE and TM polarisations. Also, the impedance matching of the structure with free space and air impedance can be analysed using reflection coefficient Γ.

$$\Gamma = \frac{Z_{MA} - Z_0}{Z_{MA} + Z_0} \tag{B.2}$$

where $Z0$ is the free space impedance. The reflectivity of the MTM absorber

structure is given as

$$R(\omega) = |\Gamma|^2 \tag{B.3}$$

Due to the metallic ground plane, the transmissivity of the structure $T(\omega) = 0$ and the absorption rate can be written as

$$A(\omega) = 1 - R(\omega) - T(\omega) = 1 - |\Gamma|^2 \tag{B.4}$$

To achieve infinite bandwidth for a wide range incidence angle, $Z_{MA} = Z_0$ which results in zero reflection and 100% absorption rate. It is possible to use suitable non-Foster load design by looking into Fig. B.3.

$$Z_L = R_L||L_L||C_L \tag{B.5}$$

where, $R_L = Z_0$, $L_L = -L_s$ and $C_L = -(C_g + C_{int})$

The grid conductance G and substrate resistance R still exist in the structure, but both are ignored in calculations due to their negligible values. An additional RTD may be required in final tuning to minimise the resistive effect.The approximate model excluding the resistive and material losses is shown in Fig. B.3(b)

Each non-Foster impedance circuit is oscillatory and unstable without their passive counterpart. The Routh-Hurwitz technique [144] can be applied to examine the solution of the system characteristic equation and determine the lumped elements within the stability bound. The stability conditions can be depicted as

$$C_L < -(C_g + C_{int}) = -C_t \tag{B.6}$$

$$-L_s < L_L < 0 \tag{B.7}$$

B.4 Design methodology

The aforementioned design principles are applied to a practical sample for verification. Here, Rogers RT5880 is used for the upper substrate, with a dielectric constant of 2.2 and loss tangent as 0.0009, whereas the lower substrate uses polyethylene as the host medium with a dielectric constant 2.25 and loss tangent as 0.001. The geometry parameters of the MA are illustrated in Table B.1. For the incidence angle up to 45° for both TE and TM polarisations, the stability bounds for the non-Foster elements can be obtained as $C_L < -3.97pF$ and $-9.89nH < L_L < 0$. The non-Foster impedance load for stable operation of active absorber is calculated in [21] as $R_L = 376\Omega$, $L_L = -9.6nH$ and $C_L = -5pF$.

This non-Foster load impedance by an RTD based approach is preferred due to its compact size in the periodic structure. As discussed in chapter 3.4, the impedance across two terminals of suitably biased RTD is dominated by real part as shown in Fig.B.4. Each shunt connected R is approximately equal to the RTD real impedance which is nearly 50 Ω and more than ten times the imaginary part up to 2 GHz. The circuit is shown in Fig. B.5 includes the non-Foster load equivalent for its passive counterpart. The calculation of internal load elements C_x and L_x of non-Foster impedance load circuit is required to obtain the desired negative elements. These are connected to a Π network along with two shunt resistances R and the series RTD. The series C_x and L_x are then connected in parallel with R, so, we get

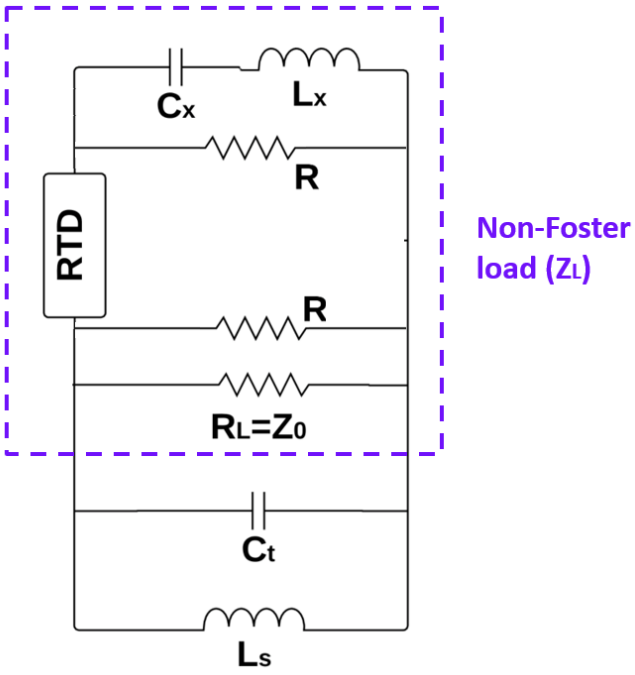

Figure B.4: The frequency response of real and imaginary impedance measured across both terminals of the RTD. The imaginary impedance is negligible for lower frequencies and significant beyond 2 GHz.

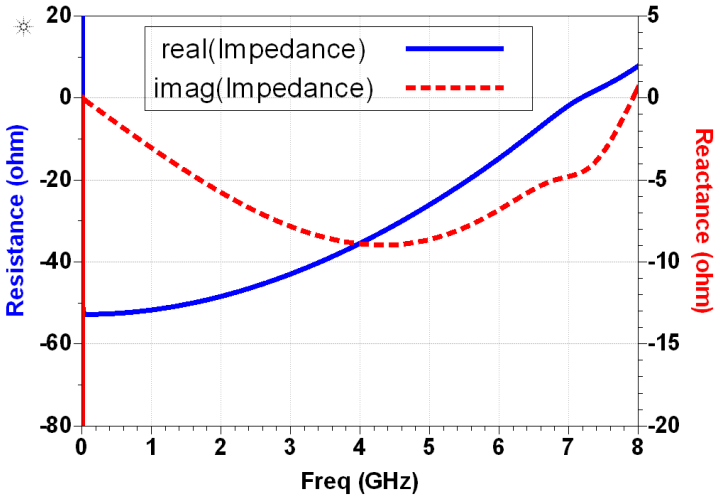

Figure B.5: The RTD based non-Foster impedance circuit to cancel the reactance of approximate model and additional resistance to match with free space impedance.

Table B.1: Geometry parameters of the MTM absorber.

Parameters	Symbol	Values(in mm)
Patch array period	D	20
Gap between patches	w	5
Finger width	W	0.2
Gap between fingers	G	0.2
Gap between fingers	G_e	0.2
Gap at end of fingers	G_e	0.2
Length of overlapped region	L	5
Number of fingers	N_p	10
Width of interconnect	W_t	1
Upper substrate thickness	h_1	0.127
Lower substrate thickness	h_2	10

Z_1 as

$$\begin{aligned} Z_1 &= \frac{\left(j\omega L_x + \frac{1}{j\omega C_x}\right) R}{j\omega L_x + \frac{1}{j\omega C_x} + R} \\ &= \frac{R - \omega^2 L_x C_x R}{j\omega C_x R + 1 - \omega^2 L_x C_x R} \end{aligned} \tag{B.8}$$

Z_1 is in series with an RTD impedance $-R$ and parallel to R, we get $Z_2 = (Z_1 + Z_{RTD})||R$. Further solving the circuit

$$\begin{aligned} Z_2 &= \frac{\left(\frac{R-\omega^2 L_x C_x R}{j\omega C_x R+1-\omega^2 L_x C_x R} - R\right) R}{\frac{R-\omega^2 L_x C_x R}{j\omega C_x R+1-\omega^2 L_x C_x R}} \\ &= \frac{-j\omega C_x R^2}{1 - \omega^2 L_x C_x} \end{aligned} \tag{B.9}$$

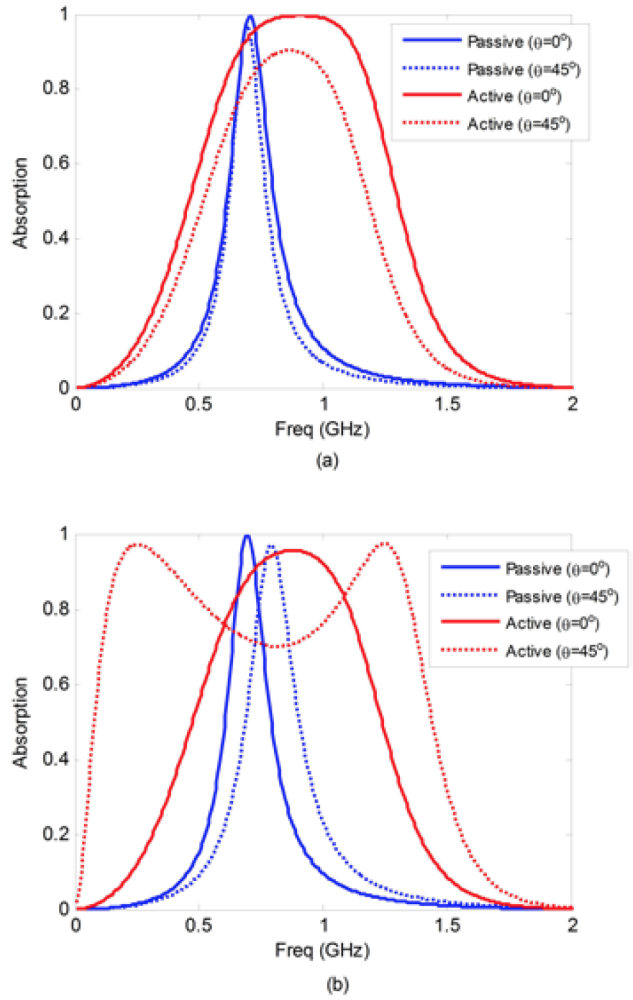

Figure B.6: The comparison of passive and active MTM absorber for normal and 45° angle of incidence. (a) TE polarisation (b) TM polarisation.

Rearranging the expression for Z_2, we can write as

$$\begin{aligned} Z_2 &= \frac{j\omega(-C_xR^2)\frac{1}{j\omega\left(-\frac{L_x}{R^2}\right)}}{j\omega(-C_xR^2)+\frac{1}{j\omega\left(-\frac{L_x}{R^2}\right)}} \\ &= \frac{j\omega(L_L)\frac{1}{j\omega(C_L)}}{j\omega(L_L)+\frac{1}{j\omega(C_L)}} \\ &= L_L||C_L \end{aligned} \tag{B.10}$$

Z_2 is clearly showing a parallel combination of negative inductance and capacitance with $L_L = -C_xR^2$ and $C_L = \frac{-L_x}{R^2}$. These reactive non-Foster

elements cancel the capacitance C_t and inductance L_s and the additional $R_L = Z_0 = 377\Omega$ match with the free space impedance. The resistive and material losses are neglected in the approximate model as shown in Fig. B.3 and the wideband impedance matching and wide angle of incidence have been obtained accordingly. The stable operational non-Foster load has internal load elements as $L_x = 12.5nH$, $C_x = 3.84pF$, $R = 50\Omega$, $R_L = 376\Omega$ and an RTD element biased at 2.75 V .

The full-wave simulation results with the design approach as earlier discussed are compared between passive and active MTM absorber for both TE and TM polarisation as shown in Fig. B.6(a) and B.6(b) respectively. High absorption rate for wideband frequencies and wide angle incidence has been achieved with active non-Foster inclusion. An absorption of more than 0.7 in the frequency band of 0.6 to 1.1 GHz and the incidence angle up to 45° is obtained.

B.5 Summary

A novel non-Foster loaded MTM absorber is presented with high absorption rate at wideband (0.6 GHz-1.1 GHz) and wide incidence angle (up to 45°) for both TE and TM polarisations. The stability characterisation is developed based on the effective circuit model of associated structure to give the value of non-Foster load elements for a stable operational. This non-Foster load is realised by compact RTD based non-Foster impedance circuits with certain approximations in effective circuit model of the structure. The design with and without non-Foster loading has been compared and bandwidth enhancement and wide angle incidence are observed with a non-Foster approach.

Bibliography

[1] J.G. Linvill. Transistor negative-impedance converters. *Proceedings of the IRE*, 6(41):725–729, 1953.

[2] J. M. C. Covington, K. L. Smith, J. W. Shehan, V. S. Kshatri, T. P. Weldon, and R. S. Adams. Measurement of a cmos negative inductor for wideband non-foster metamaterials. In *IEEE SOUTHEASTCON 2014*, pages 1–4, March 2014.

[3] C. R. White, J. W. May, and J. S. Colburn. A variable negative-inductance integrated circuit at uhf frequencies. *IEEE Microwave and Wireless Components Letters*, 22(1):35–37, Jan 2012.

[4] S. Saadat, H. Aghasi, E. Afshari, and H. Mosallaei. Low-power negative inductance integrated circuits for ghz applications. *IEEE Microwave and Wireless Components Letters*, 25(2):118–120, 2015.

[5] Deepak Singh Nagarkoti, Y. Hao, D.P. Steenson, L. Li, E.H. Linfield, and K.Z. Rajab. Design of broadband non-Foster circuits based on resonant tunneling diodes. *IEEE Antennas and Wireless Propagation Letters*, 15:1398–1401, 2016.

[6] H. A. Wheeler. Fundamental limitations of small antennas. *Proceedings of the IRE*, 35(12):1479–1484, 1947.

[7] L.J. Chu. Physical limitations of omni-directional antennas. *Journal of applied physics*, 19(12):1163–1175, 1948.

[8] R.F. Harrington. Effect of antenna size on gain, bandwidth, and efficiency. *J. Res. Nat. Bur. Stand*, 64(1):1–12, 1960.

[9] Collin and S. Rothschild. Evaluation of antenna Q. *IEEE Transactions on Antennas and Propagation*, 12(1):23–27, 1964.

[10] R. Fante. Quality factor of general ideal antennas. *IEEE Transactions on Antennas and Propagation*, 17(2):151–155, 1969.

[11] J.S. McLean. A re-examination of the fundamental limits on the radiation Q of electrically small antennas. *IEEE Transactions on antennas and propagation*, 44(5):672, 1996.

[12] G.A. Thiele, P.L. Detweiler, and R.P. Penno. On the lower bound of the radiation q for electrically small antennas. *IEEE Transactions on Antennas and Propagation*, 51(6):1263–1269, 2003.

[13] W. Geyi. A method for the evaluation of small antenna Q. *IEEE Transactions on Antennas and Propagation*, 51(8):2124–2129, 2003.

[14] A.D. Yaghjian and S.R. Best. Impedance, bandwidth, and Q of antennas. *IEEE Transactions on Antennas and Propagation*, 53(4):1298–1324, 2005.

[15] D. Kwon. On the radiation Q and the gain of crossed electric and magnetic dipole moments. *IEEE Transactions on Antennas and Propagation*, 53(5):1681–1687, 2005.

[16] H.L. Thal. New radiation Q limits for spherical wire antennas.

IEEE Transactions on Antennas and Propagation, 54(10):2757–2763, 2006.

[17] M. Gustafsson and G. Sohl, C.and Kristensson. Physical limitations on antennas of arbitrary shape. In *Proceedings of the Royal Society of London A: Mathematical, Physical and Engineering Sciences*, volume 463, pages 2589–2607. The Royal Society, 2007.

[18] H. W Bode et al. Network analysis and feedback amplifier design. 1945.

[19] R.M. Fano. Theoretical limitations on the broadband matching of arbitrary impedances. *Journal of the Franklin Institute*, 249(1):57–83, 1950.

[20] R.M. Foster. A reactance theorem. *Bell System Technical Journal*, 3(2):259–267, 1924.

[21] Y. Fan, H.C. Zhang, J.Y. Yin, L. Xu, Deepak Singh Nagarkoti, Y. Hao, and T. Cui. An active wideband and wide-angle electromagnetic absorber at microwave frequencies.

[22] J. Long, M.M. Jacob, and D.F. Sievenpiper. Broadband fast-wave propagation in a non-Foster circuit loaded waveguide. *IEEE Transactions on Microwave Theory and Techniques*, 62(4):789–798, 2014.

[23] J.L. Merrill. Theory of the negative impedance converter. *Bell System Technical Journal*, 30(1):88–109, 1951.

[24] A. Larky. Negative-impedance converters. *IRE Transactions on Circuit Theory*, 4(3):124–131, 1957.

[25] T. Yanagisawa. RC active networks using current inversion type negative impedance converters. *IRE Transactions on Circuit Theory*, 4(3):140–144, 1957.

[26] P.V. Indiresan. A negative resistance for dc computers. *Radio Engineers, Journal of the British Institution of*, 19(7):401–410, 1959.

[27] M. Nagata. A simple negative impedance circuit with no internal bias supplies and good linearity. Technical report, DTIC Document, 1965.

[28] A. Antoniou. Gyrators using operational amplifiers. *Electronics Letters*, 3(8):350–352, 1967.

[29] J. Tian, Deepak Singh Nagarkoti, K.Z. Rajab, and Y. Hao. Graphene-based tunable non-Foster circuit for vhf applications. *AIP Advances*, 6(6):065202, 2016.

[30] A. Antoniou. Realisation of gyrators using operational amplifiers, and their use in rc-active-network synthesis. In *Proceedings of the Institution of Electrical Engineers*, volume 116, pages 1838–1850. IET, 1969.

[31] I.W. Sandberg. Synthesis of driving-point impedances with active rc networks. *Bell Labs Technical Journal*, 39(4):947–962, 1960.

[32] O. Tade, P. Gardner, and P. Hall. Antenna bandwidth broadening with a negative impedance converter. *International Journal of Microwave and Wireless Technologies*, 5(03):249–260, 2013.

[33] S.E. Sussman-Fort and R.M. Rudish. Non-Foster impedance matching of electrically-small antennas. *IEEE Transactions on Antennas and Propagation*, 57(8):2230–2241, 2009.

[34] F. Albarracin-Vargas, V. Gonzalez-Posadas, F. J. Herraiz-Martinez, and D. Segovia-Vargas. Design method for actively matched antennas with non-foster elements. *IEEE Transactions on Antennas and Propagation*, 64(9):4118–4123, Sept 2016.

[35] H. Mirzaei and G. V. Eleftheriades. A resonant printed monopole antenna with an embedded non-foster matching network. *IEEE Transactions on Antennas and Propagation*, 61(11):5363–5371, Nov 2013.

[36] J. Tian, A. Katsounaros, D. Smith, and Y. Hao. Graphene field-effect transistor model with improved carrier mobility analysis. *IEEE Transactions on Electron Devices*, 62(10):3433–3440, 2015.

[37] C.R. White, J.S. Colburn, and R.G. Nagele. A non-Foster vhf monopole antenna. *IEEE Antennas and Wireless Propagation Letters*, 11:584–587, 2012.

[38] D.P. Steenson, R.E. Miles, R.D. Pollard, J.M. Chamberlain, and M. Henini. Demonstration of power combining at w-band from gaas/alas resonant tunneling diodes. In *Proc. 5th Int. Symp. Space Terahertz Technol*, pages 10–12, 1994.

[39] L. Chang, L. Esaki, and R. Tsu. Resonant tunneling in semiconductor double barriers. *Applied Physics Letters*, 24(12):593–595, 1974.

[40] D.J. Gregoire, C.R. White, and J.S. Colburn. Wideband artificial magnetic conductors loaded with non-foster negative inductors. *IEEE Antennas and Wireless Propagation Letters*, 10:1586–1589, 2011.

[41] L.P. Huelsman. The compensation of negative-immittance converters. *Proceedings of the IEEE*, 54(7):1015–1016, 1966.

[42] A. Schwarz. On the stability properties of a negative-immittance converter. *IEEE Transactions on Circuit Theory*, 14(1):77–77, 1967.

[43] A. Davies. Stability properties of a negative immittance converter. *IEEE Transactions on Circuit Theory*, 15(1):80–81, 1968.

[44] J. Brownlie. On the stability properties of a negative impedance converter. *IEEE Transactions on Circuit Theory*, 13(1):98–99, 1966.

[45] R.F. Hoskins. Stability of negative-impedance convertors. *Electronics Letters*, 9(2):341, 1966.

[46] S.D. Stearns. Non-foster circuits and stability theory. In *Antennas and Propagation (APSURSI), 2011 IEEE International Symposium on*, pages 1942–1945. IEEE, 2011.

[47] S.D. Stearns. Circuit stability theory for non-foster circuits. In *Microwave Symposium Digest (IMS), 2013 IEEE MTT-S International*, pages 1–3. IEEE, 2013.

[48] Marion Lee Edwards and Jeffrey H Sinsky. A new criterion for linear 2-port stability using a single geometrically derived parameter. *IEEE Transactions on Microwave Theory and Techniques*, 40(12):2303–2311, 1992.

[49] K.Z. Rajab, Y.F. Fan, and Y. Hao. Characterization of active metamaterials based on negative impedance converters. *Journal of Optics*, 14(11):114004, 2012.

[50] E.J. Routh. *The Elementary Part of a Treatise on the Dynamics of a System of Rigid Bodies... Revised and Enlarged*. Macmillan & Company, 1897.

[51] A. Hurwitz. Ueber die bedingungen, unter welchen eine gleichung nur wurzeln mit negativen reellen theilen besitzt. *Mathematische Annalen*, 46:273–284, 1895.

[52] K.Z. Rajab, Y. Hao, D. Bao, C.G. Parini, J. Vazquez, and M. Philippakis. Stability of active magnetoinductive metamaterials. *Journal of Applied Physics*, 108(5):054904, 2010.

[53] E. Kreyszig. *Advanced engineering mathematics*. John Wiley & Sons, 2010.

[54] J. Verdera. On the T (1)-theorem for the cauchy integral. *Arkiv för Matematik*, 38(1):183–199, 2000.

[55] R.C. Hansen and R.E. Collin. A new chu formula for q. *IEEE Antennas and Propagation Magazine*, 51(5):38–41, 2009.

[56] P. Mayes and F. Warren, W .and Wiesenmeyer. The monopole-slot: A broadband, unidirectional antenna. In *Antennas and Propagation Society International Symposium, 1971*, volume 9, pages 109–112. IEEE, 1971.

[57] A.J. Bahr, U.H. Gysel, and A. Phillips. Active network techniques for improving antenna performance. Technical report, DTIC Document, 1977.

[58] George Skahill. Dipole television antenna, September 15 1998. US Patent 5,808,584.

[59] Z.H. Hu, C. Song, J. Kelly, P.S. Hall, and P. Gardner. Wide tunable dual-band reconfigurable antenna. *Electronics letters*, 45(22):1, 2009.

[60] M..ël Pelissier, F. Demeestere, F. Hameau, D. Morche, and C. Delaveaud. Lna-antenna codesign for uwb systems. In *2006 IEEE International Symposium on Circuits and Systems*, pages 4–pp. IEEE, 2006.

[61] D. Ueo, H. Osabe, K. Inafune, M. Ikebe, E. Sano, M. Koutani, M. Ikeda, and K. Mashiko. 7-ghz inverted-f antenna monolithically integrated with cmos lna. In *2006 International Symposium on Intelligent Signal Processing and Communications*, pages 259–262. IEEE, 2006.

[62] J.T. Aberle. Two-port representation of an antenna with application to non-Foster matching networks. *IEEE Transactions on Antennas and Propagation*, 56(5):1218–1222, 2008.

[63] B. Van der Pol. A new transformation in alternating-current theory with an application to the theory of audition. *Proceedings of the Institute of Radio Engineers*, 18(2):220–230, 1930.

[64] G. Skahill, R.M. Rudish, and J.A. Pierro. Apparatus and method for broadband matching of electrically small antennas, September 19 2000. US Patent 6,121,940.

[65] A.D. Harris and G.A. Myers. An investigation of broadband miniature antennas. Technical report, DTIC Document, 1968.

[66] A. Poggio and P. Mayes. A unique broadband dipole antenna design utilizing conjugate reactance loading. In *Antennas and Propagation Society International Symposium, 1969*, volume 7, pages 250–258. IEEE, 1969.

[67] A. Poggio and P. Mayes. Bandwidth extension for dipole antennas by conjugate reactance loading. *IEEE Transactions on Antennas and Propagation*, 19(4):544–547, 1971.

[68] A.K. Perry. Broadband antenna systems realized from active circuit conjugate impedance matching. Technical report, DTIC Document, 1973.

[69] R.M. Rudish and S.E. Sussman-Fort. Non-Foster impedance matching improves s/n of wideband electrically small vhf antennas and arrays. In *IASTED Conf. on Antennas, Radar and Wave Propag., Banff, AB, Canada*, 2005.

[70] S.E. Sussman-Fort and R.M. Rudish. Progress in use of non-Foster impedances to match electrically-small antennas and arrays. In *Proceedings of the Antenna Applications Symposium*, pages 89–108, 2005.

[71] S.E. Sussman-Fort. Matching network design using non-Foster impedances. *International Journal of RF and Microwave Computer-Aided Engineering*, 16(2):135–142, 2006.

[72] S.E. Sussman-Fort and R.M. Rudish. Non-Foster impedance matching for transmit applications. In *IEEE International Workshop on Antenna Technology Small Antennas and Novel Metamaterials, 2006.*, pages 53–56. IEEE, 2006.

[73] S.E. Sussman-Fort and R.M. Rudish. Non-Foster impedance matching of a lossy, electrically-small antenna over an extended frequency range. In *the Antenna Applicat. Symp*, pages 220–240, 2007.

[74] S.E. Sussman-Fort and R.M. Rudish. Non-Foster matching of

electrically-small antennas to transmitters. In *Proceedings of the 2008 Antenna Applications Symposium*, pages 326–342, 2008.

[75] C. Di Nallo, G. Bit-Babik, and A. Faraone. Wideband antenna using non-Foster loading elements. In *2007 IEEE Antennas and Propagation Society International Symposium*, pages 4501–4504. IEEE, 2007.

[76] NXP Semiconductors. *NPN 25 GHz wideband transistor*, 2010. Rev. 1.

[77] Advanced design system-ads software, 2013.

[78] F. Schwierz. Graphene transistors: status, prospects, and problems. *Proceedings of the IEEE*, 101(7):1567–1584, 2013.

[79] K.I. Bolotin, K.J. Sikes, Z. Jiang, M. Klima, G. Fudenberg, J. Hone, P. Kim, and H.L. Stormer. Ultrahigh electron mobility in suspended graphene. *Solid State Communications*, 146(9):351–355, 2008.

[80] K. Bolotin, K.J. Sikes, J. Hone, H.L. Stormer, and P. Kim. Temperature-dependent transport in suspended graphene. *Physical review letters*, 101(9):096802, 2008.

[81] H. Wang, T. Taychatanapat, A. Hsu, K. Watanabe, T. Taniguchi, P. Jarillo-Herrero, and T. Palacios. Bn/graphene/bn transistors for rf applications. *arXiv preprint arXiv:1108.2021*, 2011.

[82] X. Yang, G. Liu, A. A Balandin, and K. Mohanram. Triple-mode single-transistor graphene amplifier and its applications. *ACS nano*, 4(10):5532–5538, 2010.

[83] High-frequency graphene voltage amplifier. *Nano letters*, 11(9):3690–3693, 2011.

[84] H. Wang, A. Hsu, J. Wu, J. Kong, and T. Palacios. Graphene-based ambipolar rf mixers. 2010.

[85] Deepak Singh Nagarkoti, K.Z. Rajab, and Y. Hao. Design and stability of negative impedance circuits for non-Foster matching of a monopole antenna. In *The 8th European Conference on Antennas and Propagation (EuCAP 2014)*, 2014.

[86] T. Wei, S. Stapleton, and E. Berolo. Equivalent circuit and capacitance of double barrier resonant tunneling diode. *Journal of applied physics*, 73(2):829–834, 1993.

[87] M.E. Hines. High-frequency negative-resistance circuit principles for esaki diode applications. *Bell System Technical Journal*, 39(3):477–513, 1960.

[88] I.T. Frisch. A stability criterion for tunnel diodes. *Proceedings of the IEEE*, 52(8):922–923, 1964.

[89] M. Hirvonen, A. Hujanen, J. Holmberg, and J. Sten. Bandwidth limitations of dipoles matched with non-foster impedances. In *The Second European Conference on Antennas and Propagation, EuCAP 2007*, 2007.

[90] S.A. Tretyakov. Meta-materials with wideband negative permittivity and permeability. *Microwave and Optical Technology Letters*, 31(3):163–165, 2001.

[91] M. Barbuto, A. Monti, F. Bilotti, and A. Toscano. Design of a non-Foster actively loaded srr and application in metamaterial-inspired components. *IEEE Transactions on Antennas and Propagation*, 61(3):1219–1227, 2013.

[92] S. Hrabar, I. Krois, I.. Bonic, and A. Kiricenko. Basic concepts of active dispersionless metamaterial based on non-Foster elements. In *ICECom, 2010 Conference Proceedings*, pages 1–4. IEEE, 2010.

[93] S. Hrabar, I. Krois, I. Bonic, and A. Kiricenko. Negative capacitor paves the way to ultra-broadband metamaterials. *Applied physics letters*, 99(25):254103, 2011.

[94] E. Ugarte-Munoz, S. Hrabar, D. Segovia-Vargas, and A. Kiricenko. Stability of non-Foster reactive elements for use in active metamaterials and antennas. *IEEE transactions on antennas and propagation*, 60(7):3490–3494, 2012.

[95] S. Saadat, M. Adnan, H. Mosallaei, and E. Afshari. Composite metamaterial and metasurface integrated with non-Foster active circuit elements: A bandwidth-enhancement investigation. *IEEE Transactions on Antennas and Propagation*, 61(3):1210–1218, 2013.

[96] S.R. Rengarajan and C.R. White. Stability analysis of superluminal waveguides periodically loaded with non-Foster circuits. *IEEE Antennas and Wireless Propagation Letters*, 12:1303–1306, 2013.

[97] P. Chen, C. Argyropoulos, and A. Alù. Broadening the cloaking bandwidth with non-Foster metasurfaces. *Physical review letters*, 111(23):233001, 2013.

[98] Y. Fan, K.Z. Rajab, and Y. Hao. Noise analysis of broadband active metamaterials with non-Foster loads. *Journal of Applied Physics*, 113(23):233905, 2013.

[99] E. Bloch and E. Socher. Beyond the smith chart: A universal graphical

tool for impedance matching using transformers. *IEEE Microwave Magazine*, 15(7):100–109, 2014.

[100] K. Ito, B. Murata, and K. Yoshimura. Coaxial cable connector plug, February 10 1981. US Patent 4,249,790.

[101] O. Yoshihiro. Murata integrates switch to coaxial connector, improves inspection process. *Technology Focus*, pages 47–49, Nov., 2007.

[102] D.M. Kerns. Correction of near-field antenna measurements made with an arbitrary but known measuring antenna. *Electronics Letters*, 11(6):346–347, 1970.

[103] Agilent Technologies. *Fundamentals of RF and Microwave Noise Figure Measurements*, 2010. Rev. 1.

[104] M. Stoisiek and D. Wolf. Recent investigations on the stationarity of $1/f$ noise. *Journal of Applied Physics*, 47(1):362–364, 1976.

[105] M. Stoisiek and D. Wolf. Origin of 1/f noise in bipolar transistors. *IEEE Transactions on Electron Devices*, 27(9):1753–1757, 1980.

[106] E.R. Chenette and A. Van der Ziel. Accurate noise measurements on transistors. *IRE Transactions on Electron Devices*, 9(2):123–128, 1962.

[107] A. Van Der Ziel. Theory of shot noise in junction diodes and junction transistors. *Proceedings of the IRE,* 43(11):1639–1646, 1955.

[108] A. Van der Ziel. Noise in junction transistors. *Proceedings of the IRE*, 46(6):1019–1038, 1958.

[109] E. Nielsen. Behavior of noise figure in junction transistors. *Proceedings of the IRE,* 45(7):957–963, 1957.

[110] H.A. Haus, W.R. Atkinson, G.M. Branch, W.B. Davenport, W.H. Fonger, W.A. Harris, S.W. Harrison, W.W. McLeod, E.K. Stodola, and T.E. Talpey. Representation of noise in linear two ports. *Proceedings of the IRE*, 48(1):69–74, 1960.

[111] H. Fukui. Available power gain, noise figure, and noise measure of two-ports and their graphical representations. *IEEE transactions on circuit theory*, 13(2):137–142, 1966.

[112] E. Ulrich. Use negative feedback to slash wideband $vswr$. *Microwaves*, 17(10):66, 1978.

[113] K.B. Niclas. The exact noise figure of amplifiers with parallel feedback and lossy matching circuits. *IEEE Transactions on Microwave Theory and Techniques*, 5(30):832–835, 1982.

[114] S. Iversen. The effect of feedback on noise figure. *Proceedings of the IEEE*, 63(3):540–542, 1975.

[115] V. Lam, C.R. Poole, and P. Yip. Exact noise figure of a noisy two-port with feedback. *IEE Proceedings G-Circuits, Devices and Systems*, 139(4):473–476, 1992.

[116] W. Adamski. Methods for direct-reading noise measurements of low-gain two-ports. *IEEE transactions on instrumentation and measurement*, 43(3):411–414, 1994.

[117] W. Adamski. Noise figure measurement uncertainty caused by low gain of the two-port under test. In *Microwaves, Radar and Wireless Communications. 2000. MIKON-2000. 13th International Conference on*, volume 1, pages 325–328. IEEE, 2000.

[118] L. Colby and B. Heinz. Accuracy of noise figure measurement systems. In *RF & Microwave Symposium and Exhibition, Hewlett Packard*, 1988.

[119] D. Boyd. Calculate the uncertainty of nf measurements. *Microwaves & RF*, 38(10), 1999.

[120] Agilent Technologies. *Operating and Service Manual Agilent 346A/B/C Noise Source*, 2013. Rev. 1.

[121] Rhode & Schwartz. *Application Firmware for Noise Figure and Gain Measurements R&S FS-K30 for R&S FSP/FSU/FSQ*, 2003. Rev. 1.

[122] H.T. Friis. A note on a simple transmission formula. *Proceedings of the IRE*, 34(5):254–256, 1946.

[123] S.R. Best. Realized noise figure of the general receiving antenna. *IEEE Antennas and Wireless Propagation Letters*, 12:702–705, 2013.

[124] A. Willig. Recent and emerging topics in wireless industrial communications: A selection. *IEEE Transactions on industrial informatics*, 4(2):102–124, 2008.

[125] M. Jonsson and K. Kunert. Towards reliable wireless industrial communication with real-time guarantees. *IEEE Transactions on Industrial Informatics*, 5(4):429–442, 2009.

[126] W. C. Brown. The history of power transmission by radio waves. *IEEE Transactions on Microwave Theory and Techniques*, 32(9):1230–1242, 1984.

[127] J. Akkermans, M.C. Van B., G. Doodeman, and H.J. Visser. Analytical

models for low-power rectenna design. *IEEE Antennas and Wireless Propagation Letters*, 4(1):187–190, 2005.

[128] C. Lo, Y. Yang, C. Tsai, C. Lee, and C. Yang. Novel wireless impulsive power transmission to enhance the conversion efficiency for low input power. In *Microwave Workshop Series on Innovative Wireless Power Transmission: Technologies, Systems, and Applications (IMWS), 2011 IEEE MTT-S International*, pages 55–58. IEEE, 2011.

[129] P. Grover and A. Sahai. Shannon meets tesla: Wireless information and power transfer. In *Information Theory Proceedings (ISIT), 2010 IEEE International Symposium on*, pages 2363–2367. IEEE, 2010.

[130] E. Caspers, S. Yeung, T.K. Sarkar, A. Garcia-Lamperez, M. Palma, M. Lagunas, and A. Perez-Neira. Analysis of information and power transfer in wireless communications. *IEEE Antennas and Propagation Magazine*, 55(3):82–95, 2013.

[131] W. Rhee and J. Cioffi. Increase in capacity of multiuser ofdm system using dynamic subchannel allocation. In *Vehicular Technology Conference Proceedings, 2000. VTC 2000-Spring Tokyo. 2000 IEEE 51st*, volume 2, pages 1085–1089. IEEE, 2000.

[132] Claude Elwood Shannon. Communication in the presence of noise. *Proceedings of the IRE*, 37(1):10–21, 1949.

[133] T. K. Sarkar, S. H. Yeung, M. Salazar-Palma, M. A. Lagunas, and A. I. Perez-Neira. The effect of broadband matching in simultaneous information and power transfer. *IEEE Antennas and Propagation Magazine*, 57(1):192–203, Feb 2015.

[134] D.R. Smith, J.B. Pendry, and M. Wiltshire. Metamaterials and negative refractive index. *Science*, 305(5685):788–792, 2004.

[135] P. Smith, D.and Kolinko and D. Schurig. Negative refraction in indefinite media. *JOSA B*, 21(5):1032–1043, 2004.

[136] J.B. Pendry, D. Schurig, and D. Smith. Controlling electromagnetic fields. *science*, 312(5781):1780–1782, 2006.

[137] J.P. Turpin, J.A. Bossard, K.L. Morgan, D.H. Werner, and P.L. Werner. Reconfigurable and tunable metamaterials: a review of the theory and applications. *International Journal of Antennas and Propagation*, 2014, 2014.

[138] J. Grant, Y. Ma, S. Saha, A. Khalid, and D. Cumming. Polarization insensitive, broadband terahertz metamaterial absorber. *Optics letters*, 36(17):3476–3478, 2011.

[139] K. Alici, A. Turhan, C.M. Soukoulis, and E. Ozbay. Optically thin composite resonant absorber at the near-infrared band: a polarization independent and spectrally broadband configuration. *Optics express*, 19(15):14260–14267, 2011.

[140] L. Huang, D. Chowdhury, S. Ramani, M. Reiten, S. Luo, A.J. Taylor, and H. Chen. Experimental demonstration of terahertz metamaterial absorbers with a broad and flat high absorption band. *Optics letters*, 37(2):154–156, 2012.

[141] H. Wakatsuchi, S. Greedy, C. Christopoulos, and J. Paul. Customised broadband metamaterial absorbers for arbitrary polarisation. *Optics express*, 18(21):22187–22198, 2010.

[142] O. Luukkonen, F. Costa, C.R. Simovski, A. Monorchio, and S.A. Tretyakov. A thin electromagnetic absorber for wide incidence angles and both polarizations. *IEEE Transactions on Antennas and Propagation*, 57(10):3119–3125, 2009.

[143] O. Luukkonen, C.R. Simovski, A.V. Raisanen, and S.A. Tretyakov. An efficient and simple analytical model for analysis of propagation properties in impedance waveguides. *IEEE Transactions on Microwave Theory and Techniques*, 56(7):1624–1632, 2008.

[144] A. Hurwitz. On the conditions under which an equation has only roots with negative real parts. *Selected papers on mathematical trends in control theory*, 65:273–284, 1964.